THE OHIO STATE UNIVERSITY

College of Engineering
Department of Chemical and Biomolecular Engineering
and Department of Materials Science and Engineering

Project Final Technical Report

Submitted to the U.S. Department of Energy
National Energy Technology Laboratory

NATIONAL ENERGY TECHNOLOGY LABORATORY

FE0031731: Novel Transformational Membranes and Process for CO_2 Capture from Flue Gas

PI: W.S. Winston Ho, Professor
E-mail: ho.192@osu.edu
Phone: 614-292-9970; Fax: 614-292-3769
The Ohio State University
151 West Woodruff Avenue
Columbus, OH 43210-1350

Co-PIs: Dr. Yang Han and Dr. Li-Chiang Lin

Project Period: July 1, 2019 – March 31, 2023
Reporting Period: July 1, 2019 – March 31, 2023
Submission Date: June 20, 2023
Revision Date: July 5, 2023

UEI: DLWBSLWAJWR1

DISCLAIMER

Table of Contents

1 Executive Summary

The objectives of this project are to develop a cost-effective design and fabrication process for a novel transformational membrane and its membrane modules that capture CO_2 from flue gas. Optimization of the novel transformational membrane, scale-up of the membrane to a prototype size of about 20″ wide in continuous roll-to-roll fabrication, and construction and testing of a skid for the integrated membrane process will be performed. For the design of this membrane, we use a cost-effective polymer support and coat a thin top layer of the membrane. The simplicity of this membrane design offers a low cost for the membrane element in commercial spiral-wound (SW) configuration (<\$2.00/ft^2 or \$21.5/m^2). The prototype membrane will be used to fabricate 6 pilot-size membrane modules (each about 20″ length, 3 modules each at the commercial-size diameter of 8 inches with 35 m^2 membrane area for Stage 1 and 3 modules each at 5-inch diameter with 12 m^2 membrane area for Stage 2) for testing with simulated flue gas at OSU and with actual flue gas at the National Carbon Capture Center, Wilsonville, AL using the skid to capture the CO_2 (at 60 – 90%) with at least 95% CO_2 purity. The prototype membrane modules will be in commercial SW configuration with a minimal pressure drop (<0.103 bar/meter (1.5 psi/meter)). These objectives have been achieved successfully.

We have prepared the best polyethersulfone (PES) support with an exceptional CO_2 permeance of 316,000 GPU for the synthesis of transformational facilitated transport membranes (FTMs) in thin-film composite configuration. This PES was achieved via a series of PES casting solution compositional improvement, including 1) improved hydrophilic modifying agent for incorporation in the PES support to improve the adhesion of the selective layer on top of the support, 2) better pore former, and 3) optimized thermodynamic stability of casting solution during vapor-induced phase separation to achieve higher porosity and bicontinuous morphology. Using this support, we have synthesized transformational FTMs, showing an exceptionally high CO_2 permeance of 4200 GPU and a high CO_2/N_2 selectivity of >160. The FTM was synthesized via a series of compositional improvement, including 1) improved interfacial compatibility between the selective layer and the polymer support to enable ultrathin, defect-free coating, 2) better amine carrier with optimal steric hindrance through density functional theory calculations, 3) optimized nanofiller geometry, and 4) higher MW polyamine synthesized for incorporating a greater amount of mobile carrier in the membrane, preparing a thinner membrane due to a lower concentration coating solution with suitable viscosity, and reducing selective-layer coating penetration into the improved porous support to achieve higher CO_2 permeance.

The membrane was scaled up successfully to a width of 21 inches through continuous roll-to-roll fabrication. The scale-up membrane showed the same performance as the lab-scale membrane, i.e., a CO_2 permeance of 4200 GPU and a CO_2/N_2 selectivity of >160. The scale-up membrane was used to fabricate 6 pilot-size SW membrane modules (each about 20″ length, 3 modules each at the commercial-size diameter of 8 inches with 35 m^2 membrane area for Stage 1 and 3 modules each at 5-inch diameter with 12 m^2 membrane area for Stage 2). The separation performances of the SW membrane modules were on par with the flat-sheet membranes fabricated in pilot scale (via continuous roll-to-roll fabrication) and synthesized in lab scale, i.e., a CO_2 permeance of 4200 GPU and a CO_2/N_2 selectivity of >160.

We designed and constructed a 2-stage membrane process skid consisting of 1 commercial-size 8-inch diameter membrane module of 35 m^2 membrane area for Stage 1 and one 5-inch diameter membrane module of 12 m^2 for Stage 2. The skid tests at the National Carbon Capture Center (NCCC) in Wilsonville, Alabama showed 90 – 99% CO_2 capture degrees for 8.6% and 4.3% CO_2 concentrations, for actual natural gas flue gas (0.88 tonne/day of CO_2 at 90% capture or ~285 kg/h flue gas flow rate) and air-diluted natural gas flue gas (0.44 tonne/day of CO_2 at 90% capture, ~280 kg/h flue gas flow rate or ~44 kW_e natural gas combined cycle (NGCC) power equivalency), respectively, all with ≥95% CO_2 purity. The skid test results were consistent with the membrane performance of 4200 GPU CO_2 permeance along with a CO_2/N_2 selectivity of at least 160. The skid test duration using the actual natural gas flue gas was 500 h, and that using the air-diluted natural gas flue gas was about 300 h. Based on the skid test results, the subrecipient Gas Technology Institute conducted the final techno-economic analysis (TEA), showing a capture cost of $38.92/tonne of CO_2 (in 2018 dollars). The achieved technology readiness level (TRL) is at least TRL 5 as the basic technology components have been integrated and validated in a relevant environment. In fact, it is close to TRL 6 as commercial-size prototype membrane modules were fabricated and used in a relevant environment using actual flue gas at the NCCC.

2 Project Overview

2.1 Major Goals of the Project

The objectives of this project are to develop a cost-effective design and fabrication process for a novel transformational membrane and its membrane modules that capture CO_2 from flue gas. Optimization of the novel transformational membrane, scale-up of the membrane to a prototype size of about 20 inches wide in continuous roll-to-roll fabrication, and construction and testing of a bench skid for the integrated membrane process will be performed. For the design of this membrane, we use a cost-effective polyethersulfone (PES) support and coat a thin top layer of the membrane. The simplicity of this membrane design offers a low cost for the membrane element in commercial spiral-wound configuration (<$2.00/$ft^2$ or $21.5/$m^2$). The prototype membrane will be used to fabricate at least 6 pilot-size membrane modules (each about 20-inch length and 35 m^2 membrane area) for testing with simulated flue gas at OSU and with actual flue gas at NCCC, Wilsonville, AL using the skid to capture the CO_2 (at 60–90%) with at least 95% CO_2 purity. The prototype membrane modules will be in commercial spiral-wound configuration with a minimal pressure drop (<0.103 bar/meter (1.5 psi/meter)).

The work to demonstrate the technology will be performed in two budget periods over a 45-month schedule as follows:

Budget Period 1 (BP1):

In BP 1, we will optimize the novel transformational membrane aided by advanced computational analysis including density functional theory (DFT), characterize it, test the membrane stability, and design the skid. We will optimize the transformational membrane by taking four approaches, namely (1) investigate carrier structures aided by DFT computations; (2) incorporate nano-fillers;

(3) synthesize higher MW polyamine; (4) modify PES support. In addition, we will perform a preliminary techno-economic analysis (TEA).

Budget Period 2 (BP2):

In BP 2, we will further optimize the membrane, scale it up to the prototype size of about 20 inches wide in continuous roll-to-roll fabrication, fabricate at least 6 prototype membrane modules each with ~20-inch length and 35 m^2 membrane area, build the skid, and test it with the modules. Using the skid, we will first conduct the parametric testing using simulated flue gas at OSU and then carry out the parametric testing to achieve >60–90% capture of the CO_2 and the continuous steady-state operation to capture at least 90% of the CO_2 for >500 hours using actual flue gas at NCCC, all with at least 95% CO_2 purity. The modules will be in the commercial spiral-wound configuration for a minimal pressure drop (<1.5 psi/m or 0.103 bar/m). Based on the membrane data obtained, Gas Technology Institute (GTI) will conduct the final TEA.

2.2 Statement of Project Objectives (SOPO)

The project tasks are described in the following paragraphs.

Task 1.0 – Project Management and Planning

This task shall include all work elements required to maintain and revise the Project Management Plan, and to manage and report on activities in accordance with the plan. It shall also include the necessary activities to ensure coordination and planning of the project with DOE/NETL and other project participants. These shall include, but are not limited to, the submission and approval of required NEPA documentation. The Recipient will manage and direct the project in accordance with this SOPO and the PMP to meet all technical, schedule and budget objectives and requirements. The Recipient will work with the DOE Project Officer to make any necessary revisions to the PMP and update it as necessary to reflect the project status.

Task 2.0 – Synthesis of Improved Polymer Support

This task is to modify the PES (polyethersulfone) support for higher hydrophilic and porous characters so that it can improve membrane adhesion and decrease mass transfer resistance for increasing membrane performance. The Recipient will identify the suitable hydrophilic modifying agent for incorporation in the PES support. The Recipient will fabricate affordable PES support on our pilot casting machine for membrane synthesis needed for the project. The hydrophilic and porous membrane materials will be characterized using contact angle measurement and SEM (scanning electron microscopy), respectively.

Task 3.0 – Optimized Synthesis of Transformational Membrane

The Recipient will take following approaches:

Subtask 3.1 – Investigation of CO_2 Carrier Structures: The Recipient will use density functional theory calculations with the nudged elastic band method to identify the structures for synthesis, e.g., replacing methyl group(s) by amino group(s) for higher CO_2 capacities and reaction rates. This should facilitate the material development.

Subtask 3.2 – Incorporation of Nano-fillers: This task is to incorporate nanofillers, e.g., graphene oxide (GO) in novel membranes to increase free volume and hence CO_2 permeance.

Subtask 3.3 – Synthesis of Higher MW Polyamine: It will allow the Recipient to incorporate a greater amount of mobile carrier in the membrane, prepare a thinner membrane due to a lower concentration solution with suitable viscosity, and reduce membrane penetration into the improved porous support from the above task to achieve higher CO_2 permeance.

Task 4.0 – Membrane Characterization

The purpose of this task is to guide membrane fabrication to achieve the BP1 success criteria, and to obtain initial design parameters for the systems and cost analysis. The characterization includes:

Subtask 4.1 – Morphology of Membranes. The morphology of membranes will be characterized via scanning electron microscopy (SEM) of (cold) fracture cross-sections.

Subtask 4.2 – Transport Properties. CO_2 permeance and CO_2/N_2 selectivity of the membrane are obtained from transport measurements using simulated flue gas mixture consisting of ~ 15% CO_2, 61% N_2, 17% H_2O, 7% O_2, 3 ppm SO_2, and 3 ppm NO_2 at OSU at 1 – 4 atm and 57 – 107°C to optimize the capture cost.

Subtask 4.3 – Membrane Stability. Permeance and selectivity versus time will be obtained over 20 hours in BP1 and at least 100 hours in BP2.

Task 5.0 – Preliminary Techno-economic Analysis (TEA)

The Recipient will investigate the critical system and cost parameters for the TEA based on membrane data. This study will assure the feasibility of achieving the lowest capture cost and optimize the membrane process with respect to the system parameters. This effort will also be used to guide process and prototype membrane development.

Task 6.0 – Design of an Integrated Skid

In this task, the Recipient will discuss with the host site (NCCC) engineers on operational details associated with the installation and testing of an integrated bench skid. Lot size for the skid and utility needs will be determined. NCCC's operating philosophy will be clarified and duties for each party will be determined. The design for the skid will consist of the following subtasks:

Subtask 6.1 – Process Design. The process design consists of (1) Process Flow Diagram (PFD) and P&ID drawings with written process description, (2) Equipment, sizing and data sheets, (3) Instrumentation and data sheets, (4) Data acquisition requirements, (5) Power and controls engineering, and (6) Plant electricity, heat, water consumption, and waste generation and management tie-ins to the existing host facility.

Subtask 6.2 – Slipstream Feed Conditions. The slipstream feed conditions including pressure, temperature, flow rate, gas composition, and contaminant levels that represent the actual flue gas will be determined.

Subtask 6.3 – CO_2 Delivery Conditions. The CO_2 delivery conditions consisting of pressure, temperature, flow rate, and gas composition will be estimated.

Subtask 6.4 – Operation Procedures. The skid operation procedures including start-up, steady-state operation, and shutdown procedures for the proposed process will be prepared.

Subtask 6.5 – HAZOP Review. The Recipient will discuss with NCCC about the initial process design, perform a HAZOP review and any other necessary reviews of the technology in accordance with its guidance document for testing at NCCC. The Recipient will then compile a list of HAZOP recommendations, and an action item list will be provided along with an updated P&ID, PLC programming, mechanical fabrication, and electrical fabrication. A final design acceptance letter from the NCCC will be obtained. Any subsequent changes to the design or test plan will require NCCC and DOE acceptance. The Recipient will consult and obtain inputs from the project partner from the power industry. The Recipient will start to purchase equipment components for the skid.

Task 7.0 – NCCC Site Preparation

The Recipient will work with NCCC based on the lot size for the skid and utility needs determined for the preparation of the site at NCCC for the skid. It involves the establishment of the foundation including pouring concrete and bringing utilities in addition to the flue gas.

Task 8.0 – Construction of the Bench Skid

Based on the aforementioned detailed design, the Recipient will build the skid, which will be accomplished by the following subtasks:

Subtask 8.1 – Skid Fabrication. During the fabrication, the Recipient will ensure the progress on track in both schedule and quality according to the design while meeting all necessary design standards.

Subtask 8.2 – Equipment Installation Monitoring. The equipment selection, skid frame fabrication, pipe fabrication and installation, and equipment and instrumentation installation will all be monitored.

Subtask 8.3 – Dry-Run Testing. Finally, dry-run testing of the skid including using air for leak checking of all connections will be performed before the use of the skid for testing at OSU and NCCC.

Task 9.0 – Further Optimized Membrane Synthesis

Based on the BP1 results, the Recipient will identify the best membrane in terms of permeance and selectivity with respect to the baseline. The Recipient will further optimize the membrane synthesis for better performance in accordance with the success criteria for BP2, including the continued investigation of the synthesis approaches described in Task 3.0.

Task 10.0 – Optimized Membrane Characterization

This task is to guide membrane fabrication to the BP2 success criteria, and to obtain improved design parameters for TEA. The characterization methods and approach are the same as those for Task 4.0 in BP1.

Task 11.0 – Scale-up Membrane Fabrication

The recipient will scale up the best optimized membrane to the prototype size of 21 inches wide for 1000 feet in continuous roll-to-roll fabrication using the pilot membrane machine shown in Fig. 2 at OSU.

Task 12.0 – Scale-up Membrane Characterization

The scale-up membrane will be characterized using the methods and approach described in Task 4.0.

Task 13.0 – Prototype Membrane Module Fabrication

The scale-up membrane will be used to fabricate at least 6 prototype spiral-wound membrane modules (each skid testing uses a set of 2 modules, and the other 2 sets are spare.), each with the commercial-size 8-inch diameter by 20-inch length (half of commercial length, ~35 m^2 area). The modules are targeted for a minimal pressure drop (<0.103 bar/meter (1.5 psi/meter)).

Task 14.0 – Prototype Membrane Module Testing

The Recipient will test the membrane modules fabricated using the simulated flue gas. This task is to obtain high module performance targeting for ~4000 GPU CO_2 permeance and >140 CO_2/N_2 selectivity.

Task 15.0 – Skid Testing with Simulated Flue Gas

We will conduct the testing of the skid at OSU. Variables including CO_2 recovery (60 – 90%), retentate recycle flow rate, operating pressure and temperature will be tested to identify conditions for the parametric testing and continuous steady-state operation at NCCC. We will obtain inputs from AEP.

Task 16.0 – Skid Installation and Commissioning at NCCC

The Recipient will involve the participation of the Host Site personnel for the HAZOP reviews. A letter from the host site indicating that they accept the final results and mitigation in the HAZOP Review will be obtained.

The Recipient will involve the Host Site to the extent necessary that the Host site accepts the final designs, installation and decommissioning prior to fabrication of the field test unit (bench-scale unit or the appropriate size for your project).

The Recipient will work with NCCC to install the skid at NCCC. It involves connections to all the utilities and the flue gas. We will conduct an on-site system shakedown to ensure the system ready for testing with real flue gas. All safety reviews and operational plans will be agreed on with the NCCC personnel.

Task 17.0 – Parametric Testing of the Skid at NCCC

Upon the completion of the above task, the Recipient will work with NCCC to conduct the parametric testing of the skid with actual flue gas at NCCC. Variables including CO_2 recovery (60 – 90%), retentate recycle flow rate, operating pressure and temperature will be tested to identify conditions for the continuous steady- state operation and to provide information for final TEA.

Task 18.0 – Continuous Steady Operation of the Skid at NCCC

The Recipient will test the skid at NCCC under the steady-state conditions identified from the parametric testing. The targets are to capture at least 90% of the CO_2 with at least 95% CO_2 purity along with a minimal pressure drop (<1.5 psi/m or 0.103 bar/m) for >500 hours. After the skid testing, the Recipient will determine the identity and concentration of any possible contaminates on the membrane via laser ablation inductively coupled plasma-mass spectrometry (LA-ICP-MS), Fourier transform infrared spectroscopy (FTIR), XPS (X-ray photoemission spectrometry), and NMR (nuclear magnetic resonance spectroscopy).

Task 19.0 – Final Updated Techno-economic Analysis

The Recipient and project partner will update the TEA based on the results from Tasks 15, 17 and 18 for CO_2 capture. The final TEA will provide the lowest capture cost achievable and available through the proposed project and will be submitted at the end of the project.

Task 20.0 – Removal of the Skid from NCCC

It will be done after the completion of the skid testing.

3 Summary of Project Accomplishments

3.1 Task 1 – Project Management and Planning

Summary

- All participating students and researchers were appointed, performed productive research, and were contributing to the project.
- Training in technical reporting was provided and improved.
- Project tasks were carried out, and significant progress was made on facilitated transport-based [1], transformational membranes [2-5] for the project.
- Project updates have been communicated with DOE-NETL on a monthly basis.
- A project close-out meeting was held on March 21, 2023.
- The State Point Data Table, Technology Gap Analysis, Environmental Health and Safety (EH&S) Risk Assessment, and Technology Maturation Plan were updated and submitted to DOE on March 31, 2023.

3.2 Task 2 – Synthesis of Improved Polymer Support

Summary

- A robust A new solvent for the preparation of casting solution was identified to better preserve the bi-continuous structure of the polymer support, thereby an improved mechanical stability.
- The polymer support from the new composition of the casting solution was successfully scaled up by the roll-to-roll continuous casting machine, which exhibited a CO_2 permeance of 310,000 GPU.
- A 170-nm selective layer was successfully coated on this new polymer support to fabricate the composite membrane.

Polymer Support Synthesis Using New Casting Solution

Nanoporous polymer supports with good surface and bulk morphologies were synthesized to reduce the mass transfer resistances associated with the openness of the support layer [1-4]. The synthesis conditions have been systematically explored in the lab scale, which are transferrable to a roll-to-roll continuous casting process.

Continuous research efforts were pursued to further improve the polymer support characteristics including the surface porosity and CO_2 permeance of the polymer support. In Q3, a PES support with a bi-continuous structure was fabricated via a vapor-induced phase separation (VIPS) method, where a nonsolvent vapor was used to bring a homogeneous polymer casting solution into phase separation and to form a porous membrane.

Figure 1 (a) shows the schematic phase diagram of a polymer/solvent/non-solvent ternary system. The binodal curve delimits the two-phase region, at which a polymer-lean phase and a polymer-rich phase may coexist. The spinodal curve represents the limit of local stability, where an infinitesimal compositional fluctuation will lead to phase separation. The region between the binodal and spinodal curves corresponds to the metastable compositions, where the demixing occurs via nucleation of polymer-lean phase and the subsequent growth of the nuclei [5]. If the composition falls below the spinodal curve, however, the immediate demixing follows the spinodal decomposition mechanism [6], which leads to a bi-continuous porous structure. If the composition falls well below the spinodal curve as shown by the blue curve (*a-a'*) in Figure 1 (a), the phase separation goes through coarsening, and the polymer-lean phase eventually evolves into spotty pores in the coarsened structure as illustrated in the left, lower diagram in Figure 1 (b). Topologically, the bi-continuous structure exhibits a higher porosity and a better pore interconnectivity. The composition path of the Q5 PES support can be represented by the blue curve (*a-a'*) in Figure 1 (a), where spinodal decomposition was the primary phase separation mechanism. Therefore, this PES support exhibited a high CO_2 permeance of 310,021 GPU.

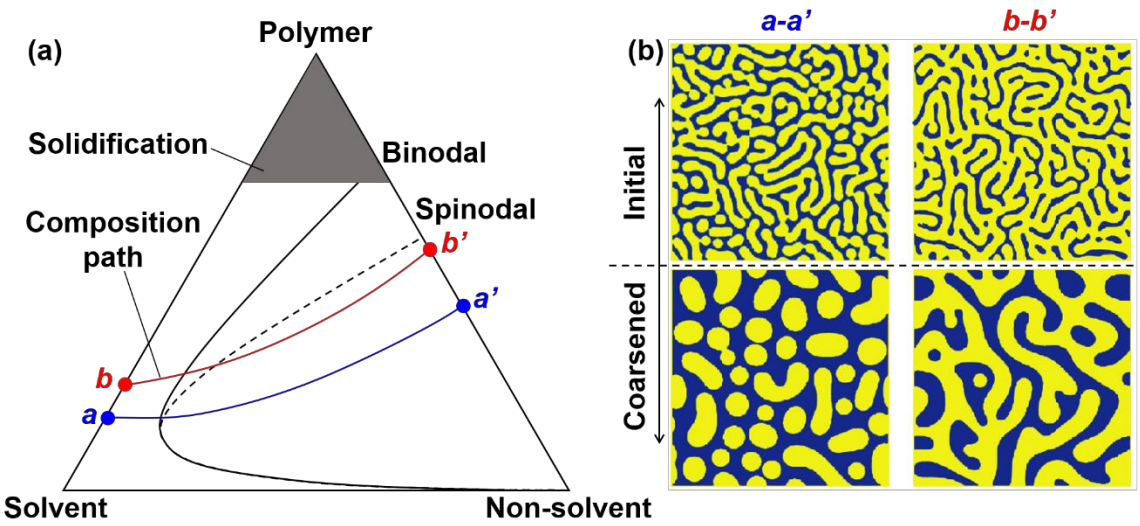

Figure 1. (a) Schematic phase diagram of polymer/solvent/non-solvent ternary system and composition paths of the Q3 PES (*a-a'* blue) and the new (*b-b'* red) casting solutions; (b) Coarsening of bi-continuous structures for *a-a'* and *b-b'* (blue = polymer-rich; yellow = polymer-lean).

Albeit the high permeance of the Q5 PES support, the selective layer coating on it was unsuccessful due to the severe penetration of coating solution into the porous support. This pitfall of the Q5 PES support stems from the evolution of the bi-continuous structure during the coarsening process. As seen in Figure 1 (a), a spinodal decomposition could occur instantaneously after the exposure to the non-solvent vapor [7]. However, after the formation of the nascent bi-continuous structure in a phase separating casting solution, the polymer-rich phase continues to evolve because of its tendency to reduce the surface energy related to the interfacial area [8]. During this coarsening process, the morphology of the polymer-rich phase keeps developing until it reaches the solidification region. Therefore, the retainment of the nascent bi-continuous structure is reversely proportional to the coarsening rate [9-11].

The coarsening rate (u) is correlated to the interfacial tension σ and the solution viscosity η as $u \propto \sigma/\eta$ [12]. In order to induce the spinodal decomposition, a low PES concentration was used for the Q1 support, which resulted in a low casting solution viscosity. Therefore, the nascent bi-continuous structure has a higher tendency to coarse into a highly opened but spotty structure as shown on the left side of Figure 1.1 (b). This process enlarges the porous region of the Q5 support, which induces the penetration of the coating solution.

In order to better retain the bi-continuous structure for improved coating quality, a new solvent was used to prepare the casting solution, which yielded a more concentrated casting solution with a higher viscosity. As shown by the red composition path (*b-b'*) in Figure 1 (a), which is closer to the spinodal cure, a bi-continuous structure can still form by the VIPS of the new casting solution, but the bi-continuous structure could be largely retained due to the fast solidification of the polymer-rich phase as illustrated by the right side of Figure 1 (b).

The new polymer support was successfully scaled up by a roll-to-roll casting machine [2,3,13,14], and the representative SEM images are shown in Figure 2. Figure 2 (a) depicts the surface morphology of the polymer support whereas Figure 2 (b) shows the cross-section morphology of the support. As shown in Figure 2 (b), the new support exhibited a morphology with bi-continuous structure on the top and macrovoids near the bottom. The formation of macrovoid was another indicator of the better solvency of the new solvent to PES. In this case where the polymer chains were well soluble in the solvent and had less entanglement, the casting solution away from the surface, i.e., next to the mechanical support of the nonwoven fabric, was disturbed by the fast solvent/non-solvent exchange, with the nonsolvent coming from the nonwoven fabric side to cause the demixing phase separation, before the spinodal decomposition occurred, thereby the formation of macrovoid [15].

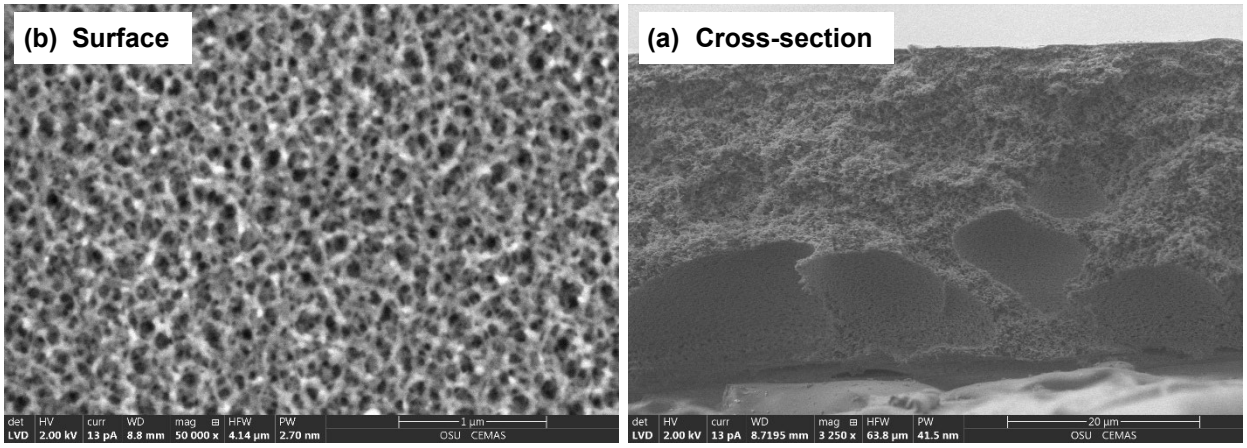

Figure 2. SEM images of the new PES support fabricated by the continuous casting machine: (a) surface and (b) cross-section.

In order to quantify the mass transfer resistance of the novel polymer support, its CO_2 permeance was measured by a Wicke-Kallenbach permeation apparatus as described in our previous work [16]. This scaled-up new support showed a very high CO_2 permeance of 310,000 GPU. The SEM morphologies and transport property of the scale-up support were on par with the support fabricated in lab scale. The selective layer coating was also successfully carried out on this novel polymer support; the transport measurement will be discussed in Task 4.

3.3 Task 3 – Optimized Synthesis of Transformational Membrane

Summary

- The carrier diffusivity, as well as N_2 diffusivity and solubility, was computationally quantified for carriers C1D12–C1D16. Compared to Carrier 1, although these newly proposed carriers demonstrated a smaller carrier diffusivity, they rendered a slower N_2 diffusion and a reduced N_2 solubility.
- C1D12–C1D16 demonstrated stronger interactions with the polymer than Carrier 1 and therefore were expected to offer improved membrane stability.

- A new parameter, N exposure, was introduced to quantify the steric hindrance effect of carriers and correlate with the reaction chemistry. In general, the reaction chemistry improved with reducing N exposure (i.e., stronger steric hindrance effect).
- A new iterative ReaxFF optimization algorithm was proposed to improve the accuracy and stability.
- The computationally evaluated carrier C1D11 was successfully synthesized, which can potentially improve the long-term membrane stability.
- The synthesis of pBuC1, a homopolymer with reactive sites resembling Carrier 1, was improved to increase its MW to 270 kDa.
- Alternatively, a terpolymer with reactive sites resembling Carrier 1 as pendant groups was also synthesized to serve as a fixed-site carrier.

Theoretical Evaluation of New Mobile Carriers

A new set of mobile carriers (MCs) (i.e., C1D12–C1D16, see Figure 3) was proposed based on C1D11 and computationally demonstrated their desirable reaction chemistry. In order to further investigate their potential as MCs in facilitated transport membranes (FTMs), the carrier diffusivity, as well as N_2 diffusivity and solubility, was computationally quantified for each carrier. In addition, the polymer–MC interactions were also evaluated to determine whether the projected membrane stability of C1D11 can be preserved.

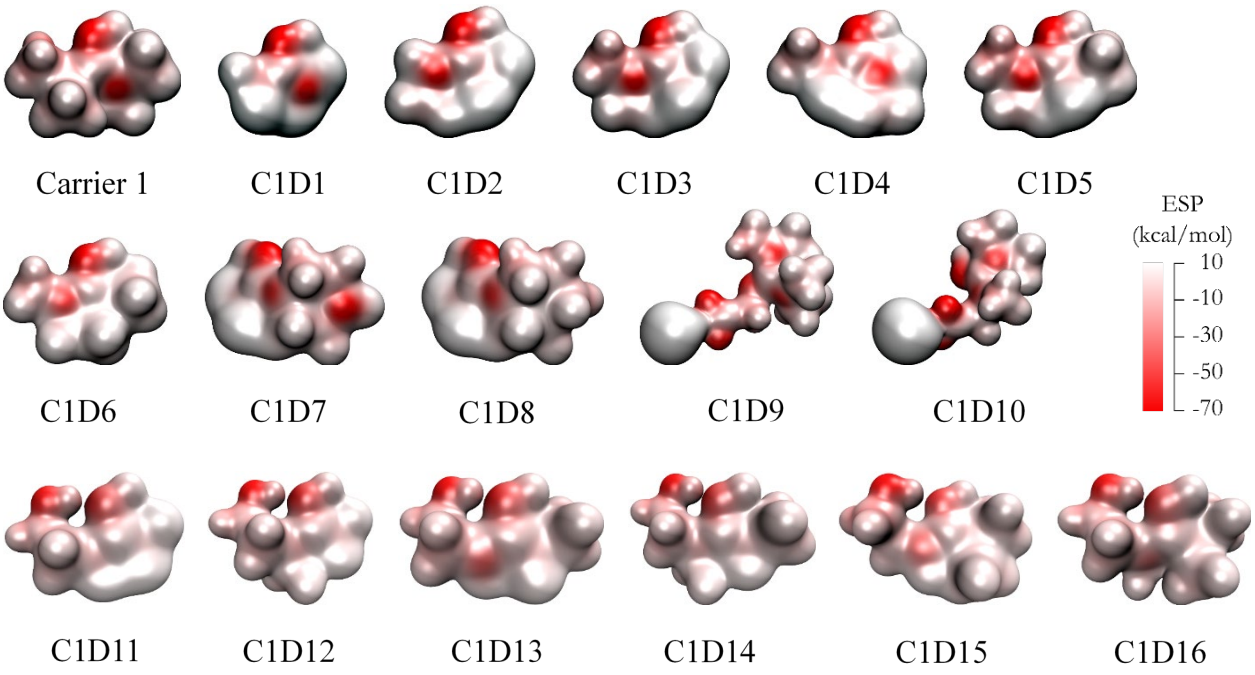

Figure 3. Electrostatic potential (ESP) maps of Carrier 1 and proposed carrier structures (C1D1–C1D16). Warmer color refers to lower ESP.

MC Diffusivity: Similar to C1D11, the diffusivities of C1D12–C1D16 were computed based on molecular dynamics (MD) trajectories at 200 wt.% water uptake (i.e., $m_{water}/m_{dry\ membrane} \times 100$ wt.%). The computed diffusivities are shown in Figure 4 with diffusivities of C1D11 and Carrier 1 included for comparison. It is clear that since C1D12–C1D16, by design, inherited the unique hydrogen bond donor group of C1D11, they also suffered from the rather low carrier diffusivity due to the strong interactions with the surrounding water molecules. Consequently, the carrier diffusivities of C1D12–C1D16 were still lower than that of Carrier 1. However, these newly proposed MCs demonstrated slightly improved carrier diffusivities relative to C1D11, suggesting their improved efficiency in facilitating the transport of CO_2.

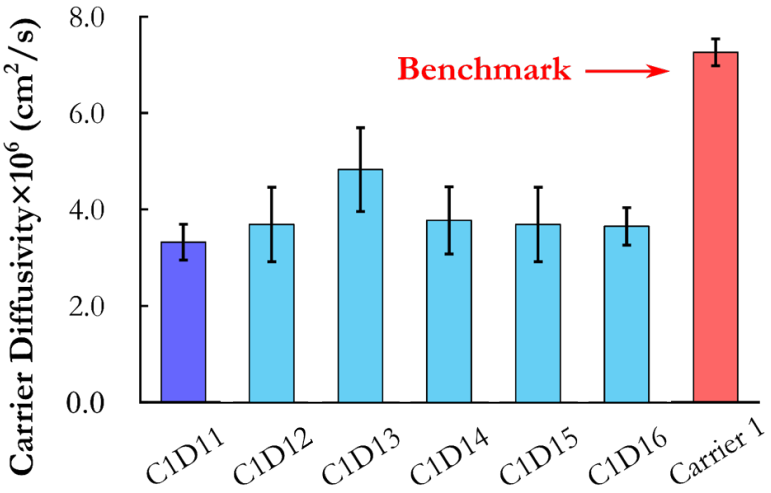

Figure 4. The computed diffusivities of C1D11, C1D12–C1D16, and Carrier 1 at 200 wt.% water uptake.

N_2 Diffusivity and Solubility: The N_2 diffusivity and solubility are critical as they affect the selectivity of the FTM. The N_2 diffusivity values in C1D12–C1D16 were theoretically evaluated using MD simulations and the solubility values using Monte Carlo calculations. The diffusivities and solubilities of N_2 in C1D12–C1D16 are summarized in Figure 5 (a) and (b), respectively. The values of Carrier 1 and C1D11 are also shown for comparison. As seen, consistent with the carrier diffusivities, C1D12–C1D16 demonstrated N_2 diffusivities and solubilities that were slightly higher than C1D11 but lower than Carrier 1. Therefore, these newly proposed MCs are expected to yield higher N_2 permeabilities as compared to C1D11, but the N_2 permeabilities should still be lower than that of Carrier 1. The reduced N_2 diffusivity and solubility as compared to Carrier 1 can also be attributed to the strong interactions between the MCs and surrounding water molecules.

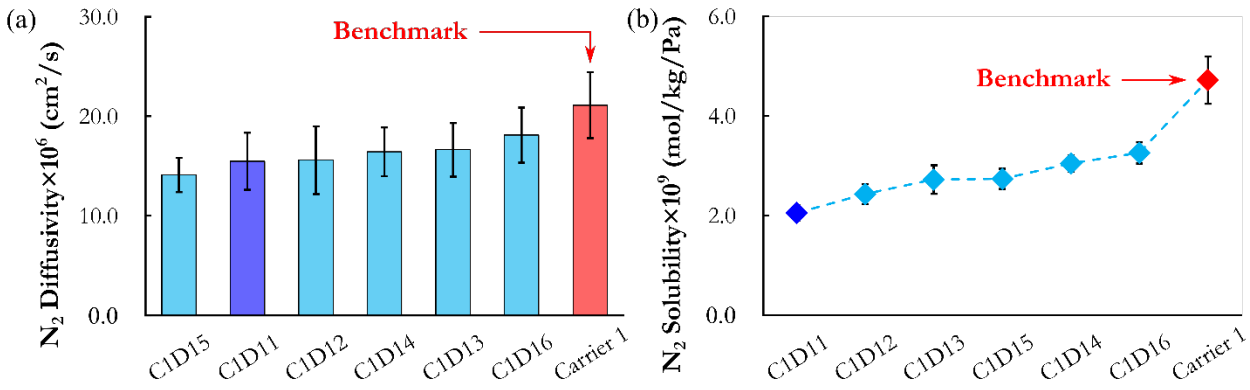

Figure 5. The computed (a) diffusivity and (b) solubility values of N_2 in C1D11, C1D12–C1D16, and Carrier 1 at 200 wt.% water uptake.

Membrane Stability: C1D11 demonstrated stronger interactions with the polymer chain and consequently a better membrane stability as compared to Carrier 1. The same group was preserved in C1D12–C1D16 while the surrounding groups were systematically modified. In order to understand the membrane stability of C1D12–C1D16, the polymer–MC interactions were also computed using MD simulations at 100 wt.% water uptake. The average polymer–MC interactions of C1D11, C1D12–C1D16, and Carrier 1 are summarized in Figure 1.6. Compared to C1D11, the modified structures of C1D12–C1D16 resulted in moderately reduced interactions with the polymer chain. This less favorable interaction is likely responsible for their slightly higher carrier diffusivities, as well as the higher N_2 diffusivities and solubilities. However, they still possessed stronger interactions with the polymer chains as compared to Carrier 1 and thereby a better membrane stability.

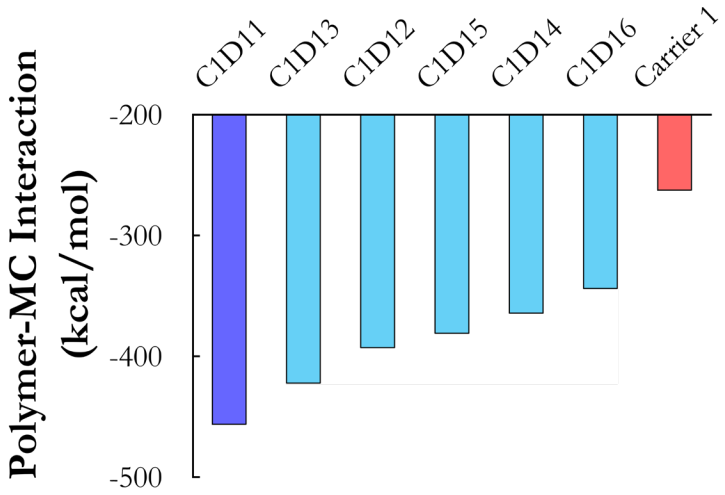

Figure 6. Average polymer–MC interactions of C1D11, C1D12–C1D16, and Carrier 1 at 100 wt.% water uptake.

In summary, C1D11 and its structural variations (i.e., C1D12–C1D16) demonstrated lower carrier diffusivities as compared to Carrier 1, which would potentially limit their ability to facilitate the CO_2 transport in FTMs. However, these MCs were expected to offer a slower N_2 permeation given their lower N_2 diffusivities and solubilities. Moreover, they exhibited desirable reaction chemistry (i.e., positive $\Delta\Delta E$ values or a preference towards bicarbonate pathway) that would lead to higher CO_2 loading capacities, as well as more favorable interactions with the polymer chain for enhanced membrane stability. Therefore, these MCs may still pose significant interest as promising candidates. Carrier C1D11 has been successfully synthesized.

Steric Hindrance Effect of MCs

To date, 14 MC structures (i.e., C1D1–C1D8 and C11D11–C11D16) have been proposed based on the structure of Carrier 1. While they all possess the unique reactive group of Carrier 1, the chemical environment around the reactive N was altered in each carrier, which resulted in different reaction chemistry. Understanding how the reaction chemistry changes with the chemical environment of the reactive N is crucial for the future screening and evaluation of carrier structures. However, the quantitative description of the influence of chemical environment is absent and therefore needs to be first defined.

The steric hindrance effect of the reactive N, which quantifies the degree of difficulty to access the reactive N imposed by the surrounding functional groups, is known to be a key factor in determining the amine–CO_2 reaction chemistry. Specifically, the N site of a primary amine in the absence of bulky substitutions is largely accessible (i.e., exposed); therefore, it is considered sterically unhindered (i.e., with low steric hindrance effect). In contrast, when an alkyl group is attached to the N site, the alkyl group effectively blocks a portion of the resultant secondary N and makes it sterically hindered (i.e., with higher steric hindrance effect). Sterically hindered amines generally tend to react with CO_2 to form bicarbonate since the strong steric hindrance could lead to unstable carbamate products [17]. In order to quantitatively probe such an effect, we introduced a new parameter, N exposure value, to quantify the accessibility of the reactive N site. The N exposure value was calculated as the ratio of the accessible (i.e., exposed) surface area of the reactive N site with respect to its van der Waals surface area. A probe (radius = 1.0 Å) was employed to determine the accessible surface area in all N exposure calculations. The calculation process is illustrated in Figure 1.7 using the N site of glycine as an example. Its accessible surface accounts for 52.56% of the total van der Waals surface area, meaning that the N exposure value of glycine is 52.56%.

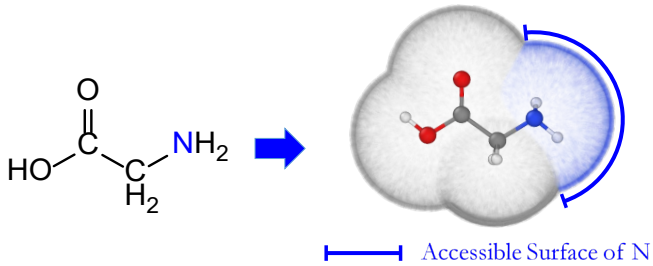

Figure 7. Illustration of the N exposure using glycine as an example. The probe was rolled over the glycine molecule to detect the accessible surface. The accessible surface of N is highlighted in blue while the rest in grey.

Following the same calculation process, the N exposure values of Carrier 1 and other proposed MC structures were calculated and correlated to the reaction chemistry (i.e., ΔΔE values) in Figure 8. As expected, the reaction chemistry indeed improved (i.e., ΔΔE value increased) with a lower N exposure value (i.e., stronger steric hindrance effect). This evidences that the newly proposed N exposure value may serve as a reliable indicator of the reaction chemistry in the evaluation of promising carrier structures. It is important to note that the computational cost of the N exposure value is negligible compared to the expensive DFT calculation of reaction chemistry, thus enabling an efficient future screening of potential carrier structures. More amines will be evaluated for their ΔΔE and N exposure values to further validate the observed correlation. In addition, the relationship between N exposure and reaction kinetics will also be explored.

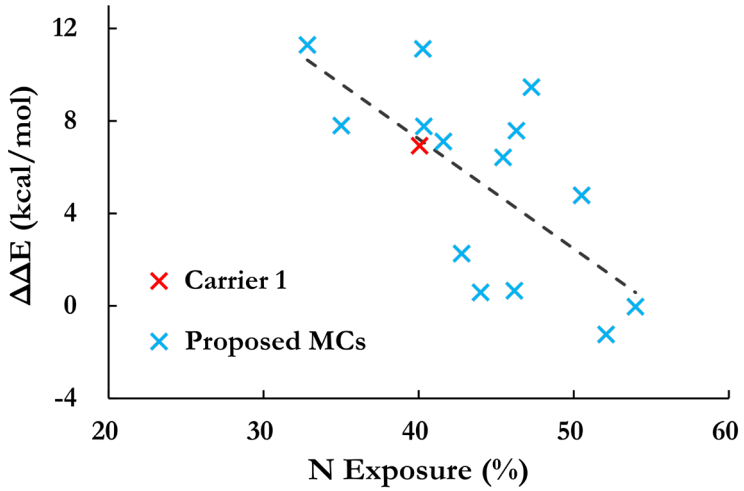

Figure 8. Correlation between the N exposure and ΔΔE values of Carrier 1 and proposed MC structures.

Optimization of Reactive Force Field

Reactive force fields (ReaxFFs) can enable studies of both the physical and chemical properties of molecular systems. Since ReaxFF is a heavily specialized force field, currently available ReaxFFs for glycine (Gly ReaxFF) [18] and tetrabutylphosphonium glycinate (TGly ReaxFF) [19] could not reproduce the inter/intra-molecular of Carrier 1 and its reaction with CO_2 correctly. A new optimization approach was proposed. The ReaxFF was first trained to reproduce the inter-molecular interaction (i.e., bulk-phase density), followed by a parameterization to resemble the DFT-computed intra-molecular interactions and reaction energy profiles.

After the training for the inter/intra-molecular interactions, the optimized ReaxFF was able to reproduce the bulk-phase density (i.e., 0.93 g/cm^3 by the optimized ReaxFF vs. 0.91 g/cm^3 measured experimentally) and the intra-molecular interaction training set (i.e., DFT calculated energy profiles) with a mean absolute error (MAE) of ca. 4.5 kcal/mol. Subsequently, the ReaxFF was trained for the reaction, and the optimized ReaxFF successfully reproduced the energy profiles along both carbamate and bicarbonate reaction pathways (i.e., MAE of ca. 0.4 kcal/mol) with the bulk-phase density calculated to be 0.94 g/cm^3. However, the training for the reaction energy made the ReaxFF deviate from the DFT-computed intra-molecular interactions, resulting in an increased MAE of ca. 8.0 kcal/mol. Also, MD simulations using the optimized ReaxFF on Carrier 1 sometimes resulted in unphysically broken bonds, which might be due to parameter over-fitting. Therefore, a critical task is to further improve the accuracy and stability of the ReaxFFs to maximize the performance.

New Iterative Training Algorithm: It was found that the instability might be attributed to the insufficient optimization on the intra-molecular interaction and geometrical features. A new test set was generated by conducting MD simulations with the previously "optimized" ReaxFF at 300 K and then compared with the DFT energy. As denoted as the "Iteration 1" in Figure 1.9, this "optimized" ReaxFF led to a large deviation from the DFT energy for this newly generated test set, although its MAE for the training set was only 4.3 kcal/mol. This clearly suggested that the training set might not sufficiently sample the potential energy surface of Carrier 1, leading to an over-fitting optimization and thus instability of the obtained ReaxFF. For this, a new optimization algorithm was proposed as shown in Figure 1.10. After the parameterization, new test sets are generated and compared with the DFT energy. If the MAE for a test set is larger than 4 kcal/mol, this test set is used as the training set for a new iteration until the MAE for the test set is below 4 kcal/mol. Following the new algorithm, the MAE for the test set indeed reduced significantly, as shown in Figure 1.9 and Table 1. From Iteration 1 to 3, the MAE for the test set decreased from 9.8 to 2.4 kcal/mol, while the MAE for the training set also reduced from 4.3 to 2.5 kcal/mol. Thus, it is important to continue conducting the iterative intra-molecular interaction training.

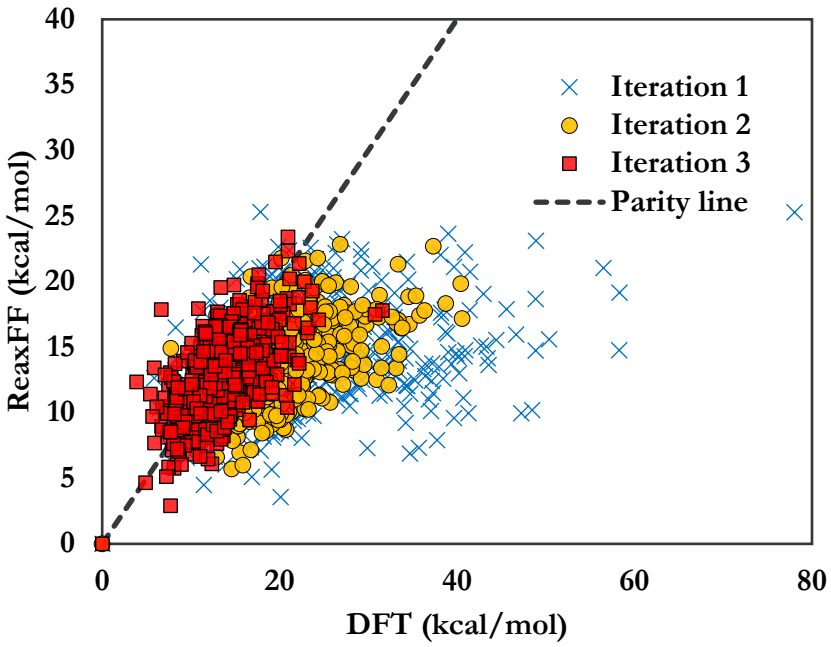

Figure 9. Comparison of the energies calculated by DFT and optimized ReaxFF for the test set of each iteration.

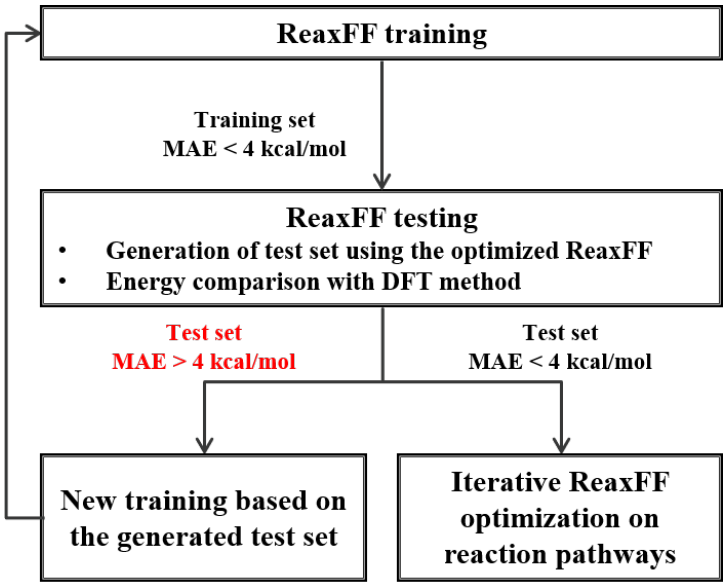

Figure 10. New optimization algorithm proposed to increase the accuracy and stability of ReaxFF.

Table 1. MAE of the energies calculated by optimized ReaxFF compared to DFT method.

# Iteration	MAE (kcal/mol)	
	Training Set	Test set
1	4.3	9.8
2	3.8	6.5
3	2.5	2.4

Synthesis of Novel Fixed-Site Carriers—Homopolymers

The synthesis procedure of a homopolymer with reactive sites resembling Carrier 1 (C1) was further improved in order to increase its MW and better serve as fixed-site carrier. Poly(butylene C1) (pBuC1) was synthesized by the polycondensation of a bifunctional monomer with a butylene linkage and a trifunctional monomer in the presence of an acidic catalyst (see Figure 11). In brief, the monomers and catalyst were initially heated at 140°C under nitrogen protection. The polycondensation reaction then started to kick off a low MW, volatile byproduct, which was continuously removed from the reactants by vacuum distillation at 10 torr and 180°C. After certain reaction duration, the crude product was first washed by a polar aprotic solvent and then dialyzed against water exhaustively to remove any residual monomers and catalyst. The purified polymer was then ion-exchanged to activate the C1 functional groups. After the purification, the MW values of different pBuC1 samples were analyzed by static light scattering (SLS) [20].

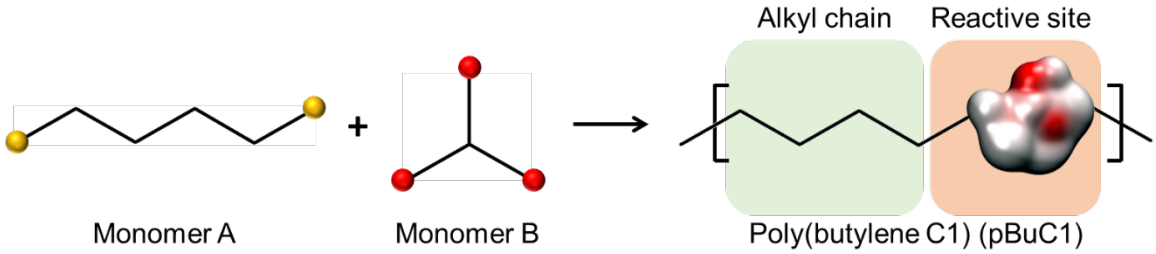

Figure 11. Synthesis scheme of pBuC1 by a bifunctional Monomer A and a trifunctional Monomer B.

In order to optimize the synthesis conditions for pBuC1, four batches of polymers were synthesized and the conditions are summarized in Table 2. The photos of the polymer samples and the MWs are shown in Figures 12 and 13, respectively. For Samples A–C, the reaction time was extended while maintaining a relatively stable vapor temperature throughout the polymerization at 180°C. With the prolonged polymerization time, the polymer sample became less powdery, accompanied with an increased MW from 26 to 68 kDa. The amount of catalyst was then increased for Sample D while maintaining the extended polymerization time. As shown in Figure 12 (D), the sample was no longer powdery; the exhibited transparency indicated a long-range change packing, which was a consequence of the increased MW [21]. SLS experiment showed that the MW of Sample D was 270 kDa.

Table 2. Synthesis conditions for pBuC1.

Sample	Monomer content	Catalyst content	Temperature (°C)	Vacuum (torr)	Reaction time
A	High	Moderate	180	10	Short
B	High	Moderate	180	10	Medium
C	High	Moderate	180	10	Long
D	High	High	180	10	Long

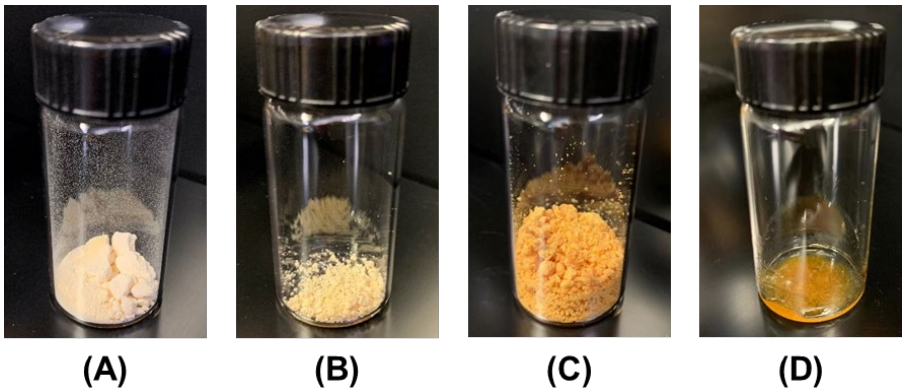

Figure 12. Photos of different pBuC1 samples with synthesis conditions as listed in Table 2.

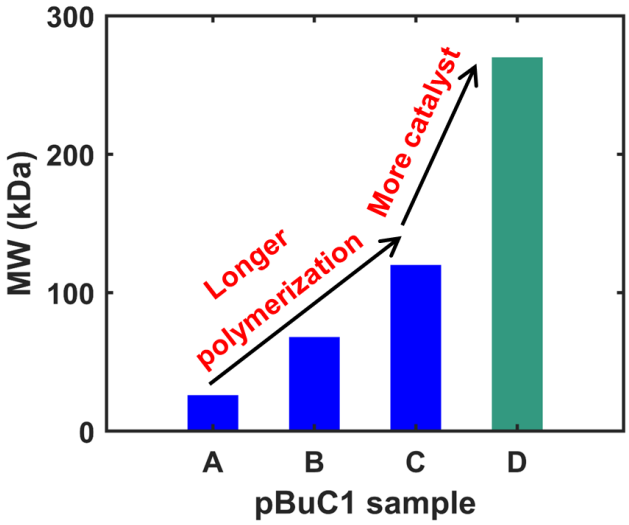

Figure 13. MWs of different pBuC1 samples with synthesis conditions as listed in Table 1.2.

Synthesis of Novel Fixed-Site Carrier—Terpolymer

A random copolymer was synthesized as an alternative approach to prepare the fixed-site carrier. As shown in Figure 14 (a), a fraction of the amino groups in polyvinylamine (PVAm) was

modified to a functional group resembling Carrier 1. Hereafter, this copolymer is referred as poly(vinylamine-*ran*-vinyl C1) (PVAm-*ran*-PVC1). For a copolymer with 50 mol.% of the amino groups converted to the C1 functional groups, the resultant PVAm-*ran*-PVC1 was found to be unstable, i.e., precipitated out, in aqueous medium. The instability might be due to the stacking of the C1 groups, which led to the aggregation of the polymer chains.

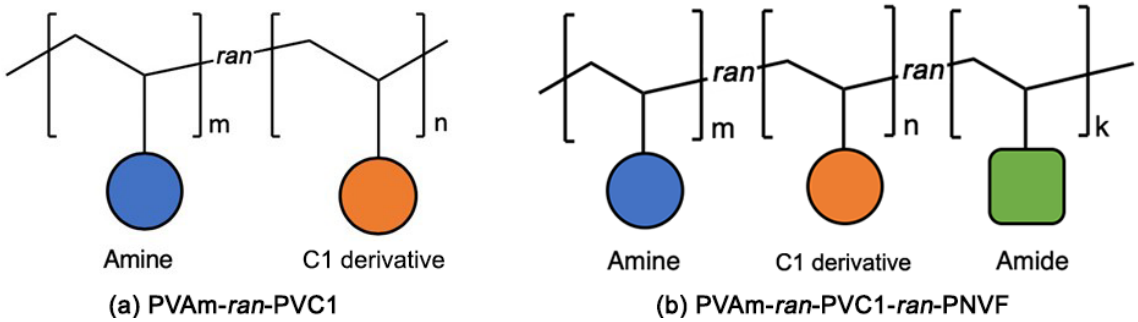

Figure 14. Schematic diagrams of (a) poly(vinylamine-*ran*-vinyl C1) (PVAm-*ran*-PVC1) and (b) poly(vinylamine-*ran*-vinyl C1-*ran*-*N*-vinylformamide) (PVAm-*ran*-PVC1-*ran*-PNVF).

In order to address the stacking issue, *N*-vinylformamide repeating units were copolymerized with PVAm-*ran*-PVC1, resulting in a terpolymer poly(vinylamine-*ran*-vinyl C1-*ran*-*N*-vinylformamide) (PVAm-*ran*-PVC1-*ran*-PNVF). The terpolymers were synthesized with 15–50 mol.% amide group. The stacking problem mentioned earlier in PVAm-*ran*-PVC1was not observed in these PVAm-*ran*-PVC1-*ran*-PNVF samples. The improved stability might be due to the case that the additionally introduced amide groups, which can form strong hydrogen bonds with water.

Synthesis of Proposed Potential Mobile Carrier

As discussed by the computational work, C1D11 and its derivatives could exhibit a better stability in the membrane owing to the additional functional group that is capable of forming hydrogen bond (HB) with the polymer matrix. In order to demonstrate such an effect, C1D11 was synthesized based on the scheme as shown in Figure 15. As seen, an amine substrate containing the HB donor was reacted with a compound containing the C1 segment, which afforded C1D11 as one of the products. The successful synthesis of C1D11 and a purity of greater than 90% were confirmed and determined by ^{1}H NMR and ^{13}C NMR.

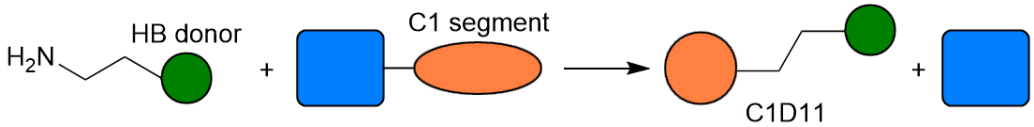

Figure 15. Synthesis scheme of C1D11 from an amine substrate containing the hydrogen bond (HB) donor.

3.4 Task 4 – Membrane Characterization

Summary

- A gravimetric method was developed to measure the CO_2 sorption in facilitated transport membranes under flue gas conditions.
- A composite membrane coated on the new polymer support showed a high CO_2 permeance of 3670 GPU and a CO_2/N_2 selectivity of 155 at 77°C.

CO_2 Sorption in Facilitated Transport Membrane

In order to understand the origin of the high CO_2/N_2 separation performance of FTM, a gravimetric method was developed to study the sorption of CO_2 in FTM. A well-studied FTM (developed in DE-FE0026919) containing PVAm as the fixed-site carrier and 2-(1-piperazinyl)ethylamine salt of sarcosine (PZEA-Sar) as the mobile carrier was used to calibrate the system [16,22]. Free-standing films containing 0–85 wt.% PZEA-Sar were prepared, and the sorption experiments were carried out using a Cahn Thermax 500 high-pressure thermal gravimetric analysis (HPTGA, Thermo Electron Corp., Newington, NH). The test sample was first purged with dry argon overnight to fully desorb any CO_2 and moisture. The sample was then exposed to a wet argon saturated with water vapor (0.172 atm) at 57°C until equilibrium. Afterwards, CO_2 fully saturated at 57°C was introduced to the HPTGA. The sample weight was then recorded every second during the experiment. The CO_2 solubility was calculated as the amount of CO_2 sorbed in the sample normalized by the sample volume and CO_2 partial pressure. A common unit for solubility is $cm^3(STP)\ cm^{-3}\ atm^{-1}$ [1]. Based on the transient increment of sample weight, the apparent CO_2 diffusivity was determined assuming Fickian diffusion [23].

The measured CO_2 solubility and apparent diffusivity values are presented in Figure 16. Also shown in this figure are the data for several non-reactive polymers, including polyethers [24-26], polyimides [27], and polynorbornenes [28]. As seen, these FTMs exhibited CO_2 solubilities that were 2–3 orders of magnitude higher than those of non-reactive polymers. The high solubility was attributed to the chemisorption of CO_2 in the presence of amine carrier molecules. The apparent CO_2 diffusivities, however, were in the order of $10^{-8}\ cm^2\ s^{-1}$ and were lower than those of polyethers and highly glassy polynorbornenes. The low diffusivity was likely caused by the strong Coulombic interaction in the presence of the mobile carrier, PZEA-Sar, an aminoacid salt. Apparently, the fast CO_2 permeation in these FTMs mainly stemmed from the strong chemisorption of CO_2.

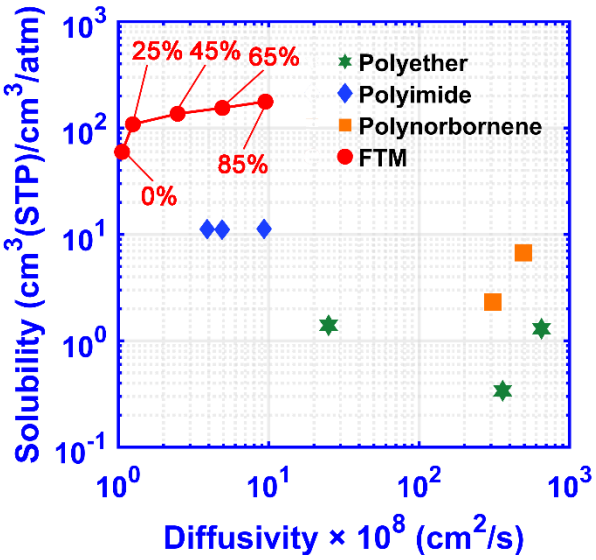

Figure 16. Solubility and apparent diffusivity values of CO_2 in FTMs containing 0–85 wt.% PZEA-Sar as compared with several non-reactive polymers: polyethers [24-26]; polyimides [27]; polynorbornenes [28].

In addition, both the CO_2 solubility and diffusivity increased significantly with increasing content of PZEA-Sar. Specifically, the addition of 85 wt.% PZEA-Sar led to a CO_2 solubility of 177 cm^3(STP) cm^{-3} atm^{-1} and a CO_2 diffusivity of 9.5×10^{-8} cm^2 s^{-1}, which were ca. 3 and 9 times higher than those of pure PVAm. This observation further emphasizes the importance of mobile carrier.

Membranes on New Polymer Support

The composite membrane coated on the aforementioned new polymer support (from Task 2) was tested at 77°C with feed and vacuum pressures of 4 and 0.8 atm, respectively. The transport performance of this membrane is shown in Figure 17. Also shown in this figure are the membrane performances on some other polymer supports, including the baseline PES (developed in DE-FE0026919), the Q3 PES support, and the high-T_g polymer support (also in Q3). As seen, a more permeable polymer support resulted in a higher CO_2 permeance of the composite membrane. The new polymer support developed rendered a CO_2 permeance of 3670 GPU and a CO_2/N_2 selectivity of 150. The improved permeance was attributed to (1) the reduced mass transfer resistance in the polymer support and (2) the reduced lateral diffusion at the selective layer/support interface due to the increased surface porosity of the polymer support [2,13,29]. Compared to the membrane coated on the baseline PES support, the continuous improvement on the polymer support has rendered an increase in the composite membrane permeance of ca. 500 GPU.

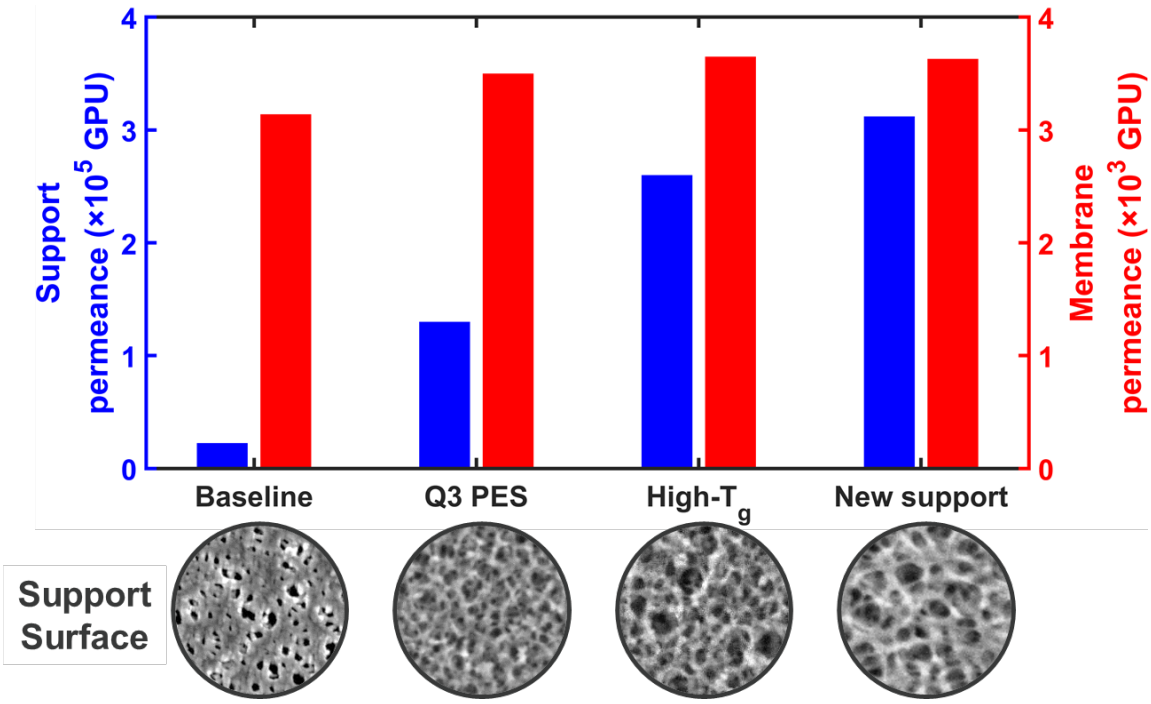

Figure 17. CO_2 permeances of different polymer supports and the CO_2 permeances of the corresponding composite membranes.

3.5 Task 5 – Preliminary Techno-Economic Analysis

Summary

- The carrier saturation phenomenon (CSP) of membrane containing Carrier 1 was modeled in order to be implemented in the process model.
- If the CSP is considered, the membrane area required for 90% CO_2 removal can be reduced by 10%.
- The reduced membrane area renders a cost reduction from $40.20 to $39.60/tonne.

Modeling of CSP

Figure 18 shows the CO_2 and N_2 permeances at 77°C and 4 atm for feed gases containing 0.1% – 20% CO_2. As seen, the CO_2 permeance reduced with increasing CO_2 partial pressure. The initial non-linear decrease of CO_2 permeance indicated the consumption of free amine carriers in the membrane [30,31]. When the entirety of the amine carriers had reacted with CO_2, a transition to a permeance plateau was observed. For the range of CO_2 partial pressure that was relevant to carbon capture from coal-derived flue gas, a decent increase in CO_2 permeance could be achieved upon the bulk removal of CO_2. For instance, the CO_2 permeance can increase from 3,511 to 4,002 GPU when the CO_2 partial pressure reduced from 71.8 to 3.6 kPa (i.e., 20% CO_2 to 1% CO_2 at 4 atm).

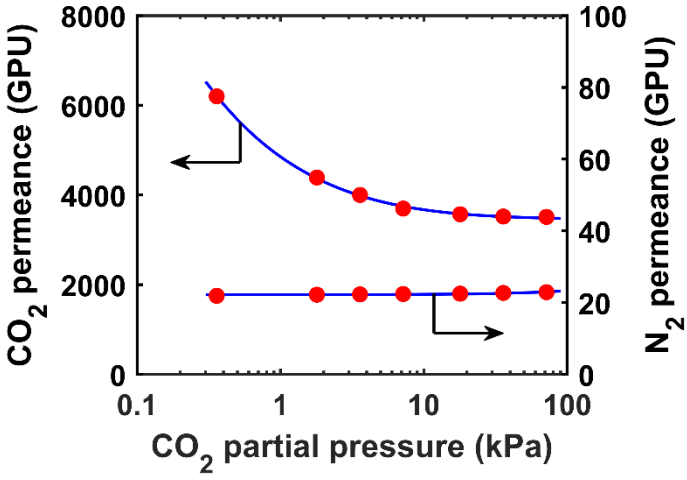

Figure 18. CO_2 and N_2 permeances at various CO_2 partial pressures at 77°C. The solid lines are the best fits based on the facilitated transport model in our previous work [32].

The N_2 permeance, however, was nearly independent on the CO_2 partial pressure. Since the CO_2 permeance increased with reducing CO_2 partial pressure, the CO_2/N_2 selectivity also increased accordingly. For instance, when feed CO_2 concentration was reduced from 20% to 1%, the selectivity increased from 153 to 179, resulting in a more selective separation. Overall, the increasing CO_2 permeance and selectivity can reduce the total membrane area and benefit the process economics.

The upper blue line in Figure 19 is the best fit of a theoretical facilitated transport model, which takes the form

$$\frac{P}{\ell} = \frac{P_0}{\ell}\left[1 + \eta\left(\sqrt{1 + \frac{p^*}{p^h}} - 1\right)\right] \tag{1}$$

where P/ℓ is the CO_2 permeance, P_0/ℓ is the CO_2 permeance in the absence of facilitated transport, and p^h is the feed CO_2 partial pressure. η and p^* are the two parameters characterizing the carrier saturation phenomenon, where η measures the contribution of the facilitated transport, and p^* represents an onset CO_2 partial pressure for carrier saturation. As indicated by Eq. (1), $P/\ell \to P_0/\ell$ if $p^h \gg p^*$, implying the vanish of facilitated transport due to the complete carrier saturation [32]. As seen, the model fits the experimental data reasonably well. The fitting parameters are listed in Table 3. This simplified equation is used to model the dependence of CO_2 permeance on the feed CO_2 partial pressure in the techno-economic modeling.

Table 3. Values of fitting parameters of the facilitated transport model.

Parameter	P_0/ℓ (GPU)	η (–)	p^* (kPa)
Value	3450	0.290	5.011

Effects of CSP on System Footprint and Capture Cost

In order to demonstrate the effect of CSP, the membrane areas for 90% CO_2 recovery at various η and p_A^* values are calculated. The results are shown in Figure 19, where a feed-to-permeate pressure ratio ($\gamma = p^h/p^l$) of 10 is employed. The $P_{A,0}/\ell$ is fixed at its value at 77°C shown in Table 3. The normalized membrane area is defined as $s = A_0/\left[\frac{n^h|_{A=0}}{p^h(P_{A,0}/\ell)}\right]$, where A_0 is the membrane area, $n^h|_{A=0}$ the feed molar flow rate, and p^h the feed pressure.

As seen in this figure, p_A^* determines the fraction of membrane that is under the mitigated carrier saturation, while η measures the contribution to the overall CO_2 permeance by the extra free amine carriers made available by the reduced partial pressure. Not surprisingly, the membrane area reduces significantly with increasing p_A^* and η, which validates the reduced membrane area by the increasing CO_2 permeance upon bulk CO_2 removal. The two red markers in the figure represent the calculated membrane area based on the experimentally measured transport results with and without considering the CSP. It is readily obvious that less membrane area is required when the CSP is considered. The membrane area reduces by 10.2% compared to the case where the CSP is not considered (i.e., η = 0).

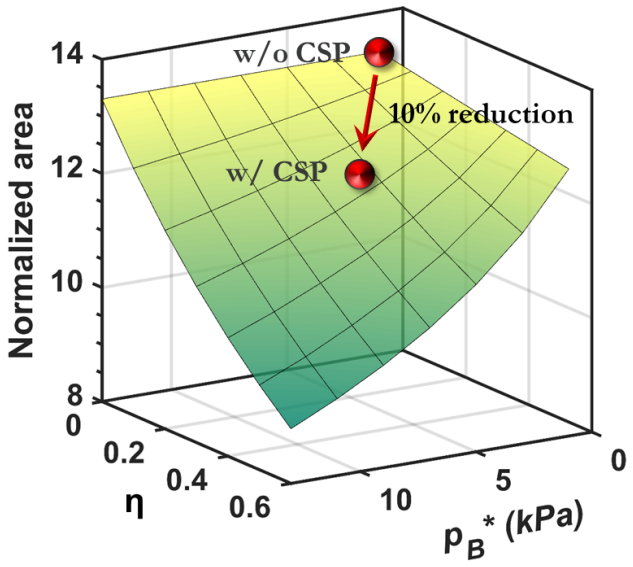

Figure 19. Effect of carrier saturation behavior on membrane area for a feed-to-permeate pressure ratio (γ) of 10. The red markers are generated based on the experimentally measured transport results at 77°C as shown in Figure 18.

In order to quantify the effect of CSP on the process economics, the capture costs for 90% CO_2 recovery at various η and p_A^* values are calculated, and the results are shown in Figure 20. The $P_{A,0}/\ell$ is fixed at its value at 77°C shown in Table 3. The N_2 permeance at 77°C is fixed at 23 GPU; the water permeance is assumed the same as $P_{A,0}/\ell$ and is not composition-dependent; the permeation of O_2 is neglected. The feed pressure and permeate vacuum pressure are fixed at 4 and 0.4 atm, respectively, and a 15% retentate recycle is used. As seen, the capture cost reduces with increasing η and p_A^*, which is in line with the trend illustrated in Figure 19. Therefore, a membrane

with less extent of carrier saturation is beneficial for reducing the system footprint and capital investment. The green markers in this figure represent the calculated cost based on the experimentally measured transport results at 77°C as shown in Figure 18. Compared to the case where the CSP is not considered (i.e., η = 0), the capture cost is reduced from $40.20 to $39.60/tonne. These results also imply that the carrier saturation does not affect the operation of the FTM adversely with a feed pressure as high as 4 atm.

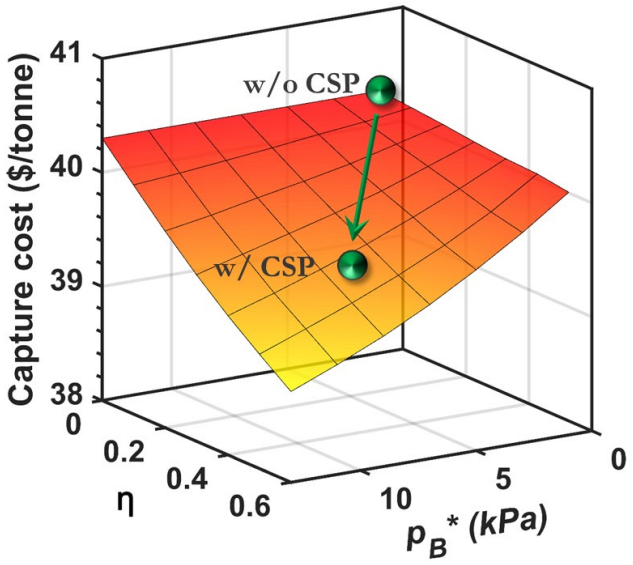

Figure 20. Effect of carrier saturation behavior on capture cost. The green markers are generated based on the experimentally measured transport results at 77°C as shown in Figure 18.

3.6 Task 6 – Design of an Integrated Skid

Summary

- The engineering design of 35-m^2 spiral-wound (SW) module (⌀8″, 20″ length) has been conducted.
- Effective utilization of the membrane area was confirmed by the computational fluid dynamics (CFD) simulations for the module.
- A prototype anti-telescoping device (ATD) was fabricated using 3D printing.
- An ⌀8″ spiral-wound (SW) element was fabricated using the scale-up membrane. The element contained 41 membrane leaves, resulting in an area of 35 m^2.
- The ⌀8″ SW element fitted tightly into a stainless-steel housing as the module. The packing density of the SW module provided the basis for the design of the integrated skid.
- The prototype module was tested with a simulated flue gas at OSU, showing CO_2/N_2 separation performance consistent with the flat-sheet membrane.
- The process design has been completed for the integrated testing skid.
- Equipment selection has been completed based on system requirement.
- Piping and instrumentation diagram (P&ID) drawing has been prepared.

Engineering Design of Prototype SW Module

The engineering design of the spiral-wound (SW) membrane module consisting of two parts, (1) a 35-m^2 SW membrane element and (2) a membrane housing, was conducted. The fabrication steps of the multi-leaf membrane element, as illustrated in Figure 21, are described below:

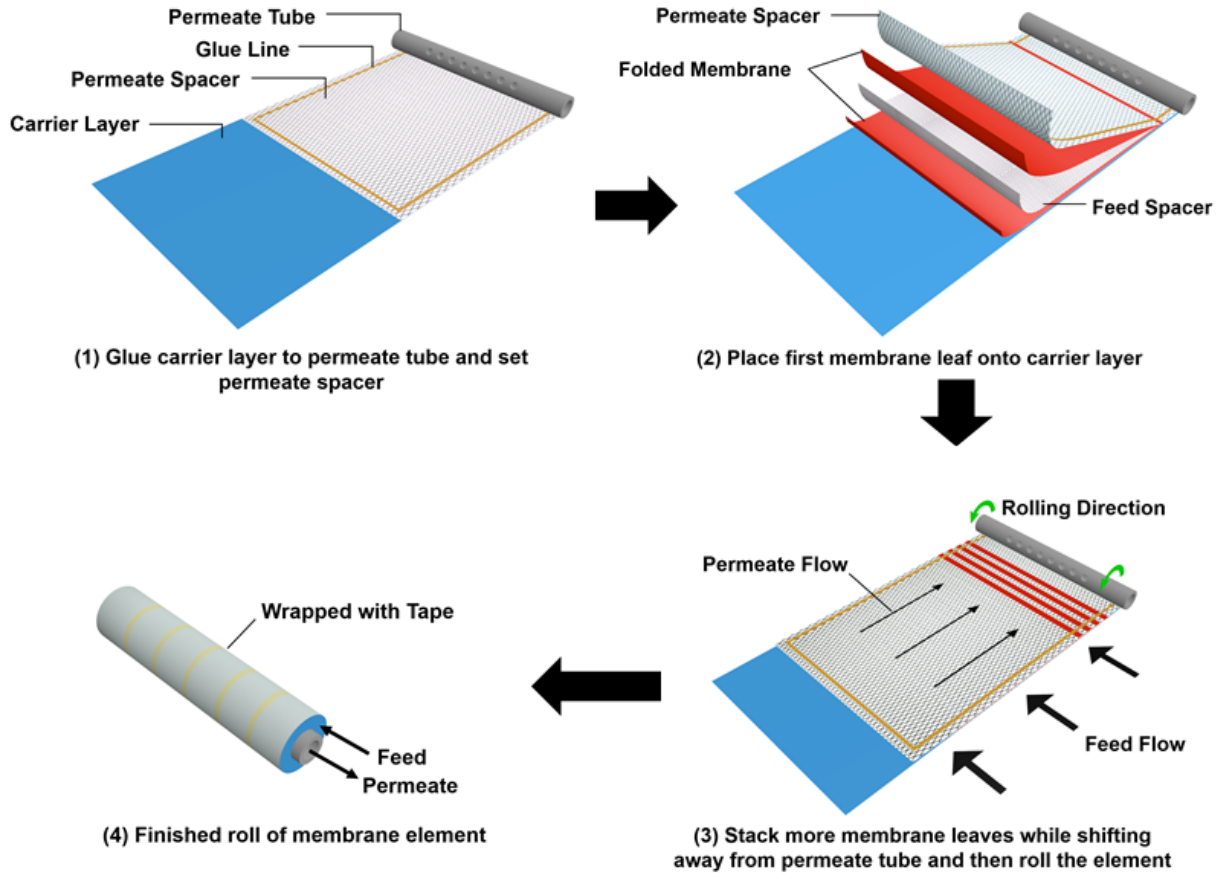

Figure 21. Procedure of multi-leaf SW membrane element fabrication.

(1) The carrier layer is a 20″-wide non-woven fabric sheet to support all the membrane leaves that will be placed on top. A maximum of 41 membrane leaves are used in a single element. The carrier layer is laid out on a platform and attached to a stainless-steel permeate tube (ID 1.0″, OD 1.5″, length 22″), which has one line of permeate holes (diameter: 0.5″) drilled on the side. Since a tension can be applied on the carrier layer during the rolling to achieve a tight roll, the layer needs to be attached to the permeate tube firmly. Hence, the layer is glued to the permeate tube. Next, a permeate spacer is inserted between the carrier layer and the permeate tube, and an epoxy glue line is placed manually using a glue applicator along the three sides of the permeate spacer. The glue line is kept 0.5″ away from the edge to leave enough room for the spreading of the glue.

(2) Next, a piece of membrane of 20″ × 72″ is folded in half, with the selective layer of the membrane facing inward, and a feed spacer is sandwiched in between. Glue is applied along the inner side of the fold to seal any possible damage resulting from the folding, and a permeate spacer

is put above the folded membrane. The folded membrane, with the feed and permeate spacers, is treated as a single membrane leaf.

(3) Subsequently, more membrane leaves are laid on top of the first one with the same pattern of glue lines applied accordingly. After the first leaf, each additional leaf is placed another 0.5″ away from the permeate tube compared to the previous one. The gradual increase in the thickness of the stack makes the rolling process smoother and reduce the relative movement among the leaves. Two sets of straight arrows in Figure 21 (3) illustrate the idealized crossflow pattern during the module's operation: as the feed flows in parallel to the permeate tube, the permeate moves radially towards the tube on the other side of the membrane. After the 41 membrane leaves have been placed, the rolling of the element, in the direction of the curved arrows, is done by an in-house rolling machine. The permeate tube is fixed firmly between a chuck and a tailstock so that it does not slip when the chuck rotates at 2.5 rpm. As the rotation begins, the carrier layer is pulled away from the permeate tube to supply a tension, which is sustained throughout the rolling step. After all the leaves are in the roll, any extra length of the carrier layer is rolled and glued onto the element as a surrogate for the fiber-reinforced plastic (FRP), which keeps the tight packing of the roll. The diameter of the fabricated SW element is designed to be 8″.

(4) Finally, the roll is sat for overnight at room temperature for the glue to set. Trimming is carried out to keep both ends of the element tidy and ensure none of the feed channels is obstructed, resulting in a final membrane element length of 20″. A pair of ATD (1″ thick each) are glued to the two ends of the element. The schematic of the SW membrane element and a photo of the ATD fabricated using 3D printing are shown in Figure 22.

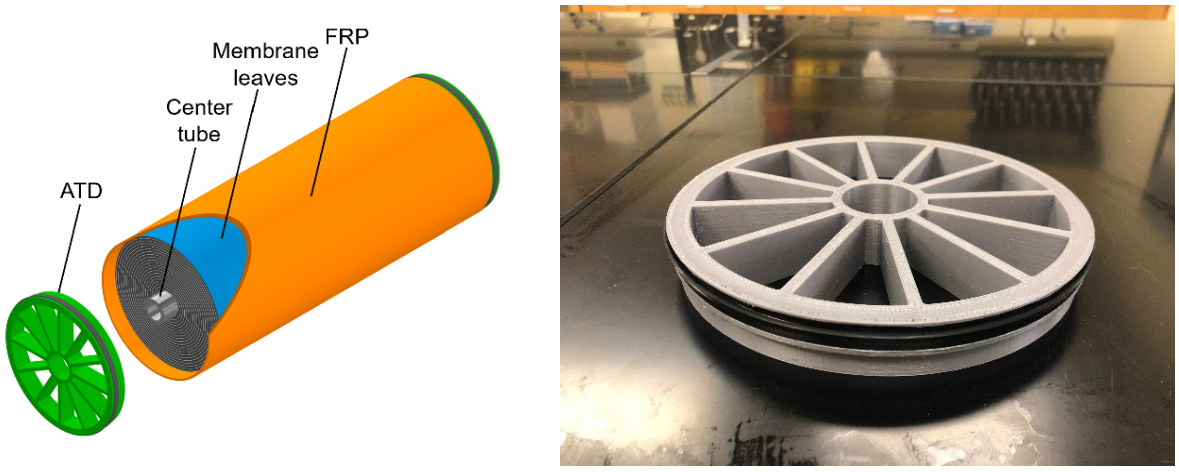

Figure 22. Schematic of prototype SW membrane element (left) and photo of ATD fabricated using 3D printing (right).

As shown in Figure 23, the cylindrical housing consists of a main body and two end caps that direct the feed and permeate streams. The membrane element is fitted tightly into the housing body. Two face-compression O-rings are set in the grooves on each of the end caps to facilitate the sealing. The inner O-ring is pressed against the end surface of the permeate tube to separate the permeate channel from the feed channel. The outer O-ring is positioned in between the flanges of the end cap and the housing body to prevent any leaking of the feed gas into the atmosphere.

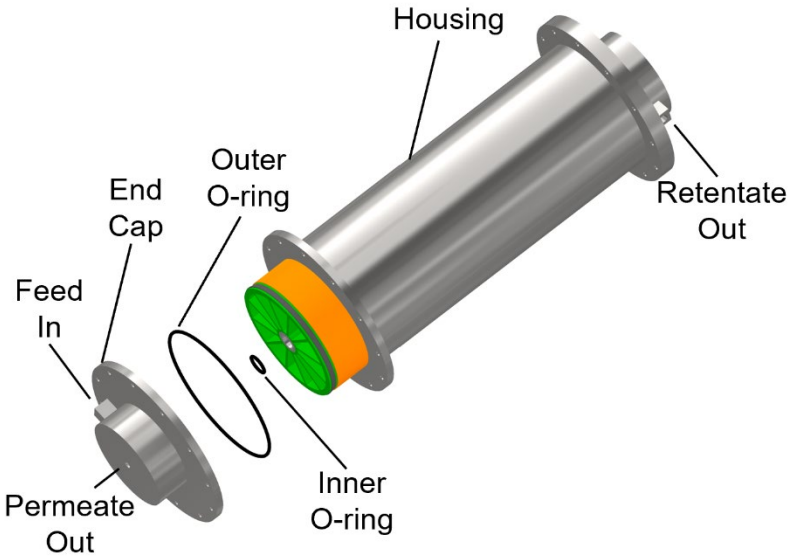

Figure 23. Installation of membrane element into SW module housing.

CFD Simulations of Gas Separation in SW Module

The momentum and mass transfer in the 35-m^2 module has been studied by computational fluid dynamics (CFD) approaches. The gas permeation in the membrane and the convective mass transfer in the feed channel are modeled based on the experimental data collected from the 3-m^2 membrane module [33,34]. Figure 24 shows the contours of the CO_2 flux at the membrane surface of a membrane leaf with sub-optimized and optimized feed spacers. For the sub-optimized spacer, the concentration polarization (gradient) leads to low CO_2 flux for much of the membrane area. With the optimized spacer identified in DE-FE0026919, most of the membrane area is effectively utilized, restricting the low-flux regions to only the edges of the feed channel. Therefore, the spacers used currently are suitable for commercial-scale module fabrication, and no material selection is required.

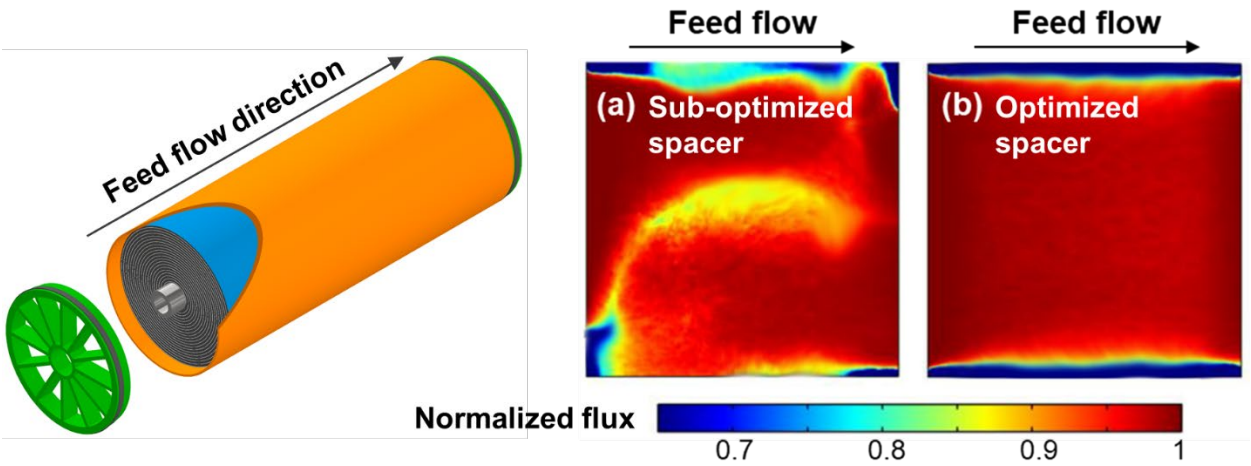

Figure 24. Contours of normalized CO_2 flux with (a) sub-optimized and (b) optimized feed spacers obtained by 3D CFD simulations.

Fabrication of Prototype SW Membrane Module

A prototype SW membrane module was fabricated in order to acquire the following information for the design of the integrated skid:

1) Packing density of the membrane module, which determines the flue gas flow rate that can be treated by the integrated skid.
2) Pressure drop in the membrane module, which determines the sizing of the rotating equipment.
3) The heat capacity of the membrane module, which determines the heating duty for isothermal operation.

In addition, the experience and learning from the module fabrication will also derisk the scope of work in BP2.

As shown in Figure 25 (a), an ⌀8″ SW element was successfully fabricated using the scale-up membrane. The element contained 41 membrane leaves, each with a width of 20″, resulting in a membrane area of 35 m^2. Figure 25 (b) compares the ⌀8″ membrane element vs. the ⌀5″ membrane element that OSU fabricated in DE-FE0026919. The DE-FE0026919 SW element consisted of 7 membrane leaves, each with a width of 12″, and it had a total membrane area of 2.94 m^2. Therefore, a scale-up factor of 11.9 was achieved. Other improvements of the new ⌀8″ SW element included: (1) a thinner fiber-reinforced plastic (FRP) wrapping on the rolled membrane leaves to increase the packing density; (2) two anti-telescoping devices (ATDs) to accommodate for the heavier element. It should be mentioned that the current ⌀8″ membrane element has the same diameter as but half the length of a typical commercial SW element. The element length is limited by the continuous coating machine at OSU, which can only manufacture flat-sheet membranes up to 21″ in width. However, the same rolling protocol can be directly applied to membranes with commercial width. The further scale-up (with a scale-up factor of 2) from the current status to the commercial size should be straightforward. In addition, 3 such membrane elements may be fitted

into a housing to yield a commercial-size membrane module with a membrane area of about 100 m^2.

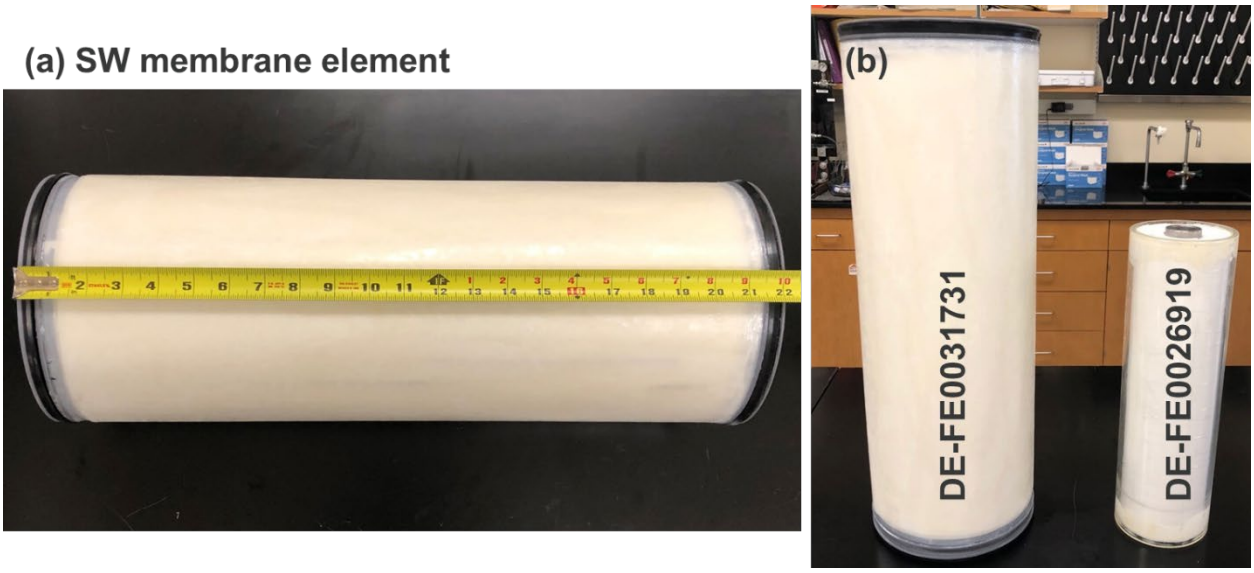

Figure 25. (a) Photo of ⌀8″ prototype SW membrane element; (b) comparison of the ⌀8″ membrane element in this project (DE-FE0031731) vs. the ⌀5″ membrane element in DE-FE0026919.

The SW membrane element was eventually loaded in the stainless-steel housing to become the stainless-steel membrane module as shown in Figure 26 (a). The gaskets on the ATDs successfully stopped the bypass of feed gas and hence enhancing the CO_2 transport in the element. Figure 26 (b) and (c) show the end and side views of the SW element fitted tightly into the housing.

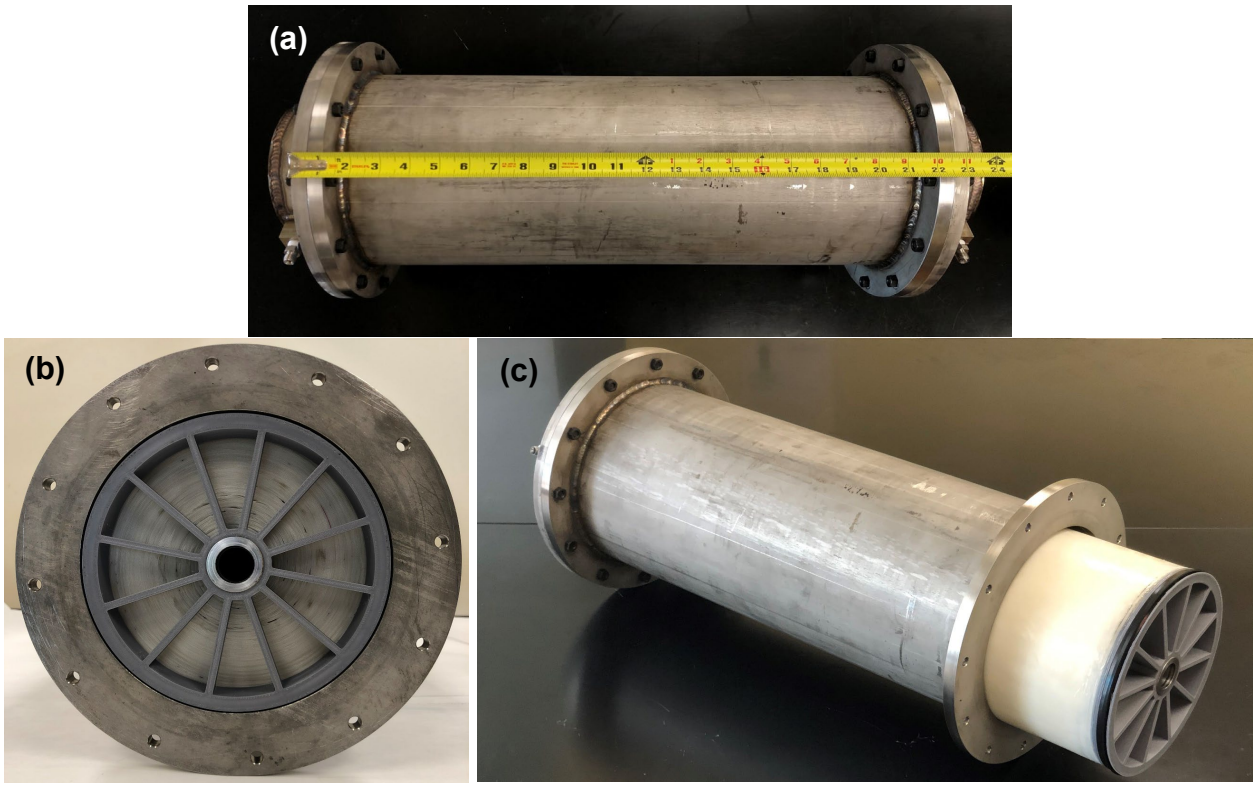

Figure 26. Photos of (a) prototype SW membrane module, and (b) end view and (c) side view of the element fitted in the housing.

Preliminary Test of Prototype SW Membrane Module

The prototype SW membrane module was tested with a simulated flue gas containing 3 ppm SO_2 and 7% O_2 at 77°C with a feed pressure of 4 atm and a permeate vacuum of 0.8 atm. As shown in Figure 27, the module initially showed a low CO_2 permeance of 2825 GPU and a CO_2/N_2 selectivity of 119. This was presumably due to the insufficient feed flow rate, thereby the concentration polarization on the feed side [34]. As the feed flow rate increased, both the CO_2 permeance and selectivity increased, eventually reaching up to 3502 GPU and 159 selectivity. These results were consistent with the performance of the flat-sheet membrane. Thus, the fabrication of the first prototype SW membrane module was successful.

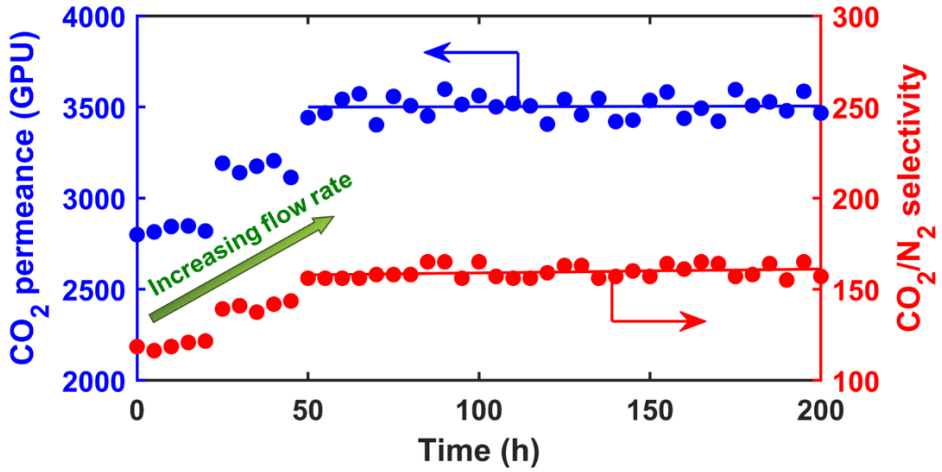

Figure 27. CO_2 permeance and CO_2/N_2 selectivity of prototype SW module at 77°C.

P&ID and Equipment Selection

The P&ID for the two-stage membrane skid has been completed and is shown in Figure 28. The flue gas coming out of the flue gas desulfurization (FGD) unit is delivered to the testing skid and the SO_2 is removed down to 1–3 ppm by a SO_2 polisher containing dilute NaOH solution. The flue gas is then compressed to 3.5 atm and cooled to 77°C. This pressurized stream is passed to the first membrane stage as feed. This step separates the feed gas into a CO_2-depleted retentate stream, usually containing ca. 1% CO_2 and ca. 92% N_2, and a CO_2-enriched permeate stream, usually ~30% CO_2 on wet basis. The retentate is expanded by a back pressure regulator and 15% of it is recycled to the permeate side of the first membrane stage as sweep gas. The remaining retentate, which has had 90% of the CO_2 from the flue gas removed, is discharged. The permeate stream is cooled to knock out the excessive water vapor, and the CO_2 concentration can reach ca. 43 vol.%. This stream is then pressurized to 3.5 atm and passes as feed to the second membrane stage. CO_2 permeates preferentially via the membrane, and >95% CO_2 purity, on dry basis, is achieved in the permeate. The permeate stream goes through an after-cooler and a water knockout, and then is discharged by a vacuum pump. The retentate stream of the second membrane stage, containing ~14% CO_2 on wet basis, is recycled to the feed of the first membrane stage.

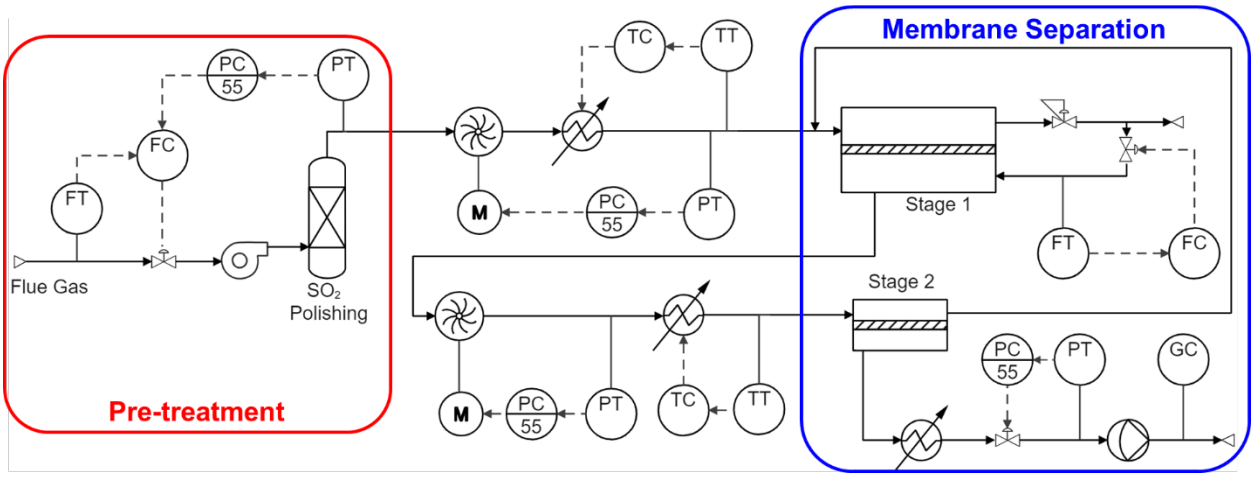

Figure 28. P&ID drawing of the integrated testing skid containing two membrane stages for 90% CO_2 recovery and >95% CO_2 purity. FT = flow transducer; FC = flow controller; PT = pressure transducer; PC = pressure controller; TT = temperature transducer; TC = temperature controller; M = motor; GC = gas chromatography.

The major equipment associated with the 2-stage membrane process is listed in Table 4. All the rotating equipment and heat exchangers are on-shelf products. The membrane module design and fabrication have been described earlier. Another piece of equipment that has been fabricated by OSU is the SO_2 polisher. Preliminary calculations for the design of the SO_2 polisher were conducted for a packed column to achieve a SO_2 concentration of <1 ppm. Reaction kinetics and mass transfer data were obtained from the literature [35-37]. Initial calculations were performed for a flue gas containing 50 ppm SO_2, and the packed column being charged with 5 wt.% NaOH aqueous solution. The calculations indicated that the required residence time was relatively short. Consequently, a batch operation is preferrable. In addition, 316L stainless steel was selected as the vessel material due to its chemical resistance to the caustic NaOH solution [38].

Table 4. Major equipment items of the integrated test skid.

Type	Description	Source†	MOC‡

Rotating equipment	Feed compressor for Stage One, diaphragm	On-shelf	SS
	Feed compressor for Stage Two, diaphragm	On-shelf	SS
	Back pressure regulator for Stage One	On-shelf	CS
	Vacuum pump, diaphragm	On-shelf	SS
	Flue gas delivery blower	On-shelf	SS
Membrane	Membrane Stage One, countercurrent	By OSU	–
	Membrane Stage Two, crossflow	By OSU	–
Heat exchanger	Stage One feed cooler, shell-and-tube	On-shelf	SS
	Stage Two feed cooler, shell-and-tube	On-shelf	SS
	Stage Two vacuum pre-cooler, shell-and-tube	On-shelf	SS
Vessel	Knockout vessel for Stage Two vacuum side	On-shelf	SS
	SO_2 polisher	By OSU	SS

† Source = On-shelf product or fabricated by OSU

‡ MOC = Material of construction. SS = Stainless steel; CS = carbon steel

3.7 Task 7 – NCCC Site Preparation

Summary

- Skid size, water and gas balances, and power requirement have been determined based on the skid design and previous field test experiences at NCCC.

3.8 Task 8 – Construction of the Bench Skid

Summary

- The piping and instrumentation diagram (P&ID) drawing has been revised based on the comments received from NCCC.
- The flue gas humidifier and pressure controller have been fabricated for both Stage 1 and Stage 2 membrane modules.
- The flue gas humidifier and pressure controller have been tested.
- The integration of the membrane modules to the humidifiers and pressure buffer tanks were completed.
- Preliminary leak test was conducted and the temperature, pressure, and flow rate controls were tested.

Updated P&ID and Equipment Selection

The P&ID for the two-stage membrane skid was revised based on the comments received from NCCC. In order to better understand the research efforts for the skid construction and commissioning, the revised P&ID is shown in Figure 29, and the associated stream table is listed in Table 1.1. A flue gas slipstream enters a SO_2 scrubber provided by NCCC that contains NaOH aqueous solution in order to polish the SO_2 down to 1 ppm. The pretreated flue gas (①) is compressed to 371.65 kPa by *Blower 1*. This stream (②) is mixed with the retentate of *Membrane Module 2* (⑰), which (③) enters the *Pressure Buffer Tank* for pressure adjustment to 364.8 kPa

(④). Compared with the designed feed pressure of 354.6 kPa, the 10 kPa pressure head is to account for the pressure drop in *Membrane Module 1*. This stream then enters *Humidifier 1*, which ensures the flue gas is fully saturated with water vapor at 77°C (⑤). The pressurized flue gas (Stream 4) is finally conditioned by *Heater 1* in case of any heat loss and enters the *Membrane Module 1* as feed (⑥). On the retentate side of this membrane module (⑦), a first mass flow controller recycles a portion of the pressurized retentate as an internal sweep (⑨) and reduces its pressure to ca. 1 atm. The remaining retentate is released by a second mass flow controller (⑧), which ultimately controls the overall flue gas flow rate. The permeate of this membrane module (⑩) contains some moisture from the water permeation. The water content is in excess for *Membrane Module 2*. Therefore, a portion of the moisture is knocked out by a *Cooler* (Stream 10) and *Knock Out 1* (⑪). It should be noted that the cooling duty is quite low due to the relatively lower permeate flow rate. Practically, the *Cooler* is replaced by a section of spooled and coiled tubing with air cooling.

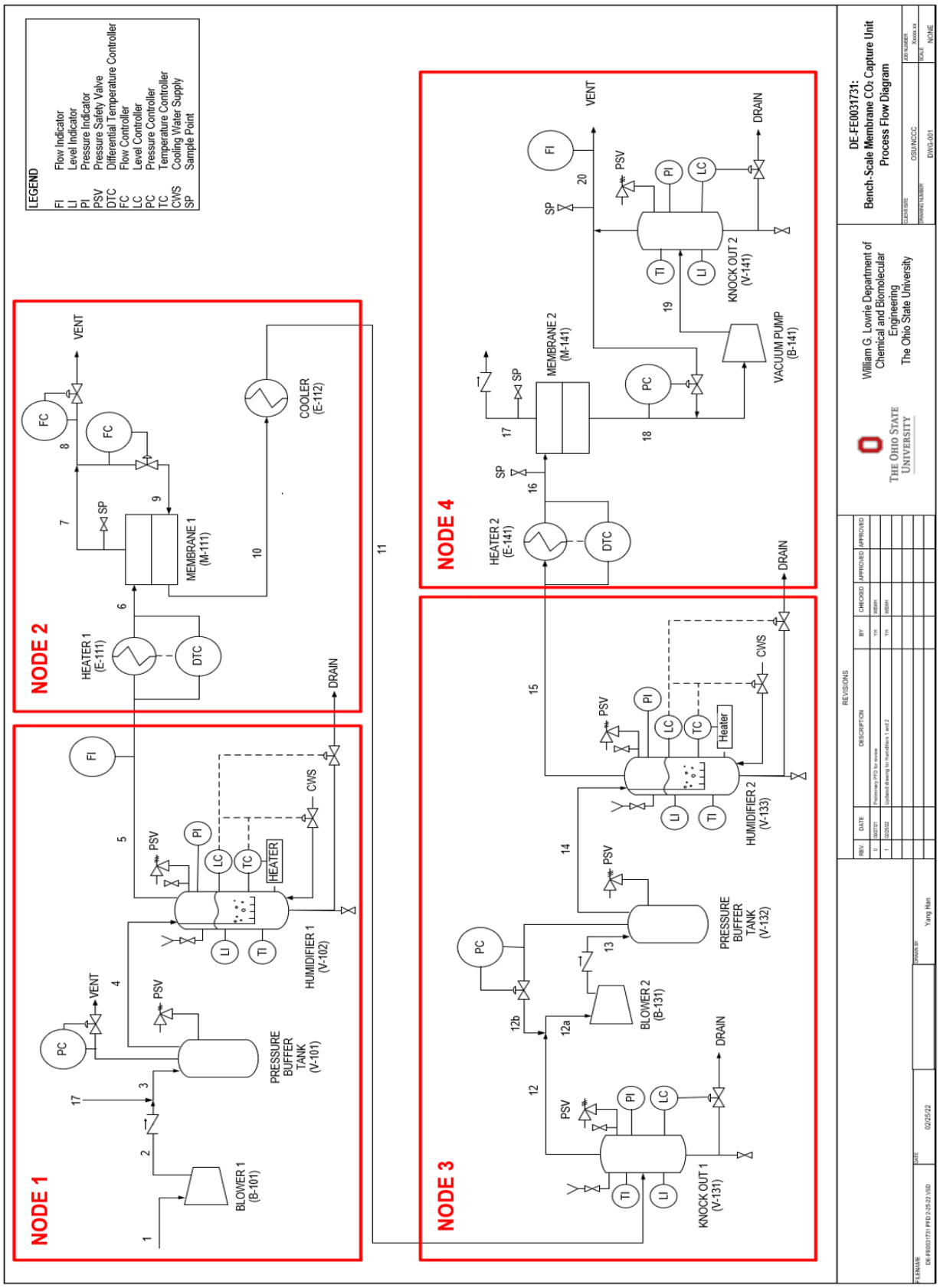

Figure 29. Revised P&ID drawing of the integrated testing skid.

Table 5. Stream table associated with the P&ID drawing.

Stream	1	2	3	4	5	6	7	8	9	10
Vapor Fraction	1.00	1.00	1.00	1.00	1.00	1.00	1.00	1.00	1.00	1.00
***T* [°C]**	57.0	132.3	121.3	121.3	77.0	77.00	77.0	77.0	77.0	77.0
***P* [kPa]**	102.0	371.7	370.3	364.8	364.8	364.8	364.8	364.8	102.0	102.0
Mole Flow [kmol/h]	0.15	0.15	0.18	0.18	0.18	0.18	0.14	0.12	0.02	0.06
Mass Flow [kg/h]	4.36	4.26	5.33	5.33	5.33	5.33	3.96	3.37	0.59	1.96
Volume Flow [m^3/h]	4.08	1.32	1.61	1.61	1.45	1.45	1.14	0.97	0.60	1.73
Mole Fraction										
Ar	0.0081	0.0084	0.0080	0.0080	0.0080	0.0080	0.0101	0.0101	0.0103	0.0038
CO_2	0.1246	0.1294	0.1305	0.1305	0.1306	0.1306	0.0156	0.0155	0.0159	0.3610
H_2O	0.1497	0.1169	0.1133	0.1133	0.1131	0.1131	0.0820	0.0852	0.0630	0.1689
N_2	0.6812	0.7074	0.7126	0.7126	0.7128	0.7128	0.8467	0.8437	0.8642	0.4505
O_2	0.0364	0.0378	0.0355	0.0355	0.0355	0.0355	0.0456	0.0454	0.0465	0.0157

Stream	11	12	13	14	15	16	17	18	19	20
Vapor Fraction	0.95	1.00	1.00	1.00	1.00	1.00	1.00	1.00	1.00	1.00
***T* [°C]**	50.0	50.0	133.9	133.9	77.0	77.0	77.00	77.0	96.0	50.0
***P* [kPa]**	100.3	100.3	364.8	364.8	364.8	364.8	364.8	80.1	112.0	112.0
Mole Flow [kmol/h]	0.06	0.06	0.06	0.06	0.06	0.06	0.04	0.02	0.02	0.02
Mass Flow [kg/h]	1.96	1.90	1.89	1.89	1.89	1.89	1.07	0.8	0.8	0.81
Volume Flow [m^3/h]	1.54	1.54	0.51	0.51	0.44	0.44	0.29	0.8	0.6	0.53
Mole Fraction										
Ar	0.0038	0.0040	0.0041	0.0041	0.0041	0.0041	0.0064	0.0000	0.0000	0.0000
CO_2	0.3610	0.3813	0.3830	0.3830	0.3845	0.3845	0.1351	0.8209	0.8209	0.8421
H_2O	0.1689	0.1222	0.1184	0.1184	0.1148	0.1148	0.0986	0.1432	0.1432	0.1210
N_2	0.4505	0.4758	0.4779	0.4779	0.4798	0.4798	0.7335	0.0359	0.0359	0.0369
O_2	0.0157	0.0166	0.0167	0.0167	0.0168	0.0168	0.0264	0.0000	0.0000	0.0000

The water condensate in Stream 11 is removed by *Knock Out 1*, and the off gas (⑫) is then re-pressurized by *Blower 2* to 364.8 kPa (⑬), which is controlled by the recirculation loop on the *Pressure Buffer Tank* (⑭). This stream is cooled to 77°C and humidified by *Humidifier 2* (⑮). This stream is re-heated by *Heater 2* in case of any heat loss (⑯) and is fed to *Membrane Module 2*. The pressurized retentate (⑰) is released by a mass flow controller, which ultimately controls the feed flow rate. This stream is ultimately recycled to the feed of *Membrane Module 1*. The permeate (⑱) is withdrawn by *Vacuum Pump 1* at 81 kPa. The discharge of the *Vacuum Pump 1* (⑲) is dehumidified by *Knock Out 2* and then released (⑳). Overall, the flow rates and pressures of the gaseous streams are all controlled mechanically. The only programmable logic control

needed is for the solenoid valves for *Humidifiers 1 and 2*, which control the make-up water and drainage flow rates.

The bill of materials associated with the 2-stage membrane process is listed in Table 6. The membrane modules are not listed in this table. The housings of *Membrane Module 1* and *Membrane Module 2* and the Stage 1 humidifier and buffer tank have been fabricated. The remaining fabrication work mainly involves the Stage 2 humidifier and buffer tank.

Table 6. Bill of materials for the integrated test skid.

ITEM CATEGORY / DESCRIPTION	TYPE OF EQUIPMENT	SIZE OR RATING	M.O.C.‡
VESSELS			
Humidifier 1	Vertical cylinder vessel, with sparger	4 inches diameter by 28 inches height, 50 psig MAWP	304 or 316 SS
Humidifier 2	Vertical cylinder vessel, with sparger	4 inches diameter by 28 inches height, 50 psig MAWP	304 or 316 SS
Knock Out 1	Vertical cylinder vessel	4 inches diameter by 28 inches height, Full Vacuum MAWP	304 or 316 SS
Knock Out 2	Vertical cylinder vessel	4 inches diameter by 28 inches height, 50 psig MAWP	304 or 316 SS
COMPRESSORS			
Compressor 1	Non-lubricated rocking piston compressor	Nominal 3–4 scfm (83–112 slpm)	
Compressor 2	Non-lubricated rocking piston compressor	Nominal 1–2 scfm (83–112 slpm)	
VACUUM PUMP			
Vacuum Pump 1	Non-lubricated diaphragm pump	Nominal 1–2 scfm discharge with 24 inHg vacuum	
PRESSURE SAFETY VALVES (PSVs)			
Humidifier 1 PSV	Spring-loaded relief valve	Set at 50 psig, to relieve up to 150 slpm	304 or 316 SS
Knock Out 1 PSV	Spring-loaded relief valve	Set at 50 psig, to relieve up to 150 slpm	304 or 316 SS
Humidifier 2 PSV	Spring-loaded relief valve	Set at 50 psig, to relieve up to 150 slpm	304 or 316 SS
Knock Out 2 PSV	Spring-loaded relief valve	Set at 50 psig, to relieve up to 150 slpm	304 or 316 SS
PRESSURE CONTROLLERS/REGULATORS			
Pressure Control Vent - Humidifier 1	Backpressure Control Valve, mechanical	72 slpm, 0 to 50 psig adjustable	
Pressure Control Vent - Humidifier 2	Backpressure Control Valve, mechanical	20 slpm, 0 to 50 psig adjustable	
Compressor 2 - Suction Pressure Regulator	Single-stage regulator, mechanical	20 slpm, 0 to 50 psig adjustable	
Vacuum Pump 1 - Vacuum Pressure Control	Vacuum Regulator, mechanical	10 slpm, 0.2 to 1 atma adjustable	
HEATERS/COOLERS			
Sparger 1 Heater	Band heater or heat tape with temperature controller	150 Watts (expected duty is 108.43 W, 370 Btu/h) duty	
Sparger 2 Heater	Band heater or heat tape with temperature controller	25 Watts (expected duty is 3.84 W, 13.1 Btu/h) duty	
Heater 1	Heat tape with temperature controller	25 Watts (expected duty is 3.2 W, 11 Btu/h) duty	
Heater 2	Heat tape with temperature controller	25 Watts (expected duty is 0.26 W, 0.85 Btu/h) duty	
Membrane 1 Permeate Cooler	Simple length of uninsulated coiled tubing	25 Watts or less (87 Btu/h) duty	

FLOW CONTROLLERS			
Membrane 1 Retentate Mass Flow Controller	Mass flow controller - with flow output signal to data logger	50 psig, 0 to 150 slpm adjustable	
Membrane 1 Sweep Mass Flow Controller	Mass flow controller - with flow output signal to data logger	50 psig, 0 to 50 slpm adjustable	
Membrane 2 Retentate Mass Flow Controller	Mass flow controller - with flow output signal to data logger	20 psig, 0 to 150 slpm adjustable	
FLOW TRANSMITTERS			
Membrane 1 Feed Flow Transmitter	Mass flow meter - with flow output signal to data logger	50 psig, 0 to 150 slpm	
Membrane 2 Feed Flow Transmitter	Mass flow meter - with flow output signal to data logger	50 psig, 0 to 50 slpm	
Membrane 2 Permeate Flow Transmitter	Mass flow meter - with flow output signal to data logger	50 psig, 0 to 50 slpm	
PRESSURE INDICATORS			
Humidifier 1	Bourdon Tube Pressure Gauge	0–50 psig	304 or 316 SS
Knock Out 1	Bourdon Tube Pressure Gauge	0–50 psig	304 or 316 SS
Humidifier 2	Bourdon Tube Pressure Gauge	0–50 psig	304 or 316 SS
Membrane 2 Permeate Line	Bourdon Tube Vacuum Gauge	30 inHg Vacuum to 15 psig	304 or 316 SS
Knock Out 2	Bourdon Tube Pressure Gauge	0–50 psig	304 or 316 SS
TEMPERATURE INDICATORS			
Humidifier 1	Simple dial type thermometer, threaded	0–100°C	304 or 316 SS
Knock Out 1	Simple dial type thermometer, threaded	0–100°C	304 or 316 SS
Humidifier 2	Simple dial type thermometer, threaded	0–100°C	304 or 316 SS
Knock Out 2	Simple dial type thermometer, threaded	0–100°C	304 or 316 SS
SOLENOID CONTROL VALVES			
Humidifier 1 CWS	On/off type solenoid valve, N.C.§	ca. 2 L/min	
Humidifier 1 Drain	On/off type solenoid valve, N.O.§	ca. 2 L/min	
Humidifier 2 CWS	On/off type solenoid valve, N.C.	ca. 2 L/min	
Humidifier 2 Drain	On/off type solenoid valve, N.O.	ca. 2 L/min	

† Maximum allowable working pressure (MAWP).
‡ Material of construction (M.O.C.).
§ Normally close (N.C.); normally open (N.O.)

Fabrication of Humidifier and Pressure Buffer Tank

The fabrication of the humidifier and pressure buffer tank assembly is described in this section. As shown in Figure 30 (a), a double ended sample cylinder was chosen to fabricate the humidifier. The length of the cylinder was 26.7″, with a diameter of 4″ and a wall thickness of 0.28″. The total volume of the cylinder was 1 gallon, and the connection size was ½″. In order to convert this cylinder into a humidifier, it was modified to accommodate 5 ports required for different components, including the gas inlet, water inlet, gas outlet, thermocouple, and heating element. The lengths of the heating element and the thermocouple were 6″ and 24″, respectively. As per our design, the heating element was inserted from the opening at the bottom, and the thermocouple was inserted from the top of the humidifying cylinder. Both components were in direct contact with water. In order to operate under different conditions, the outer layer of the selected elements

consisted of 316 stainless steel. In order to control the temperature, a proportional–integral–derivative (PID) controller was chosen. A continuous water supply into the humidifier was maintained using a HPLC pump. Finally, the outlet gas of the humidifier passed through a coalescing filter in order to remove any condensed water droplets. In order to minimize the heat loss, a heating tape was wrapped all over the humidifier including the tube, joints, and the coalescing filter, and it was covered by an insulating tape.

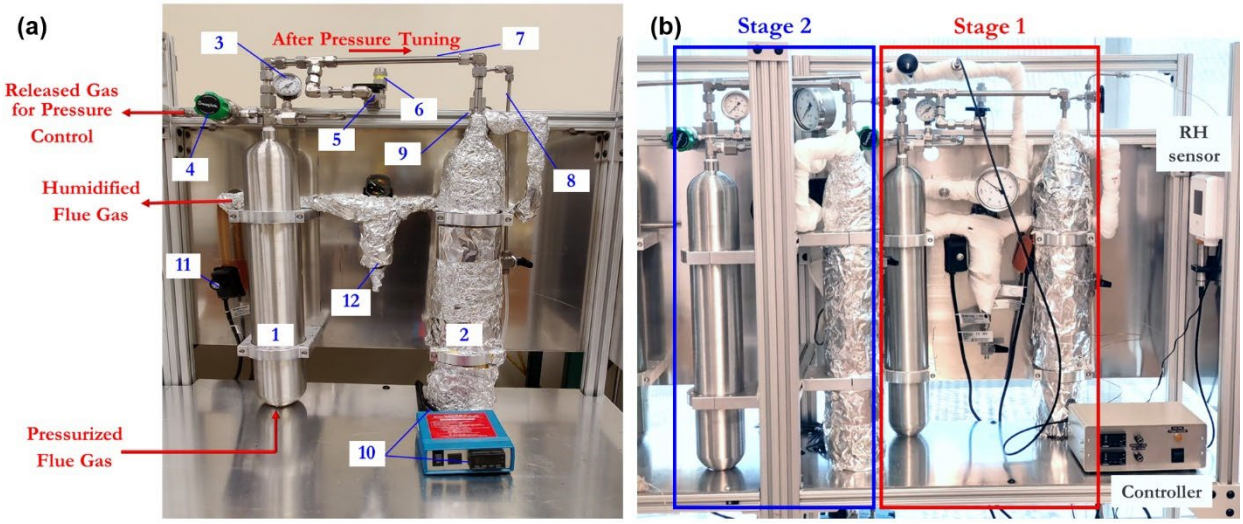

Figure 30. (a) Detailed setup of the humidifier and pressure buffer tank assembly. (b) Photos of the Stage 1 and Stage 2 humidifier assemblies. 1 – Pressure buffer tank; 2 – humidifier; 3 – pressure indicator; 4 – back pressure regulator; 5 – quick release valve; 6 – pressure safety valve; 7 – gas inlet to humidifier; 8 – water inlet; 9 – thermocouple; 10 – heating element; 11 – heating tape controller; 12 – coalescing filter.

As discussed in Figure 29, a pressure buffer tank was also connected in tandem with the humidifier in order to control the pressure. The location and design of this pressure buffer tank is also shown in Figure 30 (a). As seen, the pressure buffer tank consisted of a double ended sample cylinder that was identical to the humidifier, a pressure gauge, a back pressure regulator, a quick release valve, and a pressure safety valve. By using the back pressure regulator, the required pressure was maintained. On the other hand, the pressure safety valve could quick depressurize the gas from the system in case of a sudden pressure overshoot.

As shown in Figure 30 (b), this humidifier assembly was duplicated for both Stage 1 and Stage 2. The initial testing of the humidifier assembly was conducted on the Stage 1 humidifier by varying the gas flow rate at an absolute pressure of 4 atm. The temperature of the system was set at 80°C. The tested gas flow rates were 10, 20, 30, and 40 slpm, respectively. The observed temperatures at different gas flow rates are presented in Table 1.3. The results indicated that we had reasonably good temperature control over the fabricated humidifier. The testing was also carried out for the Stage 2 humidifier at 4 bar absolute pressure and a gas flow rate of 40 slpm. The system temperature was maintained at a set point of 82°C to achieve the desired gas temperature of 77°C because of the heat loss. The gas outlet temperature was found as 78°C and

the relative humidity (RH) was 99.5%. However, the gas outlet temperature of Stage 1 was 77.1 °C under similar conditions. This indicates that there is a further scope to improve the insulation of Stage 1 humidifier. Furthermore, the temperature optimization of Stage 2 humidifier was conducted, and the results are presented in Table 1.3. It was found that a set temperature of 81°C of the system was sufficient to achieve the desired temperature of ~77 °C.

Table 7. Relative humidities and gas outlet temperatures of humidifiers.

Humidifier	Gas flow rate (slpm)	Absolute pressure (bar)	Set temp. (°C)	Gas outlet temp. (°C)	Relative humidity (%)
Stage 1	10	4	80.0	80.0	–
Stage 1	20	4	80.0	80.0	–
Stage 1	30	4	80.0	79.8	–
Stage 1	40	4	80.0	77.1	–
Stage 2	40	4	82.0	78.0	99.5
Stage 2	40	4	81.0	77.2	99.2
Stage 2	40	4	80.0	76.5	99.6

Skid Integration

The major pieces of process equipment have been integrated with a general layout as shown in Figure 31. The upper part of the skid on the left-hand side (Figure 31 (a)) contains the SO_2 polishers (red) along with a pressure buffer tank (white) of the Stage 1 humidifier. The module for Stage 1 is placed on the lower shelf of the stand along with two coils (not included in the figure), which are required to cool down the humidified gas exiting the Stage 1. On the other hand, the upper part of the right-hand side humidifier contains the Stage 1 humidifier (white) along with the buffer tank and the Stage 2 humidifier (yellow). The bottom part of the skid contains the Stage 2 module and two HPLC pumps in order to provide the makeup water. The Stage 2 module is connected in perpendicular to the Stage 1 module. Apart from these components, two temperature controllers (not shown in this figure) are placed in the space available in front of the SO_2 polishers. The peristaltic pump required to fill the humidifiers initially is placed in front of the Stage 2 humidifiers. The Stage 1 and Stage 2 blowers as well as the vacuum pump are mounted onto a separate stand, which is placed on the back side of the skid (Figure 31 (b)). A photo of the integrated skid is shown in Figure 32.

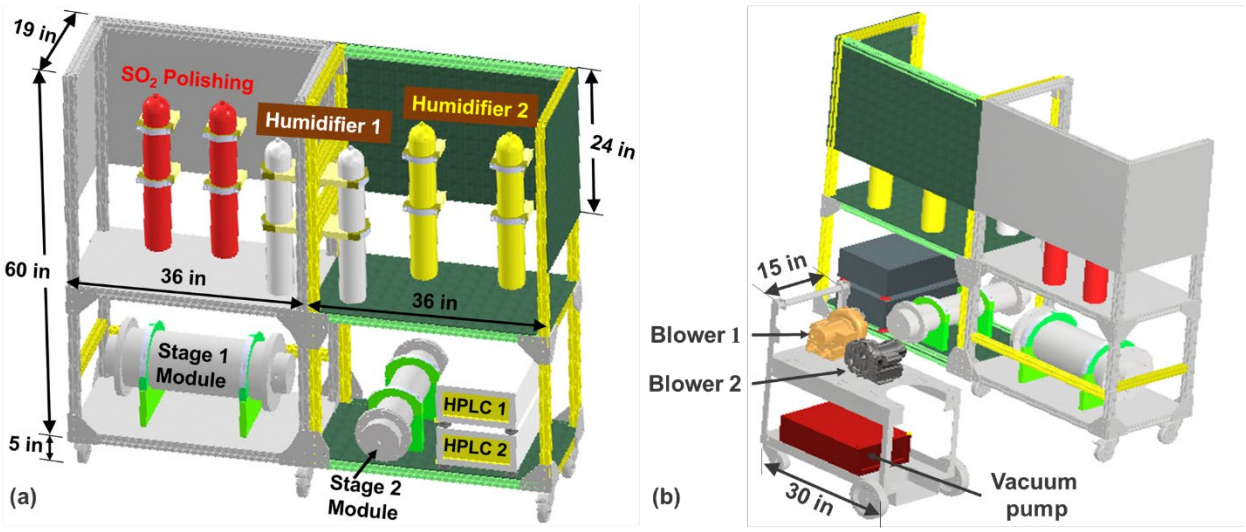

Figure 31. General layout of integrated bench skid: (a) front side and (b) back side.

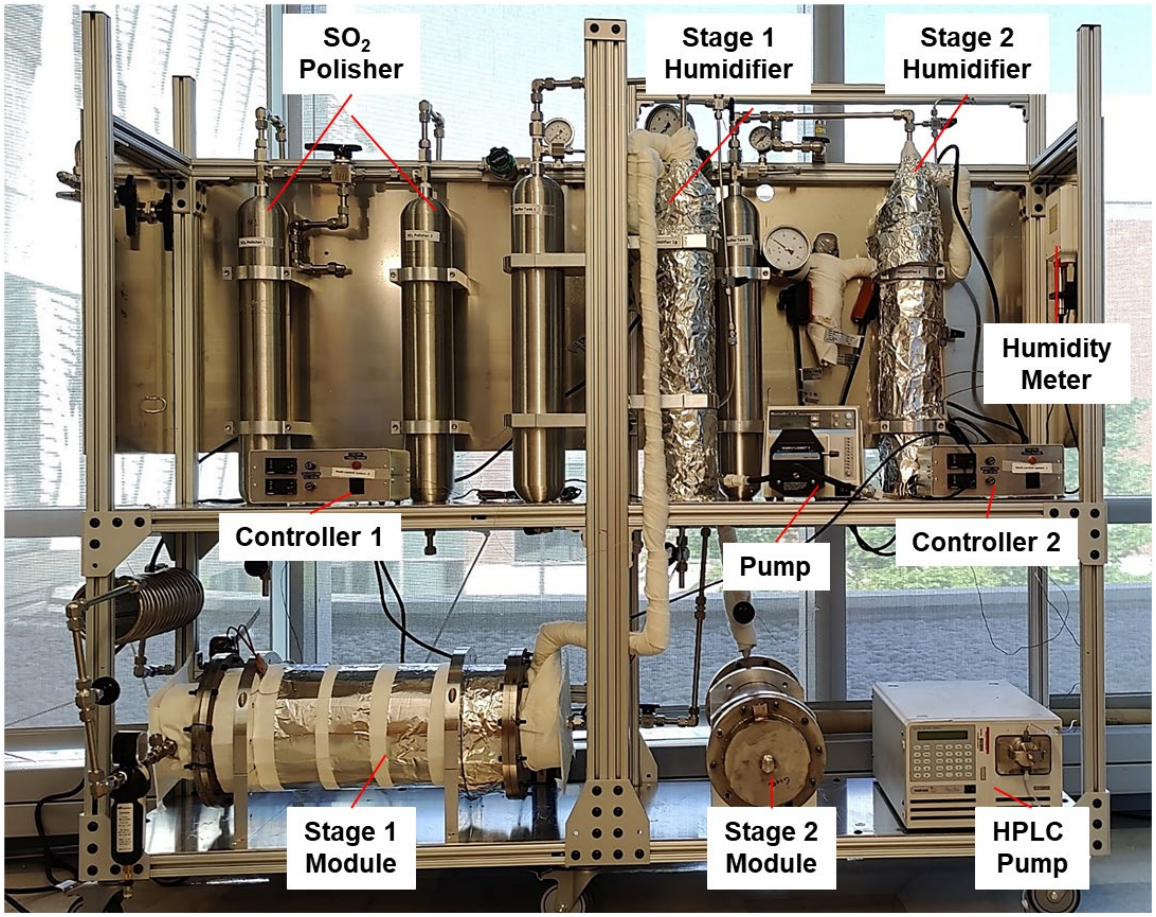

Figure 32. Photo of the integrated bench skid.

The preliminary leak check of the integrated bench skid was performed, and all fabricated parts were proven to be gas tight. The accuracies of the temperature, pressure, and flow rate controls were further tested at 4-bar absolute feed pressure and at a gas flow rate of 40 slpm. The gas outlet temperature was found as 77.1°C. The set temperature for the immersion heater and heating tape was kept higher than 77°C due to some heat loss, primarily from the clamp that was in direct contact with the cylinder. Furthermore, the relative humidity and the temperature of the gas outlet were observed at different gas flow rates. A relative humidity (RH) of 99.3 % was measured, and the results suggested that the humidifiers were operating well as per the skid design specifications. Both the humidifiers were run continuously for 72 h, and no condensation was observed during the entire period. It securely maintained a temperature of 77±1°C and a RH of 99± 2%. The little variation in the RH might be owing to the sensitivity of the humidity sensors. The temperature and humidity sensitivities of the sensors were ±0.2 °C and ±1.5 %, respectively.

3.9 Task 9 – Further Optimized Membrane Synthesis

Summary

- A new PES support was synthesized with a high surface porosity of 30.4%, ca. 5% higher than the previous best support.
- The reaction pathways of CO_2 and fixed-site carrier, pEtC1, were further studied by density functional theory (DFT).
- The reaction pathways of CO_2 and fixed-site carrier, pEtC2, were further studied by DFT.
- The synthesis of pEtC2, a homopolymer with each repeating unit containing a more efficient C2 reactive group, was conducted, and the resultant polymer possessed a high MW of 30 MDa.

Polymer Support Synthesis Using New Casting Solution

Continued research efforts were pursued to further improve the polymer support characteristics including the surface porosity and CO_2 permeance of the polymer support. A PES support with a bi-continuous structure was fabricated via a vapor-induced phase separation (VIPS) method [13,39], where a nonsolvent vapor was used to bring a homogeneous polymer casting solution into phase separation and to form a porous membrane. Particularly, the relative humidity during the vapor exposure step was increased to induce more pores on the support surface.

Figure 33 shows the surface and cross-section morphologies of the new PES support characterized by scanning electron microscopy (SEM). As shown, the new support exhibited a morphology with bicontinuous structure. The average surface pore size and surface porosity were 36.6 nm and 30.4%, respectively. The surface porosity was ca. 5% higher than the previous best support. The scale-up fabrication of this improved support will be discussed in Task 11.

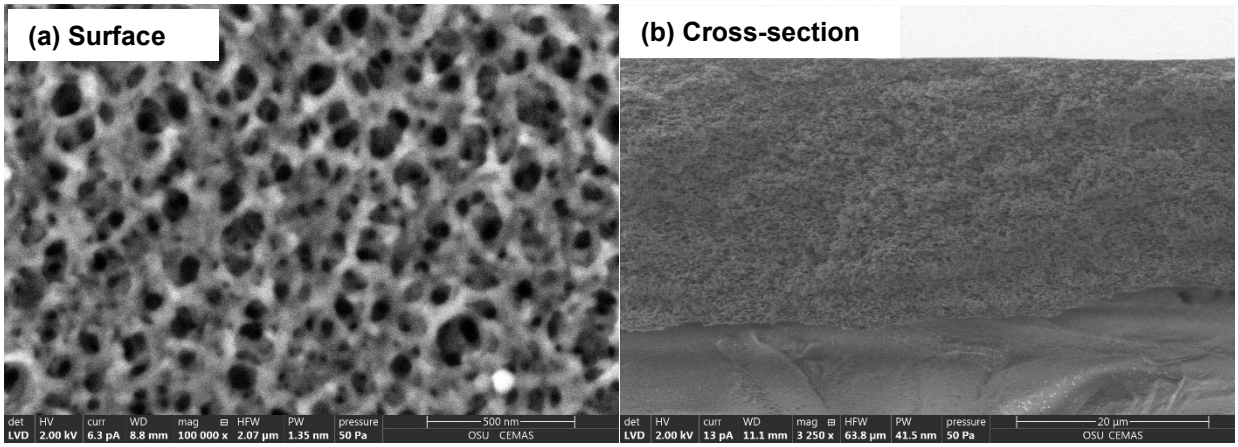

Figure 33. SEM images of pilot-scale PES supports: (a) surface and (b) cross-section.

DFT calculations of Novel Fixed-Site Carriers—pEtC1

Following the procedure reported in our previous study [40], DFT calculations were conducted to study the reaction energy profile of the bicarbonate formation pathway for pEtC1. For simplicity, the reaction of a single pEtC1 repeating unit (i.e., EtC1) was studied. In other words, the chemical reactions between the C1 functional groups and CO_2 molecules were assumed to occur within their immediate chemical surroundings. These calculations focused on the key states along the carrier−CO_2 reaction, i.e., complex, transition state (TS), products, and reactants states. Carrier-CO_2 configurations were optimized for each state, and the one that yielded the lowest relative electronic energy (i.e., $\Delta E_{products} = E_{products} - E_{reactants}$) was identified as the preferred configuration. The preferred configurations of the pEtC1−CO_2 reaction following the bicarbonate formation pathway are depicted in Figure 34.

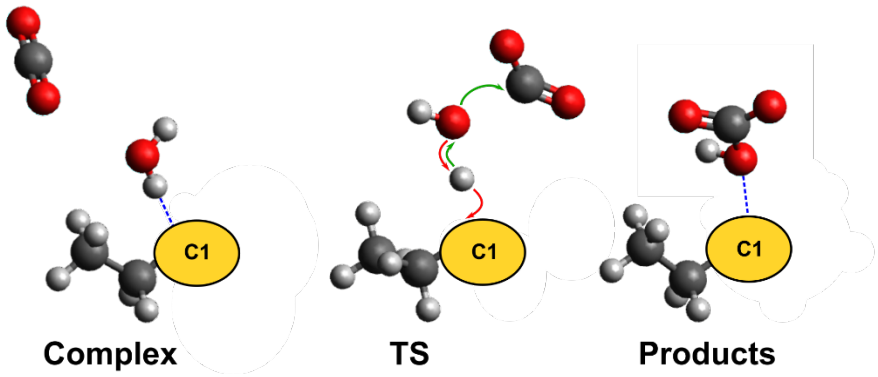

Figure 34. Molecular configurations of (a) complex, (b) TS, and (c) products of the bicarbonate formation pathway for the pEtC1−CO_2 reaction. The atom trajectories following the forward and reverse reaction directions are illustrated using green and red arrows in the TS structure, respectively. Hydrogen bonds are illustrated using blue dashed line. Color codes: carbon = gray, hydrogen = white, and oxygen = red.

In comparison, polyvinylamine (PVAm) and trimethylamine (TMA) were also studied for the reaction energy profiles of their respective bicarbonate formation pathways. PVAm was selected because it is one of the highly studied amine-based fixed-site carriers and possesses the highest amino functional group density [41]. However, the amino groups in PVAm are primary amino groups, and they tend to form carbamate products in the reaction with CO_2, as proven both computationally [40] and experimentally [42]. In comparison, TMA, a tertiary amine that can only react with CO_2 to form a bicarbonate product [43], was also selected as a reference for comparison.

The relative electronic energy profiles of pEtC1, PVAm, and TMA following the bicarbonate formation pathway are summarized in Figure 35. We noted that pEtC1 demonstrated an overall lower energy profile. More importantly, pEtC1 displayed at least 2.6 kcal/mol lower relative electronic energies (i.e., 3.42 kcal/mol) than both PVAm (i.e., 5.80 kcal/mol) and TMA (i.e., 6.02 kcal/mol) at the TS state, indicating a faster reaction kinetics. As mentioned above, PVAm showed a higher energy barrier along the bicarbonate pathway due to its preference to the carbamate formation. As for the tertiary amine, TMA was also predicted to have a higher activation energy than that of pEtC1. This may be attributed to the lower basicity of TMA than that of pEtC1, resulting in a slower protonation step by water.

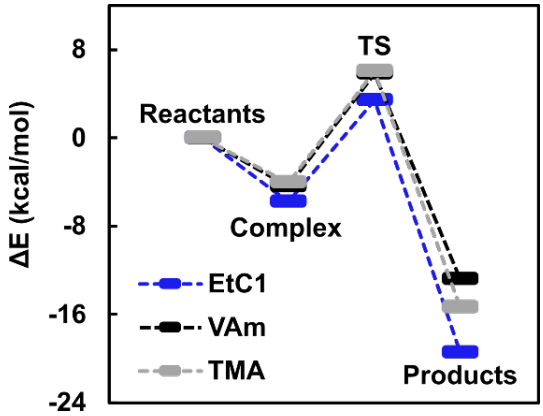

Figure 35. Relative energies (i.e., ΔE, with respect to reactants) of pEtC1, PVAm, and TMA in the reactions with CO_2 following the bicarbonate formation pathway.

Unlike the pendant amino groups of PVAm, the C1 groups of pEtC1 are on the polymer backbone. Therefore, we also investigated if the repeating unit EtC1 is representative for the reaction chemistry of the pEtC1 polymer chain. Specifically, we studied two oligomer structures, i.e., NH_2–EtC1–CH_3 and EtC1–EtC1–EtC1. As shown in Figure 36 (a), both structures showed similar energy profiles as EtC1 by following the bicarbonate formation. Subsequently, we also used the NH_2–EtC1–CH_3 structure to study its reaction with CO_2 following the carbamate formation pathway. As expected, both EtC1 and NH_2–EtC1–CH_3 exhibited extremely high energy barriers for forming a zwitterion with CO_2 (i.e., TS-1 in Figure 36 (b)). Overall, the DFT studies indicate that pEtC1 reacts with CO_2 following the bicarbonate formation pathway, which doubles the CO_2 loading compared with primary and secondary unhindered amines. More importantly, pEtC1 potentially possesses a faster reaction kinetics than tertiary amines and unhindered amines.

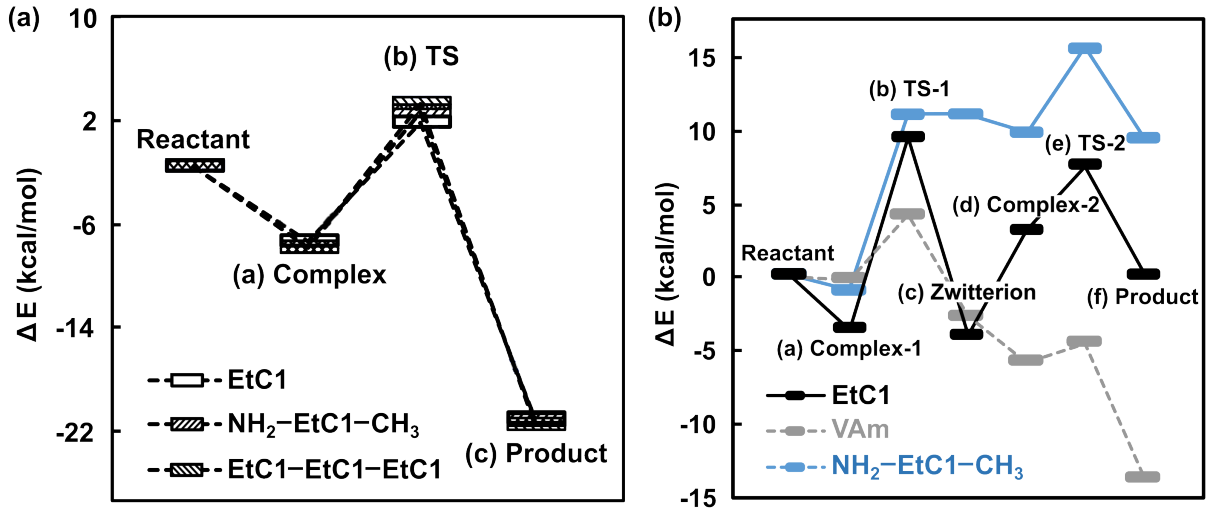

Figure 36. (a) Relative energy profiles of EtC1, NH_2–EtC1–CH_3, and EtC1–EtC1–EtC1 following the bicarbonate pathway. (b) Relative energy profiles of EtC1, PVAm, and NH_2–EtC1–CH_3 following the carbamate pathway.

DFT calculations of Novel Fixed-Site Carriers—pEtC2

Following the procedure reported in our previous study [40], DFT calculations were conducted to study the reaction energy profile of the bicarbonate formation pathway for pEtC2. For simplicity, the reaction of a single pEtC2 repeating unit (i.e., EtC2) was studied. In other words, the chemical reactions between the C2 functional groups and CO_2 molecules were assumed to occur within their immediate chemical surroundings. These calculations focused on the key states along the carrier−CO_2 reaction, i.e., complex, transition state (TS), products, and reactants states. Carrier-CO_2 configurations were optimized for each state, and the one that yielded the lowest relative electronic energy (i.e., $\Delta E_{products} = E_{products} - E_{reactants}$) was identified as the preferred configuration. The preferred configurations of the pEtC2−CO_2 reaction following the bicarbonate formation pathway are depicted in Figure 37. In comparison, polyvinylamine (PVAm) and trimethylamine (TMA) were also studied for the reaction energy profiles of their respective bicarbonate formation pathways. PVAm was selected because it is one of the highly studied amine-based fixed-site carriers and possesses the highest amino functional group density [41]. However, the amino groups in PVAm are unhindered primary amino groups, and they form carbamate products mainly in the reaction with CO_2, as proven both computationally [40] and experimentally [42]. In comparison, TMA, a tertiary amine that can only react with CO_2 to form a bicarbonate product [43], was also selected as a reference for comparison.

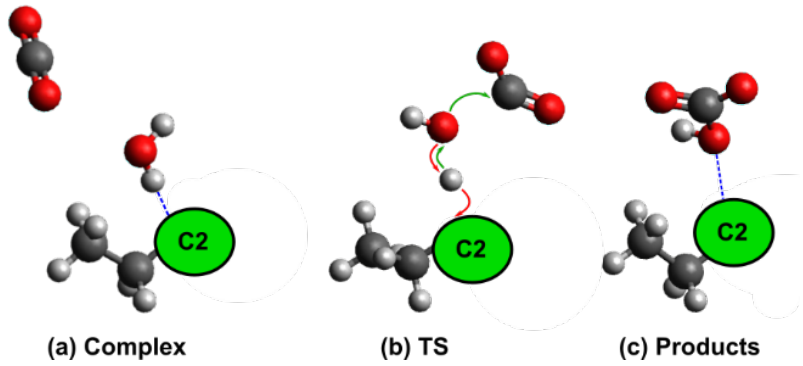

Figure 37. Molecular configurations of (a) complex, (b) TS, and (c) products of the bicarbonate formation pathway for the pEtC2−CO_2 reaction. The atom trajectories following the forward and reverse reaction directions are illustrated using green and red arrows in the TS structure, respectively. Hydrogen bonds are illustrated using blue dashed line. Color codes: carbon = gray, hydrogen = white (or silver color), and oxygen = red.

The relative electronic energy profiles of pEtC2, PVAm, and TMA following the bicarbonate formation pathway are summarized in Figure 38. We noted that pEtC2 demonstrated an overall lower energy profile. More importantly, pEtC2 displayed at least 0.9 kcal/mol lower relative electronic energies (i.e., 4.89 kcal/mol) than both PVAm (i.e., 6.02 kcal/mol) and TMA (i.e., 5.80 kcal/mol) at the TS state, indicating a faster reaction kinetics. As mentioned above, PVAm showed a higher energy barrier along the bicarbonate pathway due to its preference to the carbamate formation. As for the tertiary amine, TMA was also predicted to have a higher activation energy than that of pEtC2. This may be attributed to the very slow protonation of TMA by water, which limits the formation rate of the bicarbonate product.

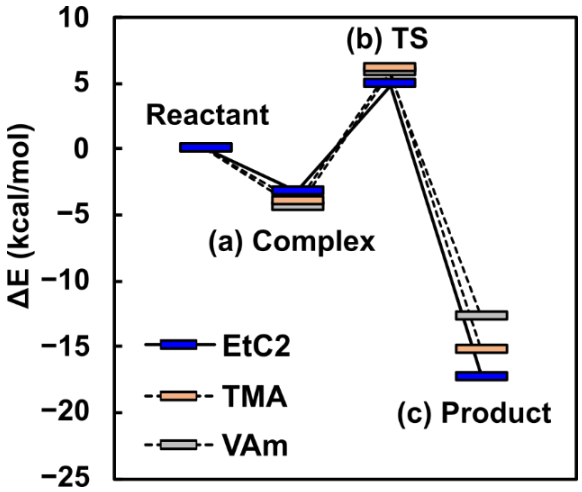

Figure 38. Relative energies (i.e., Δ*E*, with respect to reactants) of pEtC2, PVAm, and TMA in the reactions with CO_2 following the bicarbonate formation pathway.

Synthesis of Novel Fixed-Site Carrier—pEtC1

The synthesis procedure of a homopolymer with reactive sites resembling Carrier 1 (C1) was improved in catalyst amount and temperature profile in order to increase its MW and better serve as fixed-site carrier. The synthesis procedure was separated into two steps. At the first step (pre-polymerization), the polycondensation reaction was operated at 1 atm with N_2 flushing in. At the second step (polymerization), the reaction was operated at 10 torr.

In order to optimize the synthesis conditions for pEtC1, 10 batches of polymers (Samples A–J) were synthesized, and the conditions are summarized in Table 8. Accordingly, the photos of the polymer samples are shown in Figure 39. For Samples A–C, the catalyst amount was decreased step-wisely while maintaining a consistent temperature profile. By decreasing the catalyst amount from 100 mol.% to 75 mol.%, the polymer MW increased from 4.0 to 5.0 MDa. Subsequently, the catalyst amount was decreased to 50 mol.%, and the MW decreased from 5.0 to 4.3 MDa. By adopting the design of experiment approach [44], the catalyst amount was optimized to 62.5 mol% based on the characterization results of Samples A–D. By employing the predicted optimal catalyst amount, we obtained Sample E with a determined MW of 7.7 MDa. For Samples H–J, we focused on the optimization of the temperature profile used for Step 2. The designed experiments for optimizing the temperature profile have not been finished yet. So far, we obtained Sample G with the highest MW of 11.9 MDa.

Table 8. Synthesis conditions for pEtC1.

Sample	Monomer ratio	Catalyst amount (mol.%)	Step 1/2 Temperatures (°C)	Step1/2 Reaction time	Molecular weight (MDa)
A	Moderate	100	110/180	Moderate/Low	4.0
B	Moderate	75	110/180	Moderate/Low	5.0
C	Moderate	50	110/180	Moderate/Low	4.3
D	Moderate	72.3	110/180	Moderate/Low	5.3
E	Moderate	62.5	110/180	Moderate/Low	7.7
F	Moderate	62.5	110/180	Low/Low	7.5
G	Moderate	62.5	110/180	Moderate/High	11.9
H	Moderate	62.5	110/240	Moderate/Low	7.1
I	Moderate	62.5	110/200	Moderate/Medium	7.6
J	Moderate	62.5	110/170	Moderate/High	11.8

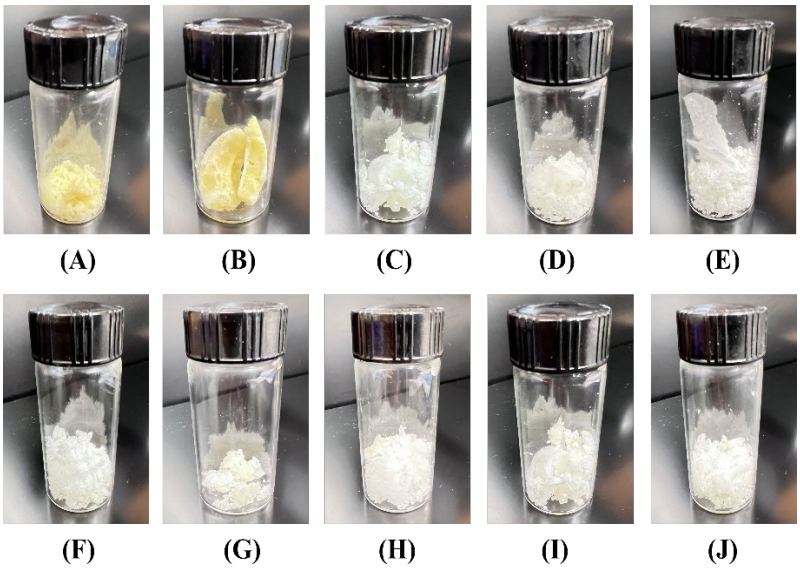

Figure 39. Photos of different pEtC1 samples with synthesis conditions as listed in Table 8.

Synthesis of Novel Fixed-Site Carrier—pEtC2

In poly(ethylene C2) (pEtC2), the C2 reactive sites can potentially react with CO_2 more efficiently compared to the C1 sites in pEtC1. As shown in Figure 40, pEtC2 was synthesized by a polycondensation reaction that was similar to pEtC1. The bifunctional monomer A is identical to that used for pEtC1. The trifunctional monomer B, however, belongs to the same class of compound as monomer A. In the presence of an acidic catalyst, monomer B was protonated and reacted with monomer A. The synthesis procedure was separated into two steps. At the first step (pre-polymerization), the polycondensation reaction was operated at 1 atm with N_2 flushing in. At the second step (polymerization), the reaction was operated at 10 torr. Our main goal was to maximize the MW by optimizing the monomer ratio.

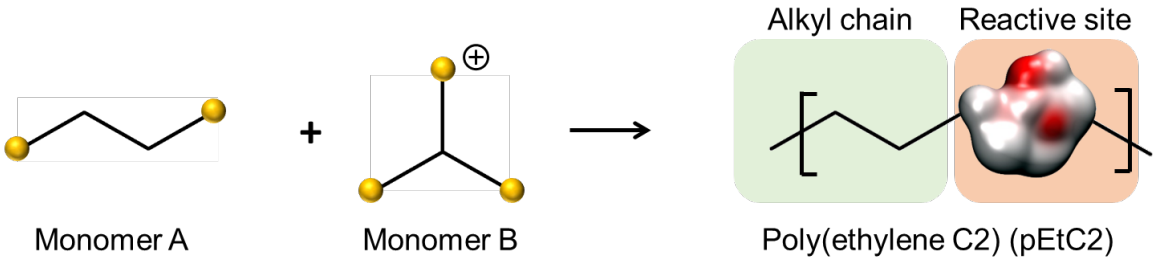

Figure 40. Synthesis scheme of pEtC2 by a bifunctional monomer A and a trifunctional monomer B.

In order to optimize the synthesis conditions for pEtC2, seven batches of polymers (Samples A–G) were synthesized, and the conditions are summarized in Table 9. Accordingly, the photos of the polymer samples are shown in Figure 41. For Samples A and B, the monomer ratio was increased step-wisely while maintaining a relatively stable vapor temperature throughout the polymerization by operating to 160°C. With the increased monomer ratio, the polymer MW

increased from 2.7 to 8.4 MDa. The monomer ratio was then optimized to a moderately high level via the design of experiment approach by using the JMP software [44]. For Samples C–G, the temperature file used for Step 1 was mainly optimized. As shown in Figure 41, the resultant products gradually became more solid and more transparent as the MW increased [21]. By employing the predicted optimal condition, we obtained the sample G with a determined MW of 30 MDa in the static light scattering (SLS) experiment [20], which was the highest MW obtained so far.

Table 9. Synthesis conditions for pEtC2.

Sample	Monomer ratio	Vacuum (torr)	Step 1/2 Temperatures (°C)	Step1/2 Reaction time	Molecular weight (MDa)
A	low	10	160/220	Medium/Low	2.7
B	Medium	10	160/220	Medium/Low	8.4
C	Moderate	10	140/240	High/Low	15
D	Moderate	10	140/240	Medium/Low	21
E	Moderate	10	120/240	High/Low	24
F	Moderate	10	120/230	High/Low	26
G	Moderate	10	120/220	Moderate/Low	30

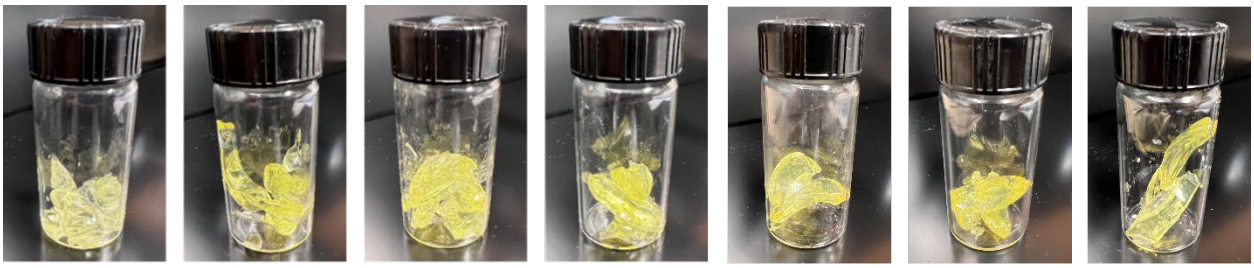

Figure 41. Photos of different pEtC2 samples with synthesis conditions as listed in Table 9.

3.10 Task 10 – Optimized Membrane Characterization

Summary

- The best membrane containing pEtC1 as well as a proprietary aminoacid salt (AAS) carrier showed 4189 GPU CO_2 permeance and 162 CO_2/N_2 selectivity at 77°C.
- The best membrane containing pEtC2 showed 2211 GPU CO_2 permeance and 107 CO_2/N_2 selectivity at 77°C.
- Using the ^{13}C Nuclear Magnetic Resonance (NMR) spectroscopy, the reaction products of CO_2 with exemplary AAS carriers were successfully identified.

- The effects of the chemical properties and structures of the AASs on their CO_2 absorption capacity and the preferred reaction pathway were analyzed.

Membranes Containing pEtC1

In order to investigate the performance of the synthesized pEtC1 in facilitating the CO_2 transport, pEtC1 (7.7 MDa, Sample E in Table 8) was blended with a high MW polyamine to form membranes. An proprietary AAS mobile carrier was also blended in to enhance the facilitated transport of CO_2. These membranes were tested at 77°C and the CO_2/N_2 separation performances are shown in Figure 42. With increasing AAS content, the CO_2 permeance increased from 2211 to 4189 GPU with an improved CO_2/N_2 selectivity from 107 to 162, which has reached the target region. Figure 1.8 also compares the CO_2/N_2 transport performance of membranes containing pEtC1 vs. the 2008 Robeson upper bound. As shown, the pEtC1-containing membranes are superior to polyamine and non-reactive polymers. Therefore, the best membrane derived from this study was used for membrane scale-up, which will be discussed in Task 11.

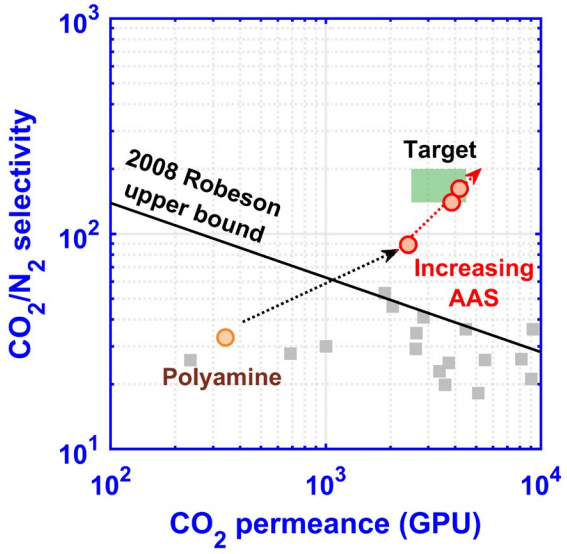

Figure 42. CO_2/N_2 transport performance of membranes containing pEtC1 and AAS vs. the 2008 Robeson upper bound. The Robeson upper bound is converted assuming a membrane thickness of 200 nm. The grey squares (■) represent non-reactive polymers as reviewed by Han and Ho [41].

Membranes Containing pEtC2

In order to investigate the performance of the synthesized pEtC2 in facilitating the CO_2 transport, pEtC2 (15 MDa, Sample C in Table 9) was blended with a high MW polyamine to form membranes with different weight ratios between them for gas permeation tests at 77°C. Here, the polyamine was to form the membrane matrix as well as increasing the coating solution viscosity. As shown in Figure 43, increasing the pEtC2 content resulted in an increase in CO_2 permeance but a reduced selectivity. The best membrane exhibited a CO_2 permeance of 2211 GPU with a CO_2/N_2

selectivity of 107. These trends were caused by the limited MW of pEtC2 in that the polymer chain entanglement was weakened by the addition of pEtC2.

Figure 43 also compares the CO_2/N_2 transport performance of membranes containing pEtC2 vs. the 2008 Robeson upper bound. As shown, the pEtC2-containing membranes are superior to polyamine and non-reactive polymers. Compared with the high performance target region as depicted by the red shade, pEtC2 shows a promising CO_2 permeance but lacks the CO_2/N_2 selectivity. In order to further enhance the membrane performance, we proposed to incorporate mobile carriers in the pEtC2-containing membranes in order to improve their selectivity. The addition of mobile carrier could also improve the overall CO_2 permeance.

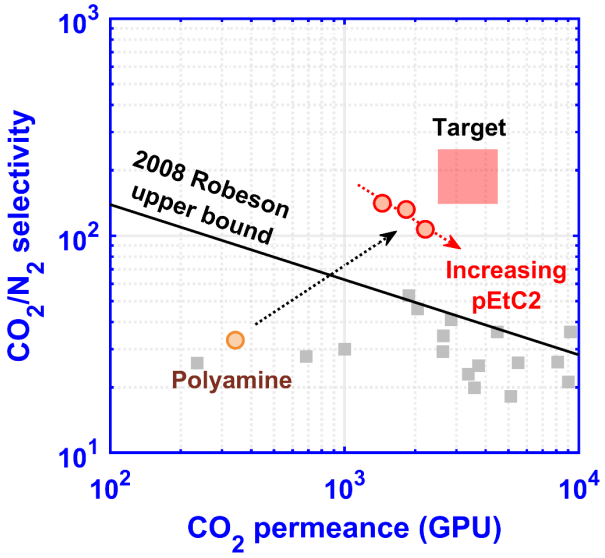

Figure 43. CO_2/N_2 transport performance of membranes containing pEtC2 vs. the 2008 Robeson upper bound. The Robeson upper bound is converted assuming a membrane thickness of 200 nm. The grey squares (■) represent non-reactive polymers as reviewed by Han and Ho [41].

Quantitative ^{13}C NMR Characterization for CO_2–AAS Reaction Chemistry

The selection of mobile carriers is crucial to the gas separation performance of facilitated transport membranes (FTMs), especially for those with a high content of mobile carriers. The FTM performance is largely dependent on the CO_2 facilitation ability of the selected mobile carrier. In order to investigate the CO_2–AAS reaction chemistry, the species of the reaction products were directly characterized using the ^{13}C NMR spectroscopy. Four exemplary AAS carriers, piperazine glycinate (PZ-Gly), 2-(1-piperazinyl)ethylamine glycinate (PZEA-Gly), 2-(1-piperazinyl)ethylamine sarcosinate (PZEA-Sar), and 2-(1-piperazinyl)ethylamine *N*-methyl-alaninate (PZEA-MAla) were chosen (Figure 44).

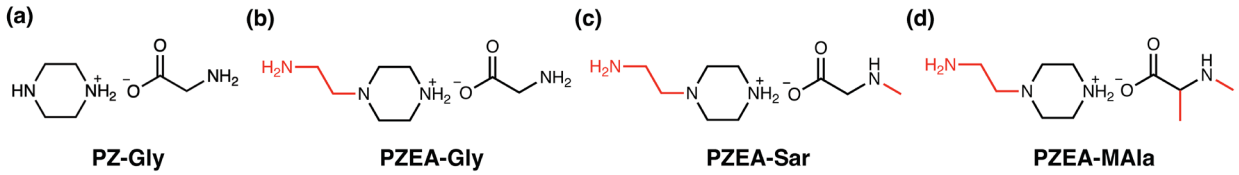

Figure 44. Chemical structures of (a) piperazine glycinate (PZ-Gly), (b) 2-(1-piperazinyl)ethylamine glycinate (PZEA-Gly), (c) 2-(1-piperazinyl)ethylamine sarcosinate (PZEA-Sar), and (d) 2-(1-piperazinyl)ethylamine *N*-methyl-alaninate (PZEA-MAla). The structural differences between PZ-Gly and other AASs are labeled in red color.

Carbamate and bicarbonate products are the dominant amine–CO_2 reaction products. CO_2 reacts with the amino groups present in AAS to form these products. For the carbamate products, they can be classified into two categories: mono-carbamate and di-carbamate. The mono-carbamate formation is a two-step process involving the formation of a zwitterion intermediate (Eq. (1)) followed by a proton-exchange reaction with another amino group (Eq. (2)):

$$CO_2 + R\text{–}NH_2 \rightleftharpoons R\text{–}NH_2^+\text{–}COO^- \quad (1)$$

$$R\text{–}NH_2^+\text{–}COO^- + R\text{–}NH_2 \rightleftharpoons R\text{–}NH\text{–}COO^- + R\text{–}NH_3^+ \quad (2)$$

This mechanism was proposed by Caplow [8] and reinforced by experimental [9] and theoretical [10] studies of the reaction between monoethanolamine (MEA) and CO_2. The carbamate product requires two amino groups to capture one CO_2 molecule (0.5 mol CO_2/mol N) and only forms on the primary or secondary amino group. In order to form a di-carbamate, a multi-amine must be involved, in which carbamate ions are generated subsequentially on different amino sites [45,46].

In contrast with carbamate products, one molecule of bicarbonate product is produced for every molecule of CO_2 (1 mol CO_2/mol N) via base-catalyzed CO_2 hydration by a primary, secondary, or tertiary amino group in the presence of water (Eq. (3)) [47]:

$$CO_2 + H_2O + R_1R_2\text{–}NH \rightleftharpoons R_1R_2\text{–}NH_2^+ + HCO_3^- \quad (3)$$

Therefore, AAS mobile carriers that exhibit more preference toward the bicarbonate pathway are expected to have a theoretical advantage in CO_2 absorption, as previously shown by Eqs. (1)–(3). In order to determine the reaction pathway preference of the AAS carriers and CO_2, the reaction product distribution in each AAS was analyzed based on the corresponding signals in the ^{13}C NMR spectra. The amounts of total reaction product and the distributions in carbamate and bicarbonate products (mol/mol AAS) of PZ-Gly, PZEA-Gly, PZEA-Sar, and PZEA-MAla were compared and are shown in Figure 45.

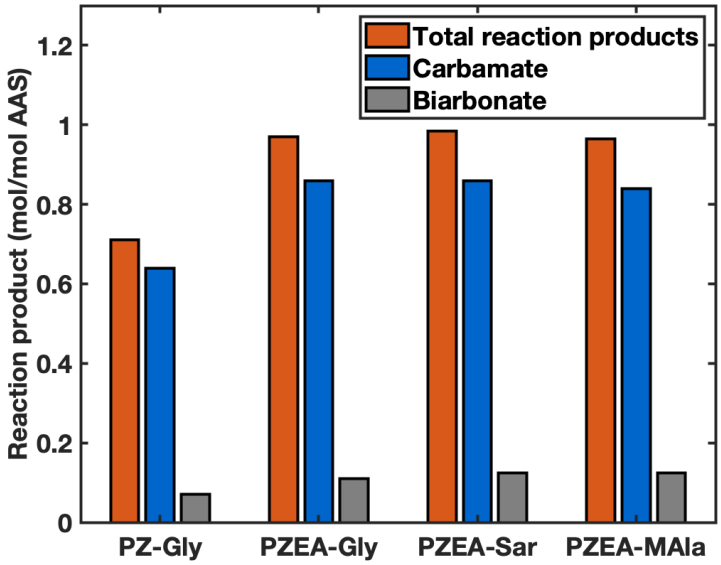

Figure 45. Total reaction products and distributions of carbamate and bicarbonate products for PZ-Gly, PZEA-Gly, PZEA-Sar, and PZEA-Mala.

The results in Figure 45 show that the AAS carriers with $PZEA^+$ as the cation had similar CO_2 loading values (0.970, 0.985, 0.965 mol CO_2/mol AAS for PZEA-Gly, PZEA-Sar, and PZEA-MAla, respectively), which were all higher in comparison to PZ-Gly (0.710 mol CO_2/mol AAS). The greater CO_2 loadings in the PZEA-based AASs were due to the greater amounts of absorbed CO_2 in the form of both carbamate and bicarbonate products. The higher CO_2 loading of PZEA-Gly than PZ-Gly also indicated that PZEA was more effective than PZ for the AAS synthesis. In addition, for all the AASs investigated, the amine–CO_2 reaction predominantly followed the carbamate pathway under the low CO_2 partial pressure condition. The significant pathway preference was shown by the ratios of 6.7–9.1 between carbamate and bicarbonate products. This was consistent with the simulation result of the preferential formation of carbamate products by AASs, as determined theoretically by comparing the stability difference between the carbamate and bicarbonate products [48]. However, when only the PZEA-based ASS carriers were considered, the carbamate products were at the value of 0.86 (mol/mol AAS) in PZEA-Gly and PZEA-Sar but slightly lower in PZEA-MAla of 0.84 (mol/mol AAS). The reduced formation of the carbamate product could be due to the steric hindrance introduced by the second methyl group on the α-carbon (α-C) of MAla. Additionally, the bicarbonate product was found to increase as the pKa value of the amino group increased.

As carbamate products were abundant compared with the bicarbonate products, the distribution of carbamate products of PZ-Gly, PZEA-Gly, PZEA-Sar, and PZEA-MAla were further analyzed, and the results are summarized in Figure 46.

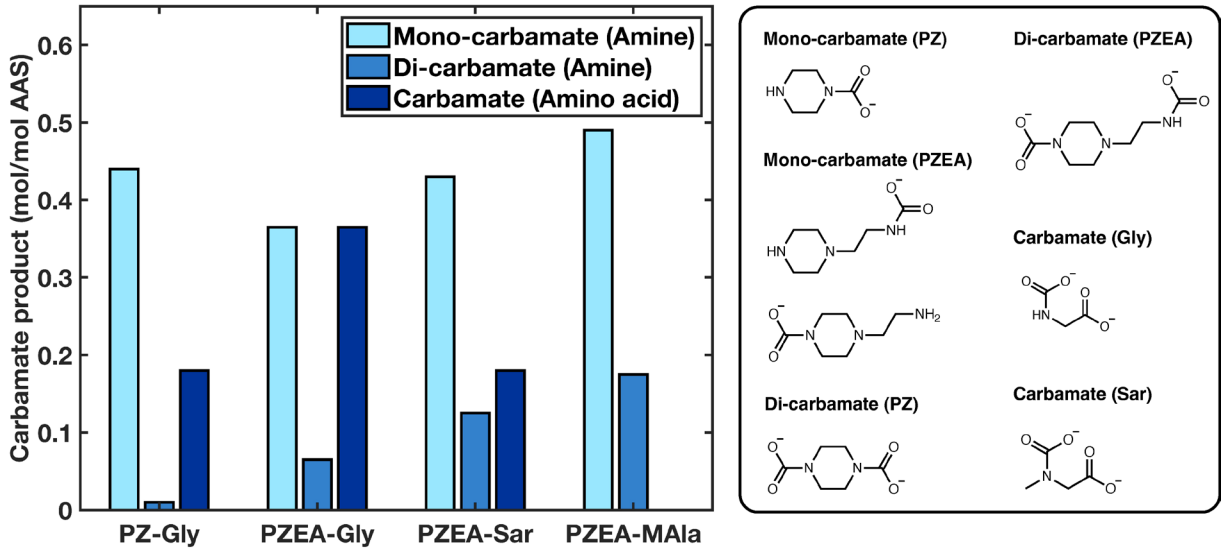

Figure 46. Distributions of carbamate products of PZ-Gly, PZEA-Gly, PZEA-Sar, and PZEA-MAla. The carbamate products of the respective amines and aminoacids are shown on the right.

As shown in Figure 46, the carbamate products could be categorized in three groups: (1) mono-carbamate (where one amino group had formed carbamate with CO_2 while there was another free amino group yet to react with CO_2), (2) di-carbamate (where two carbamate groups were simultaneously formed), and (3) carbamate (where the only amino group had formed carbamate with CO_2). For PZ-Gly following the carbamate pathway, the majority of carbamate products (70%) were PZ mono-carbamates. On the other hand, PZ di-carbamates made up no more than 2% of the overall carbamate products. The insignificant amount of PZ di-carbamate product suggested that its formation was not fully prohibited but was much less thermodynamically favorable than the formation of PZ mono-carbamate [49]. Based on this result, PZ di-carbamate product was expected to make only a minor contribution to CO_2 loading and CO_2 facilitation in the FTM containing PZ-Gly.

In contrast, for PZEA-based AASs following the carbamate pathway, PZEA di-carbamate products contributed more significantly as compared to PZ, though PZEA mono-carbamates still remained the major carbamate products. The difference in the amount of di-carbamate product formation between PZ and PZEA might be attributed to the increased steric hindrance after the PZ mono-carbamate was formed. It was found that the ring structure of PZ exhibited very little steric hindrance before reacting with a CO_2 molecule. However, the formation of mono-carbamate significantly changed the >C–N–H bond angle on the opposite side of the PZ ring, which hindered the formation of PZ di-carbamate [50]. In addition, as the aminoacids in the PZEA-based AAS carriers became more sterically hindered, the carbamate products were reduced from 0.73 on Gly to 0.36 on Sar (mol/mol AAS), and finally was entirely prohibited in MAla. This can be attributed to the reduced stability of carbamate [51].

For the PZEA-based AAS carriers, although the distribution of carbamate products was dependent on the structure of the aminoacid, the total amount of carbamate products remained relatively unchanged (Figure 45). From Figure 46, we observed that when the formation of aminoacid carbamate reduced, there was a strictly increasing amount of CO_2 that was stabilized as

PZEA mono-carbamates and PZEA di-carbamate, instead of generating a comparably increased amount of the bicarbonate product. The results indicated that CO_2 reacted with the PZEA-based AAS to form carbamate products, preferentially at the less hindered N sites, rather than to form a bicarbonate product. This finding suggested that, in order to synthesize multi-amine AAS with improved reaction chemistry that favors bicarbonate formation, one should focus on enhancing the steric hindrance of the primary amino group, rather than on those that are already hindered.

3.11 Task 11 – Scale-up Membrane Fabrication

Summary

- 21″ wide new PES support was fabricated for >100 ft in length using the roll-to-roll continuous casting machine.
- The roll-to-roll continuous coating of a membrane containing Carrier 1 was successfully conducted on the 21″ wide PES support.

Roll-to-Roll Continuous Casting of Polymer Support

The new PES polymer support with optimized surface and bulk morphologies were synthesized to reduce the mass transfer resistances associated with the openness of the support layer [1,2-4]. The synthesis conditions have been systematically explored in the lab scale, which are transferrable to a roll-to-roll continuous casting process. In order to prepare for the pilot-scale membrane coating, the casting machine at OSU has been adjusted to fabricate the polymer support with a width of 21 inches.

The schematic of the casting machine is shown in Figure 47 (a). The non-woven fabric web is connected to the unwind and rewind motors of the casting machine with the web path through a humidity chamber and a water coagulation bath. The casting solution is continuously cast onto the non-woven fabric moving at a speed of 5 ft/min by a stationary stainless-steel knife with a pre-determined gap setting. Compared to the casting conditions used previously, the web speed has been increased by 1 ft/min in order to improve the manufacturing efficiency. A tension of 6 lb_f is applied to ensure the flatness of the fabric. The trough holding the casting solution is purged with N_2 to prevent the casting solution from phase separation. The humidity chamber is installed behind the casting knife. Humid N_2 at room temperature is flowed into the humidity chamber to control the relative humidity. After being exposed to the humid N_2, the cast film is immersed into the coagulation bath to form the nanoporous polymer support.

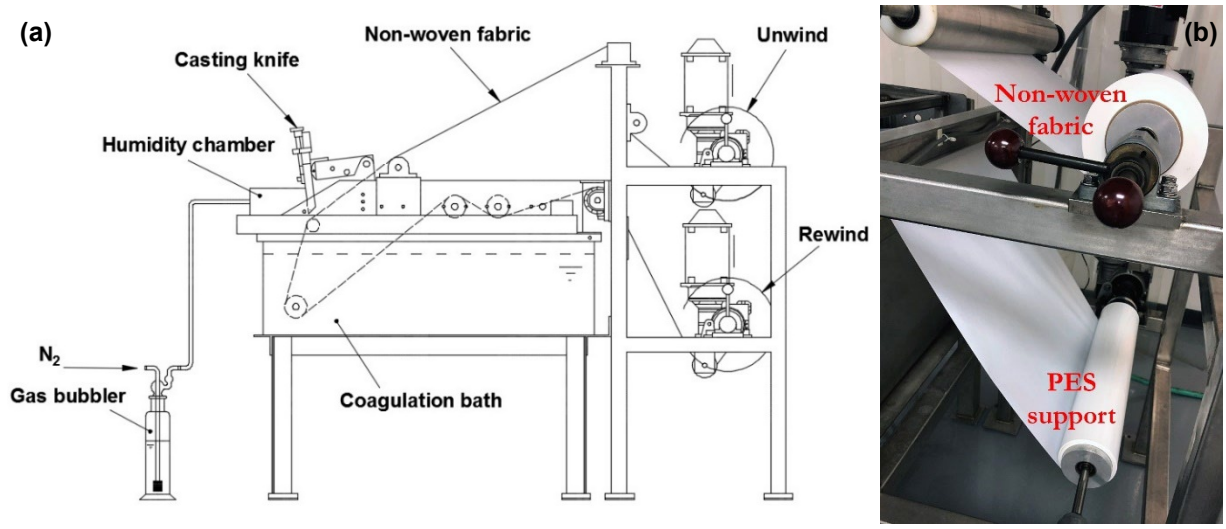

Figure 47. (a) Schematic of continuous casting machine at OSU and (b) photo of a roll of non-woven fabric on the unwind roller and a roll of the fabricated PES support on the rewind roller.

Not shown in Figure 47 (a) is a leveling laser, which aids the alignment of the web. A single-pass reverse osmosis (RO) desalination system is configured to produce high-purity water for the coagulation bath. A dehumidifier is also installed to control the surrounding room humidity. These engineering controls benefit the operation efficiency. The 21″ wide PES support with a length greater than 100 ft was successfully fabricated in a single run. A photo of the fabricated PES support on the rewind roller is shown in Figure 47 (b).

Roll-to-Roll Continuous Membrane Coating

The roll-to-roll continuous membrane coating was also conducted on the 21″ wide PES support in order to fabricate a sufficient amount of the membrane for the prototype membrane module fabrication. As shown in Figure 48, the PES support was connected to an unwind motor and a rewind motor. In between, the PES support tread through a series of passive rollers. A coating knife with a controlled gap setting was used to coat the selective layer on top of the PES support. The coated membrane was dried in a convection oven before it was picked up by the rewind motor. Two membrane compositions with the advanced fixed-site carriers were used for the scale-up coating, the details of which are listed in Table 10. Currently, ~250 ft of membrane could be fabricated by each run of coating. However, we do not foresee any issues to prevent from the mass production of the membrane with a length of 500–1000 ft.

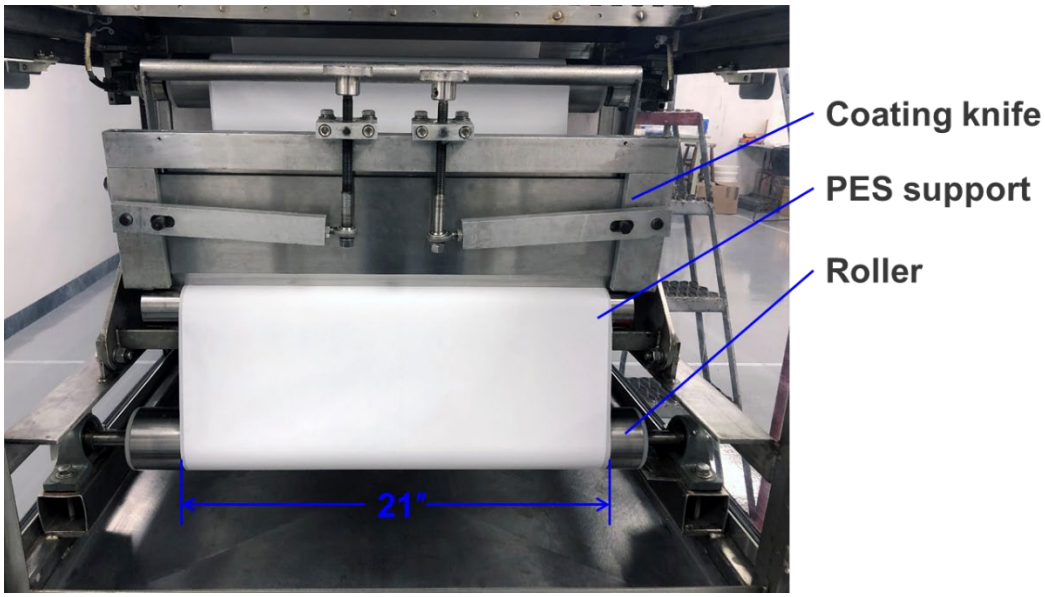

Figure 48. Photo of roll-to-roll continuous membrane coating on 21″ wide PES support.

Table 10. Scale-up coating runs conducted.

Run #	Fixed-site carrier	Mobile carrier	Width (inch)	Length (ft)
1	pEtC1	Proprietary AAS	21	100
2	pEtC2	Proprietary AAS	21	250

3.12 Task 12 – Scale-up Membrane Characterization

Summary

- The scale-up PES support exhibited a surface pore size of 36.6 nm, a porosity of 34.9%, and a CO_2 permeance of 316,000 GPU, which were the best results obtained so far.
- The scale-up membrane samples showed an average CO_2 permeance of 4203 GPU and a CO_2/N_2 selectivity of 165 at 77°C, well above the 2019 Robeson upper bound.

Characterization of Scale-up PES Support

Figure 49 shows the surface and cross-section morphologies of the new scale-up PES support characterized by scanning electron microscopy (SEM). As shown, the new support exhibited a morphology with bicontinuous structure. The average surface pore size and surface porosity were 36.6 nm and 34.9%, respectively. The measured CO_2 permeance was 316,000 GPU. These results were the best so far. The SEM morphologies of the scale-up support were on par with those of the support fabricated in lab scale.

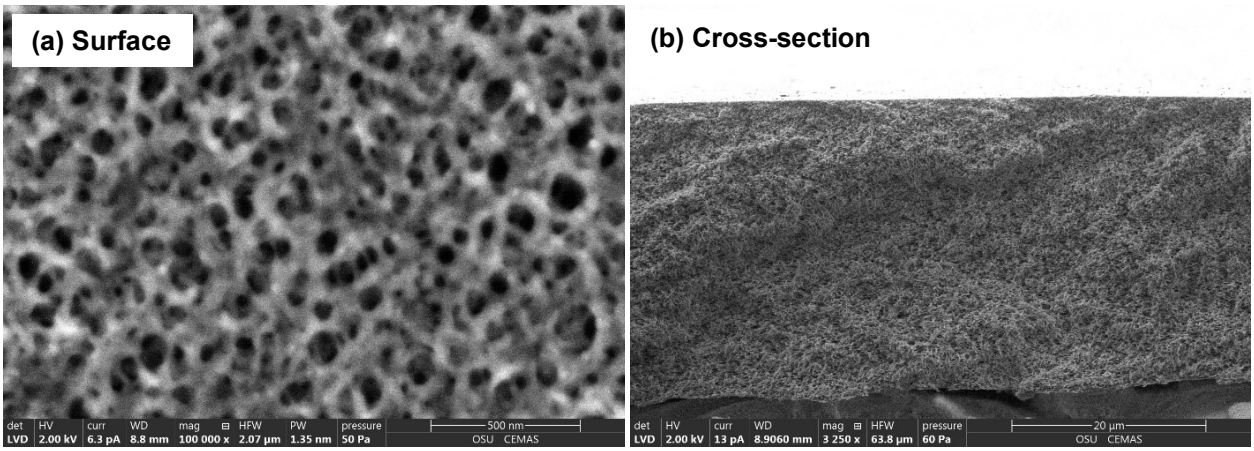

Figure 49. SEM images of scale-up PES supports: (a) surface and (b) cross-section.

Characterization of Scale-up Membrane

Figure 50 shows the transport performance of the scale-up membrane with a feed gas containing 20% CO_2 and 80% N_2 (dry basis). The feed gas was fully saturated with water vapor at 4 atm, while a vacuum of 0.4 atm was pulled on the permeate side. Two temperatures were employed for the testing, i.e., 67 and 77°C. Samples from different locations on the scale-up membrane were tested. At 67°C, the membrane exhibited a CO_2 permeance of 2405±80 GPU and a CO_2/N_2 selectivity of 185±11. When the temperature was elevated to 77°C, the CO_2 permeance increased to 4203±120 GPU with a slightly reduced selectivity of 165±15. At both temperatures, the membrane performances were well above the 2019 Robeson upper bound [52], which was owing to the advanced carriers employed in the transformational membrane.

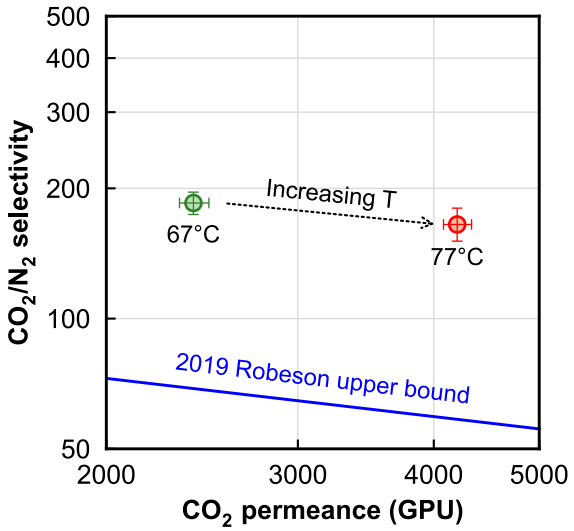

Figure 50. Transport performance of the scale-up membrane with pEtC2 as the fixed-site carrier at 67 and 77°C.

3.13 Task 13 – Prototype Membrane Module Fabrication

Summary

- Three 8″-diameter spiral-wound (SW) elements were fabricated using the scale-up membrane containing pEtC2 as the fixed-site carrier, which were for Stage 1 in the integrated bench skid.
- Three 5″-diameter SW element were also fabricated for Stage 2 in the integrated bench skid.
- Totally, three sets of SW elements (each set consisting of an 8″-diameter SW element for Stage 1 and a 5″-diameter SW element for Stage 2) were prepared for the upcoming NCCC testing.

Fabrication of Prototype SW Membrane Modules

We fabricated three commercial-diameter SW elements with the scale-up membrane containing pEtC2 as the fixed-site carrier. The elements were ⌀8″ in diameter with a length of 22″, which contained 41 membrane leaves, each with a width of 20″ and a length of 36″. Therefore, each individual element possessed a membrane area of 35 m^2. Photos of the fabricated SW membrane element and assembled module and the end view of the element fitted in the module housing are shown in Figure 51 (a) and (b), respectively. The feed gas was introduced through the connection on the side of the end cap on one end of the module, with the retentate coming out on the other end. For Stage 1 in the integrated bench skid, 15% of the retentate is recycled as a sweep gas, which enters the module via the center tube. This countercurrent configuration is designed for the Stage 1.

Figure 51. Photos of (a) ⌀8″ SW membrane module with membrane containing pEtC2 and (b) the end view of the element fitted in the module housing.

We also fabricated three ⌀5″ SW elements, which were for Stage 2 in the bench skid. The element contained 14 membrane leaves, each with a width of 20″ and a length of 36″, resulting in a membrane area of 12 m^2. Photos of the fabricated crossflow SW membrane element and assembled module and the end view of the element fitted in the module housing are shown in Figure 52 (a) and (b), respectively. The feed gas was introduced through the connection on the side of the end cap on one end of the module with the retentate coming out on the other end, while the permeate was withdrawn via the center tube by a vacuum pump.

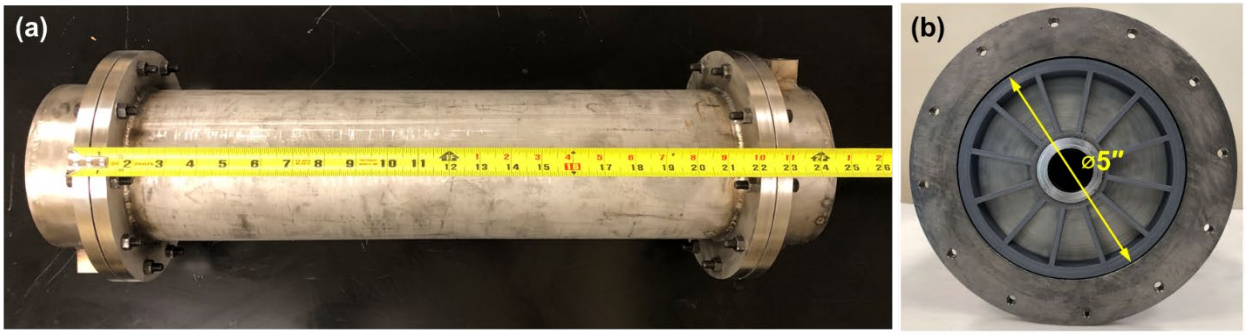

Figure 52. Photos of (a) ⌀5″ SW membrane module with membrane containing pEtC2 and (b) the end view of the element fitted in the module housing.

Totally, three sets of SW membrane elements, each included an ⌀8″ countercurrent element and a ⌀5″ crossflow element, were prepared for the upcoming field test at NCCC. Two sets of the SW elements will be used as spares.

3.14 Task 14 – Prototype Membrane Module Testing

Summary

- The ⌀8″ prototype module was tested with a simulated flue gas. It exhibited an average CO_2 permeance of 4217 GPU and a CO_2/N_2 selectivity of 171. The CO_2/N_2 separation performance was on par with the lab-scale membrane.
- One ⌀8″ prototype module was tested with a simulated coal flue gas containing 13% CO_2 corresponding to the Stage 1 conditions. About 90% CO_2 removal was achieved with ~45% CO_2 purity on dry basis.
- One ⌀5″ prototype module was tested with a simulated feed gas corresponding to the Stage 2 conditions. 95% CO_2 purity was achieved at the designed CO_2 recovery of ~80%, resulting in an overall CO_2 recovery of at least 90% for the designed 2-stage process.

Testing of ⌀8″ Prototype SW Membrane Module

The ⌀8″ prototype SW membrane module fabricated with pEtC2 reported previously was continuously tested. The SW membrane module was tested with a simulated flue gas (at a flow rate of 292 kg/h) containing 20.0% CO_2, 48.4% N_2, 15.0% O_2, 16.6% H_2O, 3 ppm SO_2, and 3 ppm NO_2 at 77°C for about 200 h. The feed and permeate pressures were controlled at 2.5 and 0.8 atm, respectively. This set of conditions was referred to as Conditions ①. Then, the module was tested using a simulated flue gas of the natural gas combined cycle (NGCC) consisting of 4.1% CO_2 for about 400 h (Conditions ②), and a simulated coal-derived flue gas containing 13% CO_2 (Conditions ③) for about 500 h. Under these two simulated flue gases, the feed pressure was increased to 4 atm. The test conditions were then alternated between ② and ③ for two cycles, resulting in a total test time of 2000 h. As shown in Figure 53, the module exhibited an average CO_2 permeance of 4217 GPU and a CO_2/N_2 selectivity of 171 and remained stable for ca. 2000 h,

which are believed to be the highest combined permeance/selectivity membrane performance for carbon capture. Thus, the fabrication of the commercial-size 8-inch diameter prototype SW membrane module was successful.

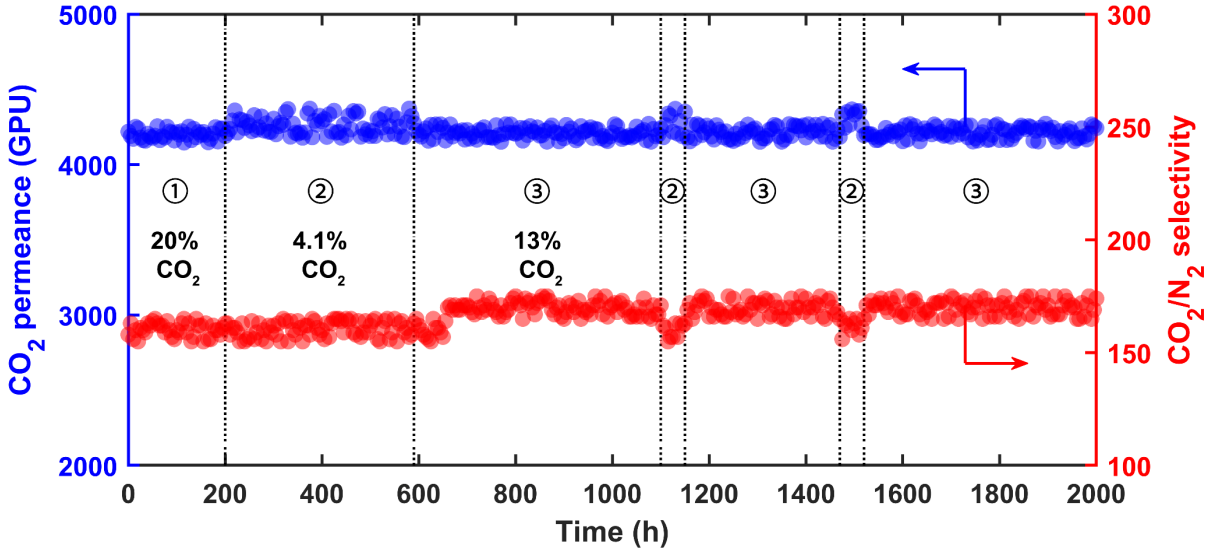

Figure 53. CO_2 permeance and CO_2/N_2 selectivity of the ⌀8″ prototype SW module at 77°C. ① = Simulated flue gas (20% CO_2); ② = Simulated NGCC flue gas (4.1% CO_2); ③ = Simulated coal flue gas (13% CO_2).

Preliminary Test of ⌀8″ Prototype SW Membrane Module

One ⌀8″ prototype SW membrane module was tested with a simulated coal flue gas containing 13% CO_2, 75.5% N_2, and 11.5% H_2O at 77°C. The feed was controlled at 3.5 atm, while 15% of the retentate was expanded to 1.5 psig and passed as a sweep gas. As shown in Figure 54, a CO_2 recovery of ca. 90% was achieved with a CO_2 purity of ca. 45% (dry basis). The CO_2/N_2 separation performance was consistent with the design of the bench skid.

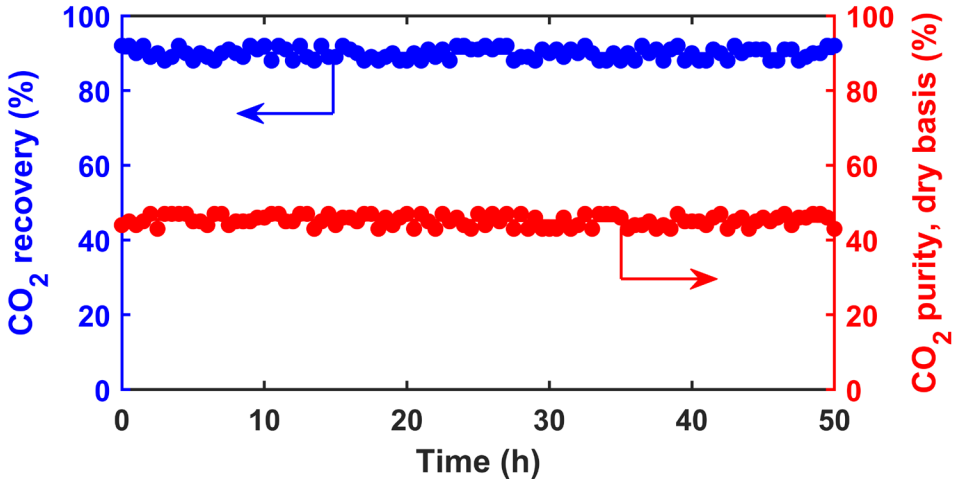

Figure 54. CO_2 recovery and purity (dry basis) of the ⌀8″ prototype SW module under a simulated coal flue gas at 77°C.

Preliminary Test of ⌀5″ Prototype SW Membrane Module

One ⌀5″ prototype SW membrane module was tested with a simulated feed gas containing 38.5% CO_2, 50.0% N_2, and 11.5% H_2O at 77°C. The feed composition corresponded to the feed to the Stage 2 membrane module. The feed and permeate pressures were controlled at 3.5 and 0.8 atm, respectively. As shown in Figure 55, a CO_2 purity of 94.9±1.1% (dry basis) was achieved at a CO_2 recovery of 80.0±1.5%. The CO_2/N_2 separation performance was consistent with the bench skid design of the 2-stage process with an overall CO_2 recovery of at least 90%.

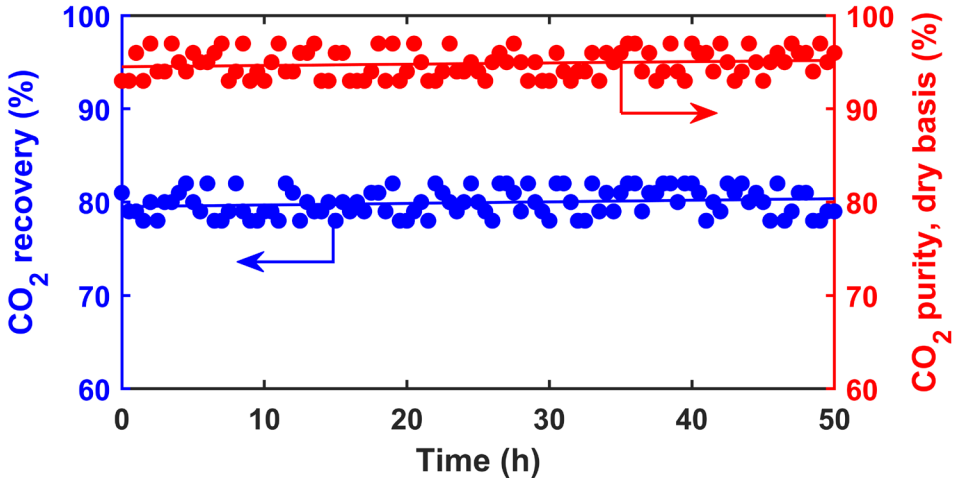

Figure 55. CO_2 recovery and purity (dry basis) of the ⌀5″ prototype SW module under a simulated feed gas at 77°C.

3.15 Task 15 – Skid Testing with Simulated Flue Gas

Summary

- The integrated bench skid was tested with a simulated coal flue gas, achieving 91.0% CO_2 capture and 95.5% CO_2 purity (dry basis).
- A simulated natural gas combined cycle (NGCC) flue gas was also used for the skid testing, resulting in 90.5% CO_2 capture with 95.6% dry CO_2 purity.

Skid Testing with Simulated Coal Flue Gas

The integrated bench skid was tested with a simulated coal flue gas containing 13.0% CO_2, 55.4% N_2, 15.0% O_2, 16.6% H_2O, 3 ppm SO_2, and 3 ppm NO_2 at 77°C. The results are shown in Figure 56. As shown, a CO_2 capture degree of 91.0±0.6% and a CO_2 purity (dry basis) of 95.5±0.3% were achieved. The minor components in the CO_2 product included 4.5% N_2, 9 ppm O_2, 13 ppm SO_2, and 11 ppm NO_2, all on dry basis. The concentrations of these minor components met the CO_2 transportation standard through carbon steel pipeline (i.e., 4–5% N_2, <10 ppm O_2, <100 ppm SO_2, and <100 ppm NO_x) [53]. Subsequently, we conducted the parametric testing and achieved 95% and 99% capture degrees, both with >95% dry CO_2 purity, for 50 h using the simulated coal flue gas. Afterwards, the skid was challenged by a simulated NGCC flue gas containing 4.1% CO_2, 64.3% N_2, 15.0% O_2, 16.6% H_2O, and 3 ppm NO_2 at 77°C. Even the CO_2 concentration was significantly lower than the simulated coal flue gas, the skid still demonstrated a stable 90.5% CO_2 capture with 95.6% dry CO_2 purity for 350 h. In the course of the 1200-h testing, the skid separation performance remained stable. The testing with simulated flue gases has demonstrated not only the good stabilities of both the membrane modules and the 2-stage membrane process, but also the capture targets of both a >90% CO_2 capture degree and a >95% CO_2 purity.

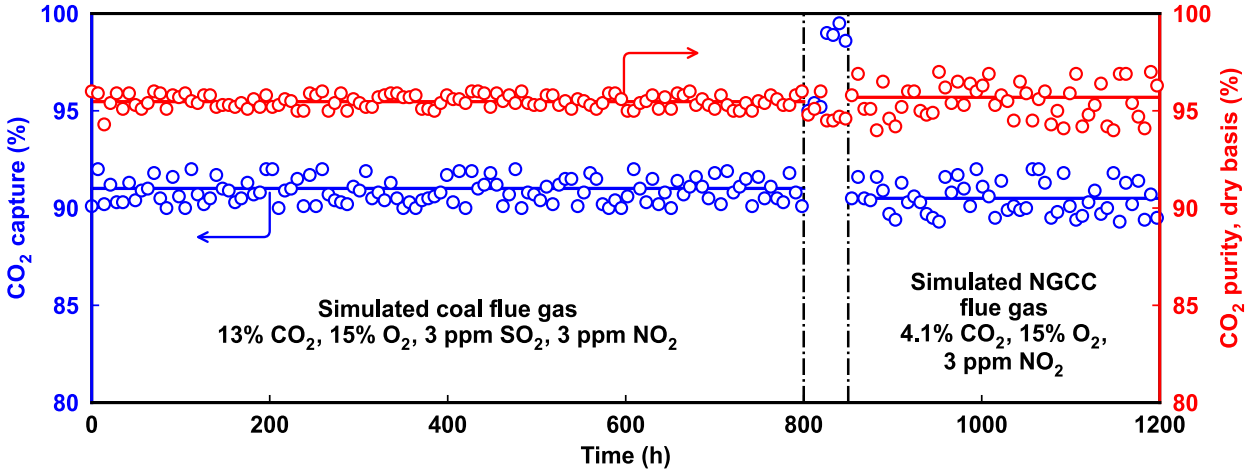

Figure 56. Test results of integrated bench skid with simulated coal and NGCC flue gases at OSU.

3.16 Task 16 – Skid Installation and Commissioning at NCCC

Summary

- OSU and NCCC negotiated and executed a technology collaboration agreement (TCA), which delineated the scope of work and responsibilities during the field trial.
- The integrated bench skid was packaged and delivered to NCCC on October 31, 2022.
- The skid was installed at NCCC, and the commissioning was completed on November 1, 2022.

Skid Shipping, Installation, and Commissioning

A TCA was negotiated between OSU and NCCC to delineate the scope of work and responsibilities during the field trial. Right after the TCA was executed, OSU packaged the bench skid (Figure 57 (a)) and delivered it to NCCC on October 31, 2022. With the assistance of the NCCC staff, the skid was installed in the Lab Scale Testing Unit (LSTU) due to the compact design and thereby the small footprint of the skid (Figure 57 (b)). A flue gas slipstream was brought from the natural gas (NG) boiler to the skid as the feed gas (at a flow rate of 285 kg/h). Utility supplies, including demineralized water, electricity, and analytical gases for gas chromatography analysis, were also connected. Necessary equipment grounding was also carried out by the NCCC electricians. Two OSU personnel installed an ⌀8″, 35-m^2 spiral-wound (SW) element into the first-stage membrane housing and a ⌀5″, 12-m^2 SW element into the second-stage membrane housing. Afterwards, a thorough leak check was conducted in order to ensure (1) the membrane elements were properly installed, (2) the system is gas tight, and (3) the pressure safety valves worked properly. The system was then preheated to 57°C, and the temperature control was closely monitored for 2 h in order to verify the electric resistance heating setup and the thermal insulation. Overall, the skid commissioning was completed on November 1, 2022.

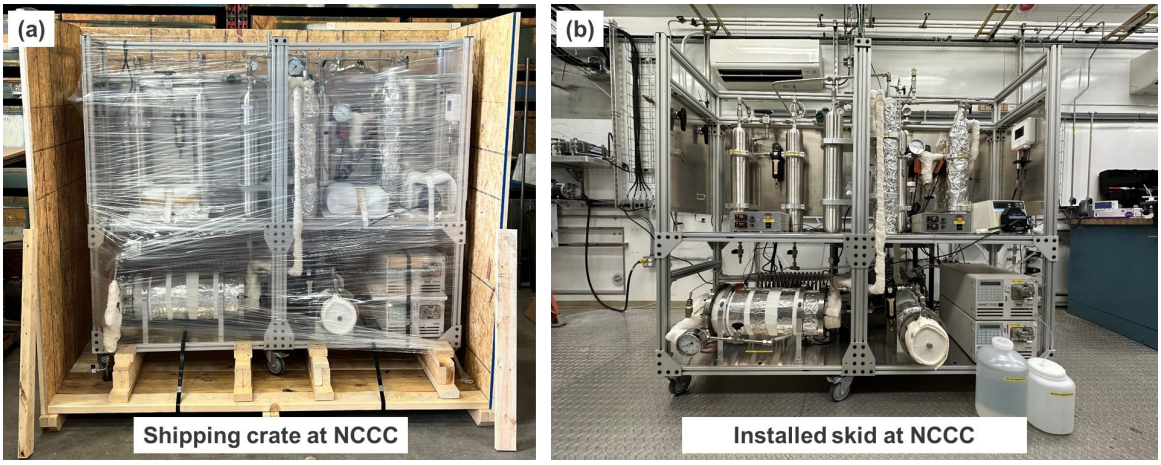

Figure 57. (a) Shipping crate of the bench skid and (b) the installed skid at NCCC.

3.17 Task 17 – Parametric Testing of the Skid at NCCC

Summary

- Parametric testing was conducted under the NG flue gas, and operating conditions for 90 – 99% CO_2 capture were identified.

Parametric Testing with NG Flue Gas

After the skid commissioning was completed, a parametric testing was conducted under the actual NG flue gas containing 8.6% CO_2, 86.2% N_2, 5.2% O_2, and 3 ppm NO_2 (on dry basis). Figure 58 summarizes the testing results including those obtained during the parametric testing. The SW modules were operated at (I) 57°C and 0.2 atm vacuum, (II) 67°C and 0.3 atm vacuum, and (III) 77°C and 0.4 atm vacuum, resulting in 99.1%, 95.4%, and 91.0% CO_2 capture degrees, respectively, with dry CO_2 purities all above 95%. The (III) set of operating conditions was chosen for the steady-state operation.

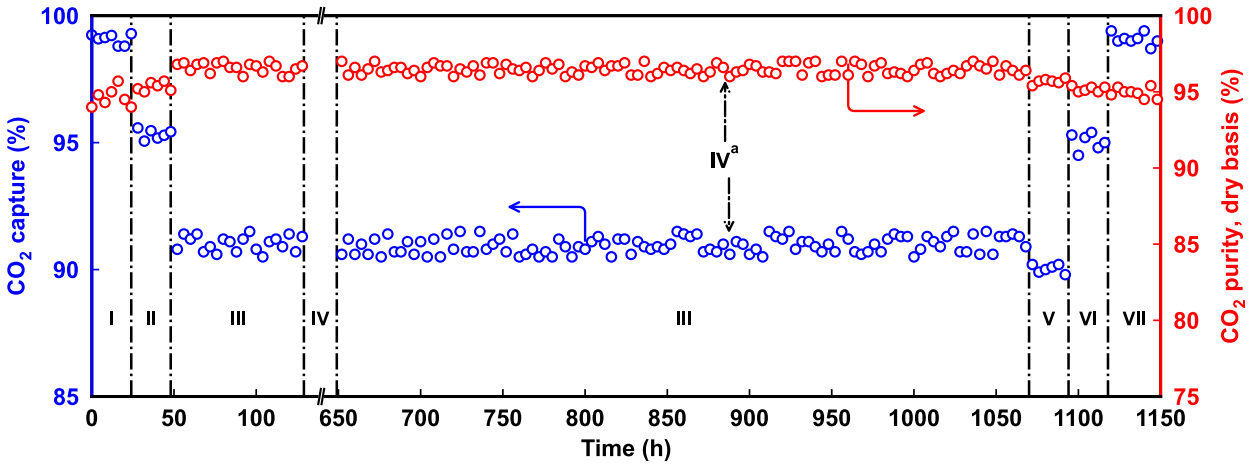

Figure 58. Test results of integrated bench skid with NG and diluted NG flue gases at NCCC.

3.18 Task 18 – Continuous Steady Operation of the Skid at NCCC

Summary

- Cumulatively, the bench skid was tested under the steady-state conditions for 500 h with an average CO_2 capture degree of 91.1% and 96.5% dry CO_2 purity.
- Additional parametric testing was conducted under the diluted NG flue gas to simulate the skid operation under the NGCC flue gas.

Steady-State Operation with NG Flue Gas

Under the (III) set of operating conditions, the skid was operated under steady state to treat the NG flue gas. As shown in Figure 58, a stable separation performance of 91.0% CO_2 capture

with >95% CO_2 purity was achieved for ca. 80 h. After this, the first flue gas shut down (IV) was encountered. The shutdown was caused by the bearing failure of the combustion air blower, which tripped the NG boiler. After the NG flue gas returned, the skid showed resilience with the same CO_2 capture and purity results for ca. 420 h under the steady-state conditions. During the steady-state testing, the NG boiler tripped for a second time (IV[a]), which only led to a short period of low flue gas supply and did not affect the skid performance. Cumulatively, the 500-h runtime of the steady-state testing was reached.

Additional Parametric Testing with Diluted NG Flue Gas

Following the steady-state operation, OSU conducted additional parametric testing when NCCC diluted the NG flue gas by air to simulate the NGCC flue gas with a 4.3% CO_2 concentration. At (V) 77°C and 0.4 atm vacuum, (VI) 67°C and 0.3 atm vacuum, and (VII) 50°C and 0.15 atm vacuum, the skid rendered 90.0%, 95.0%, and 99.0% CO_2 capture degrees, respectively, with dry CO_2 purities all above 95% as shown in Figure 58.

3.19 Task 19 – Final Updated Techno-Economic Analysis

Summary

- Based on the field test results obtained under Tasks 17 and 18, GTI conducted the process simulation of the two-stage membrane process. Heat and material balances were established for 90% capture with a reference to DOE's baseline document "Cost and Performance Baseline for Fossil Energy Plants Volume 1: Bituminous Coal and Natural Gas to Electricity, Revision 4" [54].
- Based on GTI's TEA, the membrane process has a capture cost of $38.92/tonne CO_2 (in 2018 dollars), ~15% lower than Case B12B (i.e., Cansolv, the solvent-based process).
- The final TEA report was submitted to DOE on February 6, 2023 and was approved by DOE on March 21, 2023.

Membrane Performance Results

Under Tasks 17 and 18, transformational membrane performance results were obtained by OSU, which were used for the final TEA conducted by GTI. The membrane performance results as a function of CO_2 concentration are listed in Table 11.

Table 11. The membrane performance results used in the TEA.

CO_2 Concentration	CO_2 Permeance (GPU)	CO_2/N_2 Selectivity
20.0%	4200	160
13.0% (Coal flue gas)	4230	165
4.1% (Natural gas combined cycle flue gas)	4300	170

As listed in Table 11, the membrane performances show typical carrier saturation phenomenon where CO_2 permeance and CO_2/N_2 selectivity increase as CO_2 partial pressure reduces. At lower CO_2 partial pressure, less amine carrier molecules reacted, i.e., more free amine carrier molecules are available in the membrane to transport CO_2, resulting in a higher CO_2 permeance and CO_2/N_2 selectivity. The membrane performances are consistent among following tests: (1) flat-sheet membrane using simulated flue gas, (2) membrane module testing with simulated flue gas, and (3) skid testing using simulated flue gas at OSU and actual natural gas flue gas at NCCC. All simulated flue gases used contained 15% O_2, 3 ppm SO_2, and 3 ppm NO_2.

Final TEA for 90% Capture

In the power plant as shown in Figure 59, flue gas enters the Trim SO_2 Removal Contactor, where it undergoes SO_2 extraction in a distinct caustic-filled section. The flue gas is then compressed using a multistage compressor and cooled in each stage via indirect heat exchange with the cool gas from downstream turboexpander outlet streams. The liquid collected in the compressor inlet and interstage knockouts is returned to the power plant.

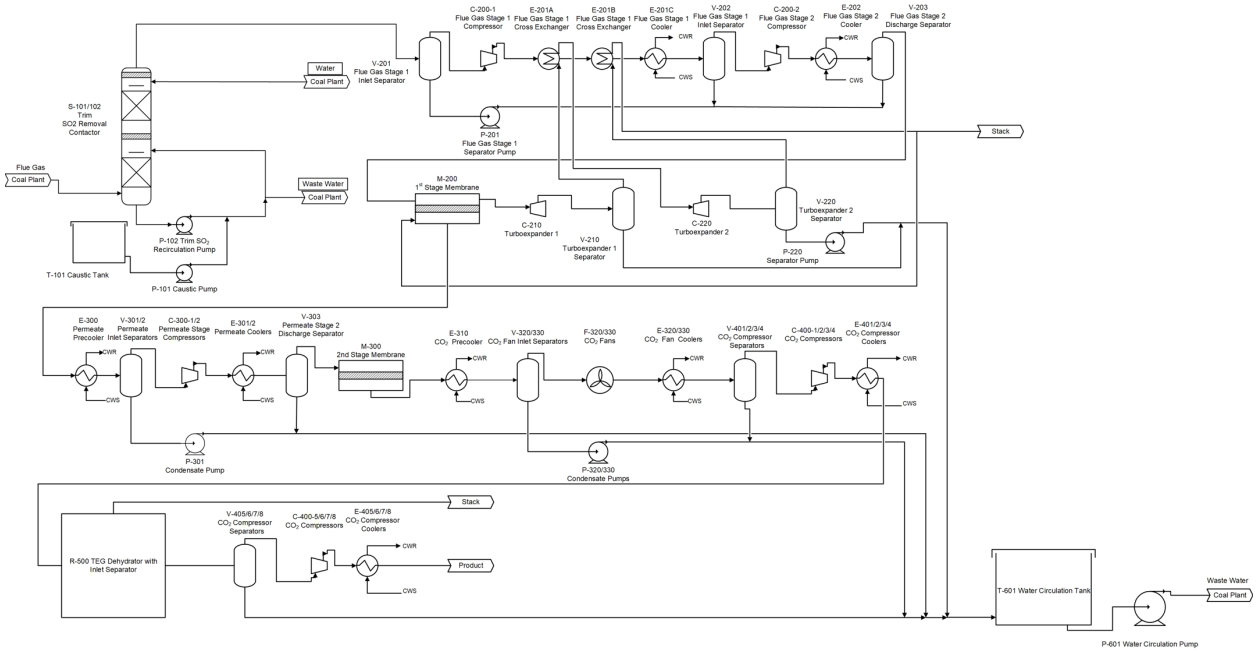

Figure 59. Simplified schematic of the two-stage membrane process for CO_2 capture and compression.

The compressed flue gas proceeds to the first membrane stage, where a portion of the CO_2 permeates through. The membrane's retentate enters the initial turboexpander, which, due to a pressure reduction, results in lower temperature and pressure. This chilled gas serves as a cooling utility for the flue gas compressor's first stage of intercooling. The warmed gas is then directed to a second turboexpander, supplying cool gas for the second stage intercooler. Subsequently, the retentate gas divides into two streams: one is recycled to the first-stage membrane as the sweep on the permeate side, while the other is vented into the atmosphere. Finally, liquids gathered in the turboexpander knockouts are transferred back to the power plant.

The first membrane's permeate undergoes recompression in a secondary multistage compressor, which employs cooling water as a utility for interstage cooling. The liquid accumulated from the interstage coolers is then directed to the power plant. Subsequently, the compressed permeate enters a second membrane stage, where CO_2 permeates, yielding the final CO_2 product. The retentate from this membrane is recycled and combined with the compressed flue gas before reaching the first membrane. The CO_2 product undergoes cooling, compression, dehydration through triethylene glycol (TEG), and further compression in preparation for injection.

The levelized cost of electricity (LCOE) excluding transportation and storage (T&S), and CO_2 capture cost for the membrane process vs. Case B12B (i.e., Cansolv, the solvent-based process) [54] are shown in Table 12. Table 13 provides a detailed breakdown of the capture cost metric by category (capital, fixed, variable, and fuel costs) for both processes and highlights the cost savings between Case B12B and the two-stage membrane process.

Table 12. LCOE and capture cost summary (in 2018 dollars).

		NETL. Rev 4 Case B12A	NETL. Rev 4 Case B12B	Two-stage membrane process
LCOE excluding T&S	$/MWh	$64.4	$105.2	$99.3
Incremental CO_2 capture cost	$/MWh	-	$40.8	$34.9
Increase in COE vs. Case B12A	%	-	63.4%	54.2%
Capture cost	$/tonne	-	$45.63	$38.92

Table 13. Capture cost - contributions by cost category (in 2018 dollars).

Capture cost breakdown	Unit	NETL. Rev 4 Case B12B	Two-stage membrane process	Saving vs. Case B12B	Fraction of overall saving
Capital	$/tonne	$25.34	$21.48	$3.86	58%
Fixed	$/tonne	$7.41	$6.32	$1.09	16%
Variable	$/tonne	$7.05	$5.24	$1.81	27%
Fuel	$/tonne	$5.83	$5.88	–$0.05	–1%
Total	**$/tonne**	**$45.63**	**$38.92**	$6.71	

The two-stage membrane process exhibits a 6% decrease in LCOE when compared to Case B12B, with the membrane process demonstrating a lower LCOE of $99.3/MWh versus $105.2/MWh for Case B12B. This reduction in LCOE can be primarily attributed to the lower capital and variable costs associated with the membrane process. Additionally, the CO_2 capture cost for the two-stage membrane process is $38.92/tonne, which represents a 15% decrease when

compared to Case B12B [54]. The reduction in capital costs accounts for the majority of the overall savings (58%).

3.20 Task 20 – Removal of the Skid from NCCC

This task was completed on February 15, 2023.

4 Success Criteria Status

All the success criteria pertained to this project have been met upon the submission of this report. The criteria concerning the bench-scale membrane performance and the process economics are briefly described as follows:

- Prepare polymer support with CO_2 permeance = 23,000 – 30,000 GPU.
  - This criterion was met in BP1 (12/31/2020) via a series of polyethersulfone (PES) casting solution compositional improvement, including 1) improved hydrophilic modifying agent for incorporation in the PES support, 2) better pore former, and 3) optimized thermodynamic stability of casting solution during vapor-induced phase separation to achieve higher porosity and bicontinuous morphology.
  - The fabrication of the PES support has been further improved from BP1 (10/01/2019) to BP2, which has resulted in the best PES support with an exceptional CO_2 permeance of 316,000 GPU.

- Demonstrate CO_2 permeance = 3000 – 3800 GPU with CO_2/N_2 selectivity = 80 – 140 at ~77°C in BP1.
  - This criterion was met in BP1 (12/31/2020) via a series of compositional improvement, including 1) improved interfacial compatibility between the selective layer and the polymer support to enable ultrathin, defect-free coating, 2) better amine carrier with optimal steric hindrance through density functional theory calculations, 3) optimized nanofiller geometry, and 4) higher MW polyamine synthesized for incorporating a greater amount of mobile carrier in the membrane, preparing a thinner membrane due to a lower concentration coating solution with suitable viscosity, and reducing membrane penetration into the improved porous support to achieve higher CO_2 permeance.
  - The membrane synthesized showed a CO_2 permeance of 3500 GPU and a CO_2/N_2 selectivity of >160.

- Conduct preliminary techno-economic analysis (TEA) showing $40.0 – 41.5/tonne capture cost.
  - This criterion was met in BP1 (06/30/2020). The TEA exhibited a capture cost of $39.60/tonne of CO_2, which was less than the $40.0 – 41.5/tonne capture cost.

- Complete the design of the skid successfully in BP1 (12/31/2020).

- This criterion was met in the end of BP1 (12/31/2020) successfully.

- Demonstrate CO_2 permeance = 3800 – 4000 GPU with CO_2/N_2 selectivity = 140 – 200 at ~77°C in BP2.
  - This criterion was met (by 03/31/2022) via a series of compositional improvement, including 1) better amine carrier with optimal steric hindrance through density functional theory calculations, 2) optimized nanofiller geometry, and 3) higher MW polyamine synthesized for incorporating a greater amount of mobile carrier in the membrane, preparing a thinner membrane due to a lower concentration coating solution with suitable viscosity, and reducing selective-layer coating penetration into the improved porous support to achieve higher CO_2 permeance.
  - The synthesis of the polymer matrix has been further improved from BP2 (01/01/2021) to now, which has led to the most transformational membrane with a CO_2 permeance of 4200 GPU and a CO_2/N_2 selectivity of >160.

- Scale up membrane demonstrating CO_2 permeance = 3800 – 4000 GPU with CO_2/N_2 selectivity = 140 – 200 at ~77°C in BP2.
  - This criterion was met in BP2 (04/30/2022) successfully. The scale-up membrane showed the same performance as the lab-scale membrane, i.e., a CO_2 permeance of 4200 GPU and a CO_2/N_2 selectivity of >160.

- Fabricate spiral-wound (SW) membrane modules showing good membrane performance at ~77°C.
  - This criterion was met in BP2 (05/31/2022). The prototype scale-up membrane was used to fabricate 6 pilot-size membrane modules (each about 20″ length, 3 modules each at the commercial-size diameter of 8 inches with 35 m^2 membrane area for Stage 1 and 3 modules each at 5-inch diameter with 12 m^2 membrane area for Stage 2).
  - The separation performances of the SW membrane modules were on par with the flat-sheet membranes fabricated in pilot scale (via continuous roll-to-roll fabrication) and synthesized in lab scale, i.e., a CO_2 permeance of 4200 GPU and a CO_2/N_2 selectivity of >160.

- Construct the testing skid of a 2-stage membrane process.
  - This criterion was met in BP2 (06/30/2022).
  - The skid consisted of 1 commercial-size 8-inch diameter SW membrane module of 35 m^2 membrane area for Stage 1 and one 5-inch diameter SW membrane module of 12 m^2 for Stage 2.

- Carry out skid testing to demonstrate ≥90% CO_2 capture with ≥95% CO_2 purity with actual flue gas for 500 h at the National Carbon Capture Center (NCCC) in Wilsonville, Alabama.
  - This criterion was met in BP2 (12/31/2023) with the testing of the 2-stage membrane process skid consisting of 1 commercial-size 8-inch diameter membrane module of 35 m^2 membrane area for Stage 1 and one 5-inch diameter membrane module of 12 m^2 for Stage 2.

- The NCCC skid tests showed 90 – 99% CO_2 capture degrees for 8.6% and 4.3% CO_2 concentrations, for actual natural gas flue gas and air-diluted natural gas flue gas, respectively, all with ≥95% CO_2 purity.
- The skid test results were consistent with the membrane performance of 4200 GPU CO_2 permeance along with a CO_2/N_2 selectivity of at least 160.
- The skid test duration using the actual natural gas flue gas was 500 h, and that using the air-diluted natural gas flue gas was about 300 h.

- Conduct final TEA showing $39.5 – 40.0/tonne capture cost.
  - This criterion was met in BP2 (03/31/2023). The final TEA was conducted by the subrecipient Gas Technology Institute using the skid test results obtained. The TEA showed a capture cost of $38.92/tonne of CO_2, which was less than the $39.5 – 40.0/tonne capture cost.

5 State Point Data Table

Table 14. State-Point Data for DE-FE0031731.

	Units	Current R&D Value	Target R&D Value
Materials Properties			
Materials of Fabrication for Selective Layer		Amine-containing polymer	
Materials of Fabrication for Support Layer		Polyethersulfone on non-woven fabric	
Nominal Thickness of Selective Layer (nm)		170	170
Membrane Geometry		Flat sheet	Flat sheet
Max Trans-Membrane Pressure	bar	4	4
Hours tested without significant degradation		3,930	3,930
Membrane Performance			
Temperature	°C	77	77
CO_2 Pressure Normalized Flux	GPU	4,200	4,000
CO_2/H_2O Selectivity	-	1	1
CO_2/N_2 Selectivity	-	165	140
Type of Measurement (Ideal or mixed gas)	-	Mixed gas	Mixed gas
Proposed Module Design			
Flow Arrangement	-	Spiral-wound	
Packing Density	m^2/m^3	~2,000	
Permeate-Side Fluid	-	Vacuum or retentate recycle	

***Definitions*:**

Membrane Geometry – flat discs or sheets, hollow fibers, tubes, etc.

Pressure Normalized Flux – For materials that display a linear dependence of flux on partial pressure differential, this is equivalent to the membrane's permeance.

GPU – Gas Permeation Unit, which is equivalent to 10^{-6} cm^3 / (cm^2 · s · cmHg) at 1 atm and 0 °C. For non-linear materials, the dimensional units reported shall be based on flux measured in cm^3 / (cm^2 · s) (at 1 atm and 0 °C) with pressures measured in cmHg. Note: 1 GPU = 3.3464×10^{-10} mol / (m^2 · s · Pa) [SI units].

Type of Measurement – Either mixed or pure gas measurements; projected permeance and selectivities shall be for mixture of gases found in de-sulfurized flue gas.

Flow Arrangement – Typical gas-separation module designs include spiral-wound sheets, hollow-fiber bundles, shell-and-tube, and plate-and-frame, which result in either co-current, counter-current, cross-flow arrangements, or some complex combination of these.

Packing Density – Ratio of the active surface area of the membrane to the volume of the module.

Shell-Side Fluid – Either the permeate or retentate stream.

6 Milestones and Status Report

Budget Period 1

Table 15. Milestone status report for Budget Period 1.

Milestone Title Description	Planned Completion Date	Actual Completion Date	Verification Method	Comments
Task 1. Project Management & Planning:				
Project Kickoff Meeting Held	09/30/2019	09/13/2019	Presentation file	
Continuation Application Meeting	12/31/2020	11/10/2020	Presentation file	
Updated PMP submitted	07/30/2019	08/02/2019	Updated PMP file	
Task 2. Synthesis of Improved Polymer Support				
Support CO_2 permeance = 23,000–30,000 GPU	03/31/2020	03/31/2020	Polymer support reported in RPPR	
Task 3. Optimized Transformational Membrane Synthesis				
Subtask 3.1. Investigation of CO_2 Carrier Structures				
Complete DFT calculations to identify the carrier structures	12/31/2019	12/31/2019	DFT calculations reported in RPPR	
Subtask 3.2. Incorporation of Nano-fillers				
Nano-filler incorporated in the membrane	06/30/2020	06/30/2020	Nano-filler reported in RPPR	
Subtask 3.3. Synthesis of Higher MW Polyamine				

Synthesis of 3–5 million MW polyamine	12/31/2020	03/31/2020	Polyamine reported in RPPR	
Task 4. Membrane Characterization				
Subtask 4.1. Morphology of Membranes				
Obtain SEMs showing membrane morphologies	12/31/2019	12/31/2019	Morphologies reported in RPPR	
Subtask 4.2. Transport Properties				
Determine CO_2 permeance and CO_2/N_2 selectivity	06/30/2020	06/30/2020	Transport results reported in RPPR	
Subtask 4.3. Membrane stability				
CO_2 permeance = 3,000–3,800 GPU and CO_2/N_2 selectivity = 80–140	12/31/2020	12/31/2020	Stability results reported in RPPR	
Task 5. Preliminary Techno-economic Analysis				
$40.0–41.5/tonne CO_2 for 90% recovery	12/31/2020	12/31/2020	Submission of preliminary TEA report	
Task 6. Design of an Integrated Skid	**12/31/2020**	**12/31/2020**	Skid design reported in RPPR	
Task 7. NCCC Site Preparation	**12/31/2020**	**12/31/2020**	Site preparation reported in RPPR	
RPPRs Submitted	10/30/2019; 01,04,07, 10/30/2020; 01/30/2021	Q1: 10/26/2019 Q2: 01/27/2020 Q3: 04/23/2020 Q4: 07/20/2020 Q5: 10/15/2020 Q6: 01/25/2021	Project Officer	

Budget Period 2

Table 15. Milestone status report for Budget Period 2.

Milestone Title Description	Planned Completion Date	Actual Completion Date	Verification Method	Comments
Task 1. Project Management & Planning:				
Subtask 1.1. State Point Data Table	3/31/2023		Updated Table	
Subtask 1.2. Technology Gap Analysis	3/31/2023		Updated Analysis	
Subtask 1.3. EH&S Risk Assessment	3/31/2023		Updated Assessment	
Subtask 1.4. Technology Maturation Plan	3/31/2023		Updated Plan	
Task 8. Construction of the Bench Skid	**06/30/2022**	06/30/2022	Skid reported in RPPR	
Task 9. Further Optimized Membrane Synthesis	**03/31/2023**			
Improved support and carrier synthesis aided by computational methods	03/31/2022	02/28/2022	Improved membranes reported in RPPR	
Task 10. Optimized Membrane Characterization	**03/31/2022**			
CO_2 permeance = 3800–4000 GPU; CO_2/N_2 selectivity = 140–200	03/31/2022	03/31/2022	Transport results reported in RPPR	
Task 11. Scale-up Membrane Fabrication	**05/31/2022**			
Sufficient amount of membrane fabricated	05/31/2022	05/31/2022	Scale-up membrane reported in RPPR	
Task 12. Scale-up Membrane Characterization	**05/31/2022**			
CO_2 permeance = 3800–4000 GPU; CO_2/N_2 selectivity = 140–200	04/30/2022	04/30/2022	Transport results reported in RPPR	
Task 13. Prototype Membrane Module Fabrication	**05/31/2022**	05/31/2022	Module reported in RPPR	
Task 14. Prototype Membrane Module Testing	**05/31/2022**			
CO_2 permeance = 3800–4000 GPU; CO_2/N_2 selectivity = 140–200	05/31/2022	05/31/2022	Transport results reported in RPPR	
Task 15. Skid Testing with Simulated Flue Gas	**09/30/2022**			

CO_2 permeance = 3800–4000 GPU; CO_2/N_2 selectivity = 140–200	09/30/2022	09/30/2022	Transport results reported in RPPR	
Task 16. Skid Installation and Commissioning at NCCC	**11/30/2022**	11/1/2022	Installation reported in RPPR	
Task 17. Parametric Testing of the Skid at NCCC	**11/30/2022**			
Complete skid parametric testing with prototype modules in-series and conditions for steady state operation identified	11/30/2022	11/3/2022	Capture results reported in RPPR	
Task 18. Continuous Steady Operation of the Skid at NCCC	**12/31/2022**			
Complete steady state operation with modules in series and demonstrate feasibility on capture of the CO_2 with >95% CO_2 purity for >500 h	12/31/2022	12/21/2022	Skid performance reported in RPPR	
Task 19. Final Updated Techno-economic Analysis	**3/31/2023**			
Complete final techno-economic analysis showing the feasibility of $39.5–40.0/tonne CO_2	3/31/2023	3/21/2023	Final TEA Report submitted	
Task 20. Removal of the Skid from NCCC	**01/31/2023**	2/15/2023	Skid removal reported in RPPR	
RPPRs Submitted	4/30/2021; 7,10/30/2021; 01,04/30/2022; 7,10/30/2022; 1/30/2023; 4/30/2023	Q7: 4/20/2021 Q8: 7/19/2021 Q9: 10/25/2021 Q10: 1/20/2022 Q11: 4/30/2022 Q12: 7/25/2022 Q13: 10/28/2022 Q14: 1/27/2023 Q15: 4/15/2023	Project Officer	
Final Technical Report	**06/30/2023**	6/20/2023	Project Officer	

References

1. W. S. W. Ho and K. K. Sirkar, eds., Membrane Handbook, Chapman & Hall, New York (1992), Kluwer Academic Publishers, Boston, reprint edition (2001), Springer US, New York, reprint edition (2012).
2. D. Wu, Y. Han, W. Salim, K. K. Chen, J. Li, and W. S. W. Ho, "Hydrophilic and Morphological Modification of Nanoporous Polyethersulfone Substrates for Composite Membranes in CO_2 Separation", Journal of Membrane Science, 565, 439–449 (2018).
3. D. Wu, L. Zhao, V. K. Vakharia, W. Salim, and W. S. W. Ho, "Synthesis and Characterization of Nanoporous Polyethersulfone Membrane as Support for Composite Membrane in CO_2 Separation: From Lab to Pilot Scale", Journal of Membrane Science, 510, 58–71 (2016).
4. J. Lopez, S. Matson, J. Marchese, and J. Quinn, "Diffusion through Composite Membranes: A Two-Dimensional Analysis", Journal of Membrane Science, 27, 301–325 (1986).
5. C. Smolders, A. Reuvers, R. Boom, and I. Wienk, "Microstructures in Phase-Inversion Membranes. Part 1. Formation of Macrovoids", Journal of Membrane Science, 73, 259–275 (1992).
6. P. Machado, A. Habert, and C. Borges, "Membrane Formation Mechanism Based on Precipitation Kinetics and Membrane Morphology: Flat and Hollow Fiber Polysulfone Membranes", Journal of Membrane Science, 155, 171–183 (1999).
7. R. C. Ruaan, T. Chang, and D. M. Wang, "Selection Criteria for Solvent and Coagulation Medium in View of Macrovoid Formation in the Wet Phase Inversion Process", Journal of Polymer Science Part B: Polymer Physics, 37, 1495–1502 (1999).
8. S.-W. Song and J. M. Torkelson, "Coarsening Effects on the Formation of Microporous Membranes Produced via Thermally Induced Phase Separation of Polystyrene-Cyclohexanol Solutions", Journal of Membrane Science, 98, 209–222 (1995).
9. J. Tsai, Y. Su, D. Wang, J. Kuo, J. Lai, and A. Deratani, "Retainment of Pore Connectivity in Membranes Prepared with Vapor-Induced Phase Separation", Journal of Membrane Science, 362, 360–373 (2010).
10. Y. S. Su, C. Y. Kuo, D. M. Wang, J. Y. Lai, A. Deratani, C. Pochat, and D. Bouyer, "Interplay of Mass Transfer, Phase Separation, and Membrane Morphology in Vapor-Induced Phase Separation", Journal of Membrane Science, 338, 17–28 (2009).
11. H. A. Tsai, C. Y. Kuo, J. H. Lin, D. M. Wang, A. Deratani, C. Pochat-Bohatier, K. R. Lee, and J. Y. Lai, "Morphology Control of Polysulfone Hollow Fiber Membranes via Water Vapor Induced Phase Separation", Journal of Membrane Science, 278, 390–400 (2006).
12. D. G. A. L. Aarts, R. P. A. Dullens, and H. N. W. Lekkerkerker, "Interfacial Dynamics in Demixing Systems with Ultralow Interfacial Tension", New Journal of Physics, 7, 40–40 (2005).
13. R. Pang, K. K. Chen, Y. Han, and W. S. W. Ho, "Highly Permeable Polyethersulfone Substrates with Bicontinuous Structure for Composite Membranes in CO_2/N_2 Separation", Journal of Membrane Science, 612, 118443 (2020).
14. D. Wu, Y. Han, L. Zhao, W. Salim, V. Vakharia, and W. S. W. Ho, "Scale-up of Zeolite-Y/Polyethersulfone Substrate for Composite Membrane Fabrication in CO_2 Separation", Journal of Membrane Science, 562, 56–66 (2018).
15. W.-L. Hung, D.-M. Wang, J.-Y. Lai, and S.-C. Chou, "On the Initiation of Macrovoids in Polymeric Membranes–Effect of Polymer Chain Entanglement", Journal of Membrane Science, 505, 70–81 (2016).

16. Y. Han, D. Wu, and W. S. W. Ho, "Simultaneous Effects of Temperature and Vacuum and Feed Pressures on Facilitated Transport Membrane for CO_2/N_2 Separation", Journal of Membrane Science, 573, 476–484 (2019).
17. Y. Matsuzaki, H. Yamada, F. A. Chowdhury, S. Yamamoto, and K. Goto, "Ab Initio Study of CO_2 Capture Mechanisms in Aqueous 2-Amino-2-Methyl-1-Propanol: Electronic and Steric Effects of Methyl Substituents on the Stability of Carbamate", Industrial & Engineering Chemistry Research, 58, 3549–3554 (2019).
18. O. Rahaman, A. C. van Duin, W. A. Goddard III, and D. J. Doren, "Development of a Reaxff Reactive Force Field for Glycine and Application to Solvent Effect and Tautomerization", The Journal of Physical Chemistry B, 115, 249–261 (2011).
19. B. Zhang, A. C. van Duin, and J. K. Johnson, "Development of a Reaxff Reactive Force Field for Tetrabutylphosphonium Glycinate/CO_2 Mixtures", The Journal of Physical Chemistry B, 118, 12008–12016 (2014).
20. M. Andersson, B. Wittgren, and K.-G. Wahlund, "Accuracy in Multiangle Light Scattering Measurements for Molar Mass and Radius Estimations. Model Calculations and Experiments", Analytical Chemistry, 75, 4279–4291 (2003).
21. Y. Lin, E. Bilotti, C. W. M. Bastiaansen, and T. Peijs, "Transparent Semi‐Crystalline Polymeric Materials and Their Nanocomposites: A Review", Polymer Engineering & Science, 60, 2351‐2376 (2020).
22. Y. Han, D. Wu, and W. S. W. Ho, "Nanotube-Reinforced Facilitated Transport Membrane for CO_2/N_2 Separation with Vacuum Operation", Journal of Membrane Science, 567, 261–271 (2018).
23. J. D. Moon, M. Galizia, H. Borjigin, R. Liu, J. S. Riffle, B. D. Freeman, and D. R. Paul, "Modeling Water Diffusion in Polybenzimidazole Membranes Using Partial Immobilization and Free Volume Theory", Polymer, 122170 (2020).
24. H. Lin, E. Van Wagner, J. S. Swinnea, B. D. Freeman, S. J. Pas, A. J. Hill, S. Kalakkunnath, and D. S. Kalika, "Transport and Structural Characteristics of Crosslinked Poly(Ethylene Oxide) Rubbers", Journal of Membrane Science, 276, 145–161 (2006).
25. V. A. Kusuma, B. D. Freeman, S. L. Smith, A. L. Heilman, and D. S. Kalika, "Influence of Tris-Based Co-Monomer on Structure and Gas Transport Properties of Cross-Linked Poly(Ethylene Oxide)", Journal of Membrane Science, 359, 25–36 (2010).
26. J. Liu, S. Zhang, D. Jiang, C. M. Doherty, A. J. Hill, C. Cheng, H. B. Park, and H. Lin, "Highly Polar but Amorphous Polymers with Robust Membrane CO_2/N_2 Separation Performance", Joule, 3, 1881–1894 (2019).
27. S. Luo, J. R. Wiegand, P. Gao, C. M. Doherty, A. J. Hill, and R. Guo, "Molecular Origins of Fast and Selective Gas Transport in Pentiptycene-Containing Polyimide Membranes and Their Physical Aging Behavior", Journal of Membrane Science, 518, 100–109 (2016).
28. C. R. Maroon, J. Townsend, K. R. Gmernicki, D. J. Harrigan, B. J. Sundell, J. A. Lawrence III, S. M. Mahurin, K. D. Vogiatzis, and B. K. Long, "Elimination of CO_2/N_2 Langmuir Sorption and Promotion of "N_2-Phobicity" within High-T_g Glassy Membranes", Macromolecules, 52, 1589–1600 (2019).
29. L. Zhu, M. Yavari, W. Jia, E. P. Furlani, and H. Lin, "Geometric Restriction of Gas Permeance in Ultrathin Film Composite Membranes Evaluated Using an Integrated Experimental and Modeling Approach", Industrial & Engineering Chemistry Research, 56, 351–358 (2016).
30. J. D. Goddard, J. S. Schultz, and S. R. Suchdeo, "Facilitated Transport via Carrier-Mediated Diffusion in Membranes: Part II. Mathematical Aspects and Analyses", AIChE Journal, 20, 625–645 (1974).

31. J. S. Schultz, J. D. Goddard, and S. R. Suchdeo, “Facilitated Transport via Carrier-Mediated Diffusion in Membranes: Part I. Mechanistic Aspects, Experimental Systems and Characteristic Regimes”, AIChE Journal, 20, 417–445 (1974).
32. Y. Han and W. S. W. Ho, “Design of CO_2-Selective Amine-Containing Membrane Process for Carbon Capture from Flue Gas”, Industrial & Engineering Chemistry Research, 59, 5340–5350 (2020).
33. K. K. Chen, W. Salim, Y. Han, D. Wu, and W. S. W. Ho, “Fabrication and Scale-up of Multi-Leaf Spiral-Wound Membrane Modules for CO_2 Capture from Flue Gas”, Journal of Membrane Science, 595, (2020).
34. Y. Han, W. Salim, K. K. Chen, D. Wu, and W. S. W. Ho, “Field Trial of Spiral-Wound Facilitated Transport Membrane Module for CO_2 Capture from Flue Gas”, Journal of Membrane Science, 575, 242–251 (2019).
35. M. Schultes, “Absorption of Sulphur Dioxide with Sodium Hydroxide Solution in Packed Columns”, Chemical Engineering & Technology, 21, 201–209 (1998).
36. Z. Wang, Y. Peng, X. Ren, S. Gui, and G. Zhang, “Absorption of Sulfur Dioxide with Sodium Hydroxide Solution in Spray Columns”, Industrial & Engineering Chemistry Research, 54, 8670–8677 (2015).
37. L. Albright, Albright's Chemical Engineering Handbook, CRC Press, Boca Raton, Florida (2008).
38. R. Davalos Monteiro, J. van de Wetering, B. Krawczyk, and D. L. Engelberg, “Corrosion Behaviour of Type 316L Stainless Steel in Hot Caustic Aqueous Environments”, Metals and Materials International, 26, 630–640 (2019).
39. R. Pang, Y. Yang, Y. Han, K. K. Chen, and W. S. W. Ho, “**Bicontinuous Substrates with Reduced Pore Restriction for CO2-Selective Composite Membranes**, J. Membr. Sci., 654, 120547 (2022).
40. X. Deng, C. Zou, Y. Han, L.-C. Lin, and W. S. W. Ho, “Computational Evaluation of Carriers in Facilitated Transport Membranes for Postcombustion Carbon Capture”, The Journal of Physical Chemistry C, 124, 25322–25330 (2020).
41. Y. Han and W. S. W. Ho, “Recent Advances in Polymeric Membranes for CO_2 Capture”, Chinese Journal of Chemical Engineering, 26, 2238–2254 (2018).
42. S. G. Pate, H. Xu, and C. P. O'Brien, “Operando Observation of CO_2 Transport Intermediates in Polyvinylamine Facilitated Transport Membranes, and the Role of Water in the Formation of Intermediates, Using Transmission Ftir Spectroscopy”, Journal of Materials Chemistry A, 10, 4418–4427 (2022).
43. G. Sartori, W. S. W. Ho, D. Savage, G. Chludzinski, and S. Wlechert, “Sterically-Hindered Amines for Acid-Gas Absorption”, Separation and Purification Methods, 16, 171–200 (1987).
44. C. Ye, J. Liu, F. Ren, and N. Okafo, “Design of Experiment and Data Analysis by JMP®(SAS Institute) in Analytical Method Validation”, Journal of Pharmaceutical and Biomedical Analysis, 23, 581–589 (2000).
45. W. Conway, D. Fernandes, R. Burns, G. Lawrance, G. Puxty, and M. Maeder, “Reactions of CO_2 with Aqueous Piperazine Solutions: Formation and Decomposition of Mono- and Dicarbamic Acids/Carbamates of Piperazine at 25.0 °C”, The Journal of Physical Chemistry A, 117, 806–813 (2013).
46. Y. Kim, J. Choi, S. Nam, S. Jeong, and Y. Yoon, “Nmr Study of Carbon Dioxide Absorption in Aqueous Potassium Carbonate and Homopiperazine Blend”, Energy & Fuels, 26, 1449–1458 (2012).

47. T. L. Donaldson and Y. N. Nguyen, “Carbon Dioxide Reaction Kinetics and Transport in Aqueous Amine Membranes”, Industrial & Engineering Chemistry Fundamentals, 19, 260–266 (1980).
48. J. J. Lee, C. J. Yoo, C. H. Chen, S. E. Hayes, C. Sievers, and C. W. Jones, “Silica-Supported Sterically Hindered Amines for CO_2 Capture”, Langmuir, 34, 12279–12292 (2018).
49. H. M. Stowe, E. Paek, and G. S. Hwang, “First-Principles Assessment of CO_2 Capture Mechanisms in Aqueous Piperazine Solution”, Physical Chemistry Chemical Physics, 18, 25296–25307 (2016).
50. Y. Shen, H. Chen, J. Wang, S. Zhang, C. Jiang, J. Ye, L. Wang, and J. Chen, “Two-Stage Interaction Performance of CO_2 Absorption into Biphasic Solvents: Mechanism Analysis, Quantum Calculation and Energy Consumption”, Applied Energy, 260, 114343 (2020).
51. S. Gangarapu, A. T. Marcelis, and H. Zuilhof, “Carbamate Stabilities of Sterically Hindered Amines from Quantum Chemical Methods: Relevance for CO_2 Capture”, ChemPhysChem, 14, 3936–3943 (2013).
52. B. Comesaña-Gándara, J. Chen, C. G. Bezzu, M. Carta, I. Rose, M.-C. Ferrari, E. Esposito, A. Fuoco, J. C. Jansen, and N. B. McKeown, “Redefining the Robeson Upper Bounds for CO_2/CH_4 and CO_2/N_2 Separations Using a Series of Ultrapermeable Benzotriptycene-Based Polymers of Intrinsic Microporosity”, Energy & Environmental Science, 12, 2733–2740 (2019).
53. P. Shirley and P. Myles, Quality Guidelines for Energy System Studies: CO_2 Impurity Design Parameters, US Department of Energy, National Energy Technology Laboratory (NETL), Report No. NETL-Pub-22529, OSTI Identifier No. 1566771, 2019.
54. R. James, A. Zoelle, D. Keairns, M. Turner, M. Woods, and N. Kuehn, Cost and Performance Baseline for Fossil Energy Plants Volume 1: Bituminous Coal and Natural Gas to Electricity, Revision 4, U.S. Department of Energy, Report Number: DOE/NETL-Pub-22638, Washington, DC, USA, 2019.

Suppliers

1. Sigma-Aldrich, 3050 Spruce Street, St. Louis, MO, 63103, USA; www.sigmaaldrich.com.
2. ThermoFisher Scientific. 25 Nimble Hill Rd., Newington, NH, USA. Contact: Greg Vinson, Ph: (800)258-0830, Office: (281)334-0164, Mobile: (281)851-0640.
3. Alfa Aesar, 26 Parkridge Road, Ward Hill, MA 01835, USA; Phone: 1-978-521-6300; Fax: 1-978-521-6350; www.alfa.com.
4. Millipore Corporation, 290 Concord Road, Billerica, MA 01821, USA; Phone: 1-800-MILLIPORE (1-800-645-5476) or 978-715-4321; www.emdmillipore.com.
5. Purolite Corporation, 150 Monument Road, Bala Cynwyd, PA 19004, USA; Phone: 1-610-668-9090; Fax: 1-610-668-8139; www.purolite.com.
6. Tokyo Chemical Industry Co., Ltd. (TCI), 9211 North Harborgate Street Portland, OR 97203, USA; Phone: 1-800-423-8616 or 1-503-283-1681; www.tcichemicals.com.
7. VWR International, Radnor Corporate Center Building One, Suite 200 100 Matsonford Road Radnor, PA19087-8660, USA; Phone:1-610-386-1700; www.vwr.com.
8. Varian Inc., 3120 Hansen Way, Palo Alto, CA 94304-1030, USA.
9. McMaster Carr, P.O. Box 94930, Cleveland, OH 44101-4930, USA; Phone: 330-995-5500; Fax: 330-995-9600.
10. Pall Corporation, 25 Harbor Park Drive, Port Washington, NY 11050, USA; Phone: (516) 484-5400.
11. Microdyn-Nadir US Inc. (formerly TriSep Corporation), 93 South La Patera Lane, Goleta, CA 93117, USA; Phone: 805-964-8003; Fax: 805-964-1235.
12. Arkema Inc., 900 First Avenue, King of Prussia, PA 19406, USA; Phone: 610-205-7252.
13. The Ohio State University Department of Chemistry Machine Shop, 0041 Evans Laboratory, 88 W 18th Avenue, Columbus, OH 43210, USA.
14. Branson Ultrasonics Corporation, 41 Eagle Rd., Danbury, CT 06813-1961, USA.
15. THINKY USA, Inc., 23151 Verdugo Drive, Suite 107, Laguna Hills, CA 92653, USA.
16. Inabata America Corporation, 611 Anton Blvd., Suite 925, Costa Mesa, CA 92626, USA.
17. R. T. Vanderbilt Company, Inc., 30 Winfield Street, Norwalk, CT 06856, USA.
18. Spectrum Laboratories, Inc., 18617 S Broadwick Street, Rancho Dominguez, CA 90220, USA.
19. Sekisui Specialty Chemicals America, LLC, 1603 West LBJ Freeway, Suite 200, Dallas, TX 75234, USA.
20. Pervatech Sales, Rondweg 48, 7468 MC Enter, The Netherlands.
21. Sumitomo Chemical Corp. http://www.sumitomo-chem.co.jp/english/.
22. Sekisui Specialty Chemicals America, LLC, 1603 West LBJ Freeway, Suite 200, Dallas, TX 75234, USA; Phone: (972) 277-2900; Fax: (972) 277-2907. (Distributed by: Brenntag Northeast Inc. Contact: Brian M. Bartashus, 81 W. Huller Lane, Reading PA 19605, USA; Phone: 610-926-4151 x3368).
23. Modular Process Technology Corporation, 2233 Paragon Drive, San Jose, CA 95131, USA; Phone: (408) 325-8640; Fax: (408) 3258649; Website: http://www.modularpro.com/.

Symbols, Abbreviations and Definitions

Abbreviations

2-ME	2-methoxyethanol
ACC	additional coal cost
ASLC	administration & support labor cost
ATD	anti-telescoping device
BEC	bare equipment cost
BL	blower
BP	Budget Period
BPC	cost of electricity of base plant
C1	Carrier 1
CC	capital cost
CCS	carbon capture and storage
CCT	carbon capture cost
CF	capacity factor
CFD	computational fluid dynamics
COE	cost of electricity
CSP	carrier saturation phenomenon
CWC	cooling water cost
DFT	density functional theory
DOE	Department of Energy
DOLC	direct operating labor cost
EC	engineering cost
ESP	electrostatic potential
EX	turbo expander
FC	fixed cost
FGD	flue gas desulfurization
FRP	fiber-reinforced plastic
FTM	facilitated transport membrane
GC	gas chromatography
Gly	glycinate ReaxFF
GPU	gas permeation unit; 1 GPU = 10^{-6} cm^3(STP) cm^{-2} s^{-1} $cmHg^{-1}$
GTI	gas technology institute
HOE	home office expense
HX	heat exchanger
ILC	installation labor cost
KO	water knock-out
LC	labor cost
MAE	mean absolution error
MB	membrane stage
MC	mobile carrier
MD	molecular dynamics
MFC	mass flow controller
MLC	maintenance labor cost
MMC	maintenance and material cost

MRC	membrane replacement cost
MSC	multi-stage compressor train
MSD	mean-square displacement
MW	molecular weight
NCCC	National Carbon Capture Center
NETL	National Energy Technology Laboratory
NMP	*N*-methyl-2-pyrrolidone
NMR	nuclear magnetic resonance
OAC	overhead & administration cost
OC	owner's cost
OSU	The Ohio State University in Columbus, Ohio
P&ID	piping and instrumentation diagram
pBuC1	poly(butylene C1)
PC	pressure controller
PES	polyethersulfone
pEtC1	poly(ethylene C1)
PFD	process flow diagram
PjC	project contingency
PMP	Project Management Plan
POC	payroll overhead cost
PrC	process contingency
PTI	property taxes and insurance
PVAm	polyvinylamine
PVAm-*ran*-PVC1	poly(vinylamine-*ran*-vinyl C1)
PVAm-*ran*-PVC1-*ran*-PNVF	poly(vinylamine-*ran*-vinyl C1-*ran*-*N*-vinylformamide)
PZEA-Sar	2-(1-piperazinyl)ethylamine sarcosinate
PZ-Gly	piperazine glycinate
Q	Quarter
ReaxFF	reactive force field
RO	reverse osmosis
RPPR	Research Performance Progress Report
SCS	sulfur caustic scrubbing
SEM	scanning electron microscopy
SP	SO_2 polishing cost
SW	spiral wound
T&S	transportation and storage
TC	temperature controller
TDC	total direct cost
TDLC	total direct labor cost
TEA	techno-economic analysis
TGly	tetrabutylphosphonium glycinate ReaxFF
TOC	total overnight cost
TPC	total plant cost
TS	transition state
VAC	vacuum pump train

VC	vacuum control
VIPS	vapor-induced phase separation
XPS	X-ray photoelectron spectroscopy
XRD	X-ray diffraction

Distribution List

Krista Hill
Project Officer
Carbon Capture Team
U.S. Department of Energy
National Energy Technology Laboratory
3610 Collins Ferry Road
PO Box 880
Morgantown, WV 26507-0880

W.S. Winston Ho
Yang Han
Li-Chiang Lin
Jingying Hu
Yi-Chen Huang
Babul Prasad
Shraavya Rao
Jianhang Shi
Yutong Yang
Zhien Zhang
Changlong Zou
The Ohio State University
William G. Lowrie Department of Chemical and Biomolecular Engineering
Department of Materials Science and Engineering
458 CBEC Building
151 West Woodruff Avenue
Columbus OH 43210-1350